UNIVERSITÀ DI PARMA

UNIVERSITA' DEGLI STUDI DI PARMA

DOTTORATO DI RICERCA IN
SCIENZA E TECNOLOGIA DEI MATERIALI

CICLO XXXVI

Functional polymers featuring molecular auxeticity and covalent dynamic bonds

Coordinatore:
Prof. Enrico Dalcanale

Tutore:
Prof. Alessandro Pedrini

Dottorando: Francesca Portone

2020/2021-2022/2023

Abstract

Functional polymers are a class of polymers that possess specialized chemical functionalities or structural features that enable them to perform specific functions or exhibit unique properties. These polymers are designed and synthesized to serve various applications across a wide range of industries. They can be tailored to have specific properties such as conductivity, biocompatibility, stimuli-responsiveness, adhesion, or biodegradability, among others. The versatility and tunability of functional polymers make them indispensable in numerous technological advancements and applications, driving ongoing research and development in polymer chemistry and materials science. This PhD thesis is focused on the study and development of auxetic materials and reprocessable thermosets for adhesive application.

After an overview on auxetic materials, an interesting class of materials with Negative Poisson's ratio values, reported in in Chapter 1, the attention is focused on the development of molecular auxetic system, using a quinoxaline cavitand (QxCav) as expandable unit.

In Chapter 2, the first synthetic molecular auxetic polymer is reported, obtained by incorporating a conformationally expandable cavitand as a crosslinker into a rigid polymer with intrinsic microporosity (PIM1). For this purpose, a QxCav bearing eight hydroxyl groups on the quinoxaline walls (C_v8H) is synthesized and reacted *via* multiple nucleophilic aromatic substitution reaction with the commercial tetrafluoroterephtalonitrile and 5,5',6,6'-tetrahydroxy-3,3,3',3'-tetramethyl-1,1'-spirobiindane to obtain the corresponding crosslinked polymer. The rigidity and microporosity of the polymeric matrix are pivotal to maximize the expansion effect of the cavitand by directly transfer the mechanical stress, resulting in sizable NPR values. This effect could be reached thanks to the direct covalent linking of the quinoxaline wings to the PIM structure. A theoretical micromechanical model is developed to predict the auxetic behavior, whereas experimentally, the NPR was verified *via* the digital image correlation (DIC) technique performed during the mechanical tests on films obtained by blending the auxetic crosslinked polymer with pristine PIM-1. Finally, the complete reversibility of the auxetic response is assessed upon five repeated loading cycles.

In chapter 3, QxCav is introduced as crosslinker in highly oriented main chain liquid crystal elastomeric (LCE) networks. For this purpose, the four quinoxaline walls are

decorated with terminal alkenes and the resulting cavitand is reacted via metathesis with a proper mesogenic unit in the presence of a Hoveyda-Grubbs 2nd generation catalyst. Monodomain LCE are achieved by mechanical alignment, and then characterized via differential scanning calorimetry (DSC) and polarized optical microscopy (POM). All materials retain the liquid crystalline properties, showing a range of mesophase of around 30°C. However, the inhomogeneity of the samples hampered the observation of auxetic behavior.

Moving to Chapter 4, a general introduction on covalent adaptable network is given, providing different examples of the main used dynamic exchange mechanism. These new materials bridge the gap between thermoplastics and thermosets.

In Chapter 5 a new dissociative exchange mechanism is reported. It is based on β-amino amide moieties mechanism synthetized using a two temperature dependence steps: a first Michael addition between methyl acrylate and an amine at 50°C and a subsequent amidation reaction at 100°C using a commercially available amine. Model study shows a dissociation from temperature beyond 160°C. The materials are reprocessed multiple times without compromising the properties. They exhibit also creep resistance and exceptional hydrolytic resistance in acid, basic and neutral environment.

Finally, in Chapter 6 a potential application as reversible adhesive using the chemistry discussed in Chapter 5 is tested. More in detail, a commercial liquid phenoxy-like resin is crosslinked with a dynamic hardener containing β-amino amide functionalities. Three different formulations are prepared and characterized using two different amines to tailor the T_g of such materials. All the materials give good lap shear strength results (up to 13 MPa) even after the first recycle (≈ 8 MPa). Subsequently, debonding is tested performing lap shear test at 180 °C, which resulted in complete detachment of the two aluminum joints. The broken specimens are then joined together, and the debonding is tested and confirmed after the first recycling showing zero force necessary for the detaching of the specimens.

Table of contents

Chapter 1

Introduction on auxetic materials

1.1. Overview of auxetic materials

Auxetics[1,2] are intriguing materials characterized by the counterintuitive property of lateral expansion upon longitudinal stretching. The term "auxetic" was coined for the first time by K. E. Evans, a pioneer in this field, and derives from the Greek word "auxetos" meaning "that may be increased".[3] Unlike conventional materials that exhibit positive Poisson's ratio, meaning they contract laterally when stretched longitudinally, auxetic materials expand laterally when subjected to longitudinal elongation (**Figure 1.1a**), corresponding to a Negative Poisson's Ratio (NPR).[4]

Poisson's ratio (PR) is important in defining mechanical properties of isotropic material, along with the remaining three elastic constants (Young's modulus E, bulk modulus K and shear modulus G) whose denote rigidity, compressibility, and stiffness of such material. It is defined as the ratio of transverse contraction strain (ε_{trasv}) to longitudinal extension strain (ε_{long}) considering the direction of the applied force (1).

$$\nu = -\frac{\varepsilon_{trasv}}{\varepsilon_{long}} \quad (1)$$

Theoretically, it is limited in the range -1 (for metamaterials) < ν < 0.5: the upper bound corresponds to the uncompressible material that conserve its volume when stretched (infinite K, rubber material) while the bottom is related to auxetic materials, (infinite G, anti-rubber material). More in detail, considering the expression (2) that define the shear modulus, for material with ν = -1 with a given value of E, the shear modulus will tend to infinite resulting in an extreme resistance to shear deformation.

$$G = \frac{E}{2(1+\nu)} \quad (2)$$

The enhancement of auxetics properties can be observed for values lower than -0.5 thus increasing drastically, for example, indentation resistance.[5]

In fact, when an object hits an auxetic it contracts laterally leading to a densification below the impact point (**Figure 1.1b**) corresponding to better dynamic impact energy absorption. Other interesting mechanical properties are also shear resistance[6], fracture toughness[7], sound and vibration absorption capabilities.[8]

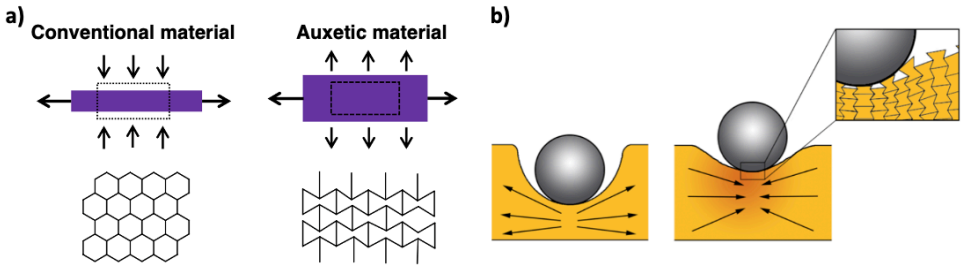

Figure 1.1. *a) Schematic representation of conventional and auxetic materials and their relative honeycomb network,[9] b) indentation response of classic and auxetic materials with the mechanism schematized in the inset.[2]*

Over the decades, a plethora of auxetic materials were discovered, studied, and synthetized at every dimensional scale, from macro- to mesoscopic or even microscopic and molecular level, natural or man-made. One examples of natural compound with NPR is α-cristobalite, a polymorph of crystalline silica. It displays auxeticity by a cooperative rotation of the rigid SiO_4 tetrahedral units.[10]

To attain negative PR values, two essential elements must be considered: the geometry and the deformation mechanism within the material's internal structure. At the macroscale level, the auxetic property is usually obtained through a particular architecture constituted by elements arranged in repeated patterns whose properties depend on their shape and arrangement rather than from the composition of the material itself (metamaterials).[11] A 2D honeycomb structure with hexagonal cells can be taken as example (**Figure 1.1a**, bottom left). In this case, the application of a force along x-axis correspond to elongation along the x direction and contraction on the y-axis resulting in positive PR. By keeping the same deformation mechanism and adjusting the cell geometry to feature the re-entrant "bow-tie" structure, the repetitive cells within the network now elongate and expands in vertical direction giving rise to auxeticity.[1][11-12] The first auxetic man-made example was reported by Lakes and co-workers in 1987.[14] They discovered NPR (-0.7) in polyurethane foam

(**Figure 1.2a**) by converting the convex polyhedral cell shape into the re-entrant one through thermal and mechanical treatment. Two years later Evans and co. showed the first examples of microporous polymer based on polytetrafluoroethylene (PTFE) with auxetic behavior (**Figure 1.2b**).[15] The mechanism lies in the microstructure of the polymer that consists of array of nodules interconnected by fibrils whose cooperative interaction under applied load generates auxeticity. In literature are extensively discussed several synthetic auxetic materials such as ceramics[16] or composites[17].

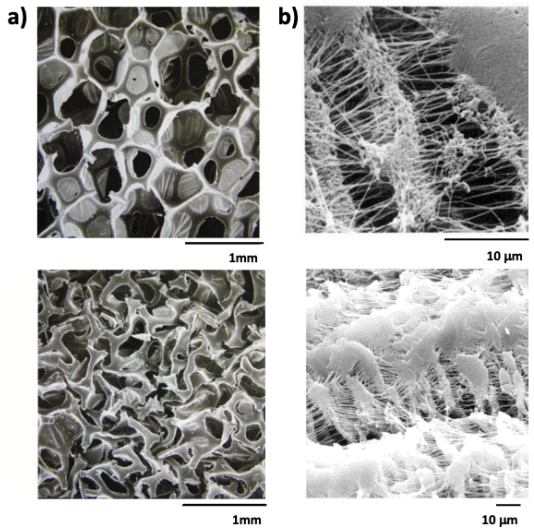

Figure 1.2. *a) SEM images of conventional foam (top) and the re-entrant auxetic foam (bottom),[14] b) SEM images at different magnifications of auxetic PTFE.[15]*

All these materials can be employed in a broad range of applications from biomedical to aerospace and automotive field. To report few examples, auxetic metamaterials can be used as smart bandage through the controlled release of medicine by exploiting the NPR of auxetic textiles. Auxetic-made artificial blood arteries can enhance their wall thickness in reaction to blood flow, preventing rupture from weakening. Aircraft nosecones could be made of composites auxetic panels taking advantage from the synclastic curvature to a dome-like shape when bent.[18] Auxetics have also been identified as candidate for bullet-proof vest for the densification properties after impact. Schumacher et al., inspired by the works of Disney Research

Lab, proposed auxetic materials in animation and graphic with the aim to obtain characters with controllable and desired deformation making them more realistic.[19]

1.2. Molecular auxetics

The major unresolved issue in auxetics is represented by the synthesis of 3D continuum (in a wide range of length scales) auxetic materials. Most current synthetic auxetic materials, whose auxeticity is triggered by deformation of their meso- or macroscopic structure, are discontinuous at the nanoscale and expand only when stretched in a particular direction. This limitation can be overcome only by operating at the molecular level. Molecular auxetics, in fact, prevail some limits of artificial auxetic in terms of desired mechanical responses to multidirectional external loads.

Over the decade, inspired by macroscopic re-entrant honeycomb and rotating triangle structures,[20] molecular auxetic behavior has been theoretically predicted for a variety of molecular networks constituted by "twisted-chain" polyacetylenes,[21] crosslinked rigid polyphenylacetylenes[20] (**Figure 1.3b**), calix[4]arene-based 3D polymeric network[22] (**Figure 1.3a**) and prismane-based molecular rods[23] (**Figure 1.3c**).

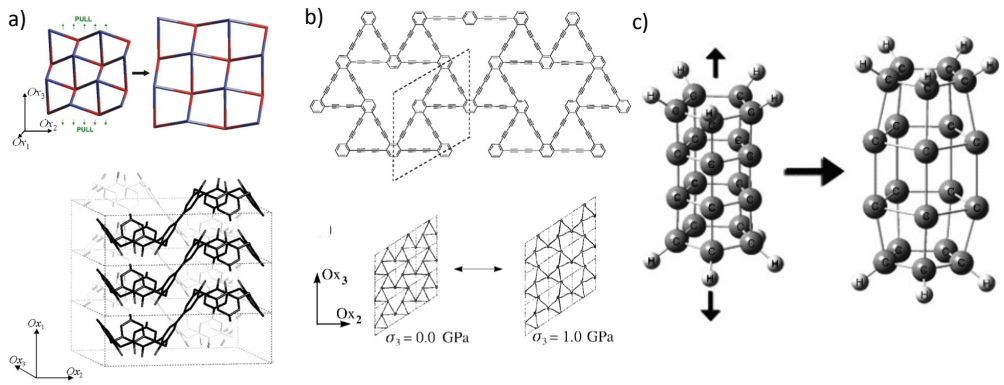

Figure 1.3. *Examples of potential molecular auxetics: a) Evans' polyphenylacetylene[20]; c) Grima's calix[4]arene network;[22] d) Hoz's polyprismane rods.[23]*

However, the synthesis of such precisely arranged, highly crosslinked structures revealed to be unfeasible so far. As alternative, in 1998, Griffin prepared main-chain

liquid crystalline elastomers with bulky rigid laterally attached rods, susceptible to force-induced rotation upon stretching (**Figure 1.3** left).[24]

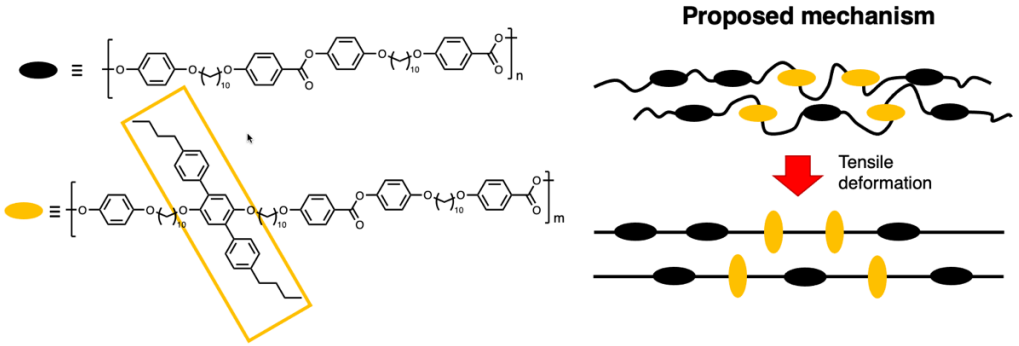

Figure 1.4. *Scheme of the auxetic liquid crystals polymers (left) and the proposed mechanism (right): in yellow the laterally attached mesogens resulted in increasing interchain distance after deformation.*

The interchain distance of the polymeric chains in the oriented nematic phase should increase in a direction perpendicular to the applied force (**Figure 1.4** right). Even if a small increase of the interchain distance has been observed by X-Ray scattering,[25] the reported system failed to evidence an auxetic behavior. More recently, auxetic 2D protein crystals, designed to self-assembled via different molecular interactions (disulfide linkage or metal coordination) into a 2D molecular lattices have been proposed (**Figure 1.5**).[26] The system displays seven motion of the lattice moving from an opened to a closed conformation. Theoretically prediction of Poisson's ratio was estimated at -1 value and was assessed through a Digital Imaging Correlation (DIC) analysis on reconstructed TEM images of protein crystals. However, mechanical tests on RhuA crystals are unfeasible without the incorporation in a polymeric matrix.

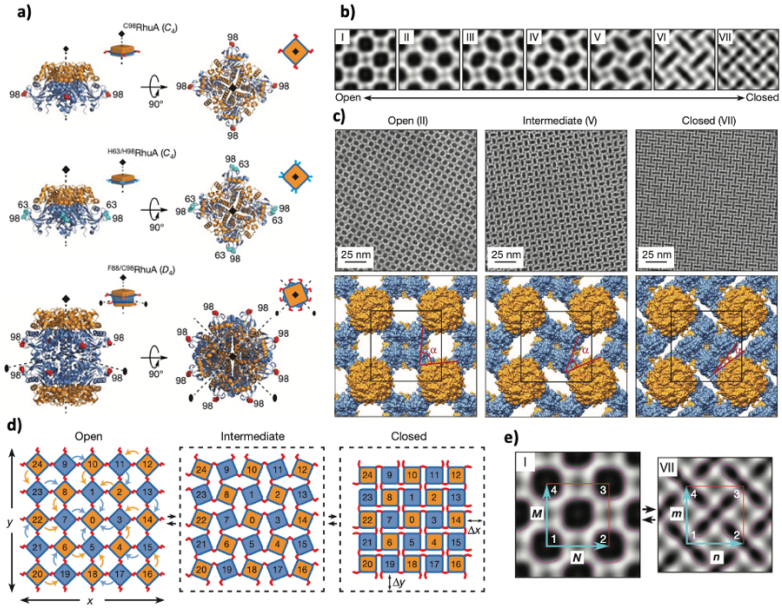

Figure 1.5. *a) Schematic representation of RhuA structures, b) Seven distinct conformational state reconstructed from 2D images of Rhua crystal, c) High-magnification views and derived structural models of conformations II, V and VII, d) Schematic representation of rotating, rigid square model that describes 2D Rhua dynamics, e) DIC analyses of reconstructed TEM images considering states I and VII.*[26]

In 2018 the first synthetic molecular auxetic, with experimental υ = -0.74 ± 0.03, was described by Gleeson and coworkers[27]: it is a nematic liquid crystal elastomer (LCE) whose auxeticity is triggered by a negative ordering of the LCE backbone. The auxetic behavior occurs only in one axis and beyond a threshold strain (**Figure 1.6b**) while for small deformation no auxetics response is observed. In the Authors' own words, this makes the LCE a *partial auxetic*[28]: their anisotropic nature allow NPR in one axis preserving on the other transverse axis positive PR thus retaining the volume. LCE auxetic deformation can be described in a more complete way via a "mechanical-Fréedericksz" transition (MFT) rather than semisoft elastic (SSE) response. The MFT is distinguished by a discontinuous director rotation that occurs at a specific critical strain, while in SSE response the liquid crystals director continuously rotates to align with the applied strain. This study concluded with the necessity of biaxial order (**Figure 1.6a**) of the material that allows the desired auxetic behavior.[28]

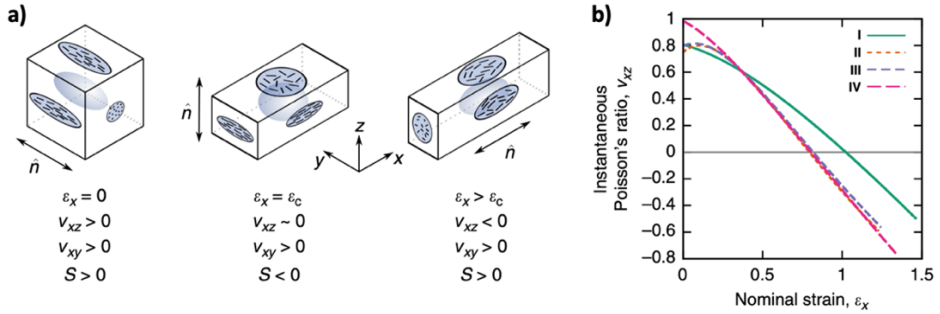

Figure 1.6. *a) Relationship between LC order and the strain-dependent PR (S = liquid crystal order parameter, ε_c = critical strain), b) Measured strains and instantaneous PR behavior.*[27]

The absence of workable solutions to the synthesis of 3D intrinsic molecular auxetics calls for a different approach to the problem. In this thesis is reported an unprecedented solution based on a conformationally expandable component called quinoxaline cavitand.

1.3. Quinoxaline cavitands

Cavitands, resorcinarene-based macrocycles, were originally designed as molecular receptors.[29] More recently, cavitands molecular recognition properties have been exploited as key components in supramolecular polymers[30] and molecular grippers.[31] Several possible functionalizations of these molecules at the upper rim are available. In this thesis, the attention is focused on quinoxaline cavitands (QxCav), obtained by the fourfold bridging of a proper functionalized 2,3-dichloroquinoxaline on a resorcinarene scaffold. The resulting hydrophobic cavity makes them suitable for aromatic guest complexation, such as BTEX in air.[32] Furthermore, QxCav have the peculiar ability to switch between two well-defined conformations: a compact one, called *vase* (C_{4v} symmetry) and an extended one named *kite* (C_{2v} symmetry) (**Figure 1.7** top).[33] The *vase-kite* interconversion has been extensively investigated in solution *via* different stimuli such as pH,[34] temperature,[33] metal coordination[31,35] and redox.

DFT calculations estimate the energy barrier for the interconversion of a quinoxaline wall in 7.6 kcal mol^{-1} and predict that the *vase* form is by 3.2 kcal mol^{-1} more stable than the *kite* form (**Figure 1.7** bottom).[36] All intermediate conformations are energetically disfavored, therefore only these two discrete conformers are observed.

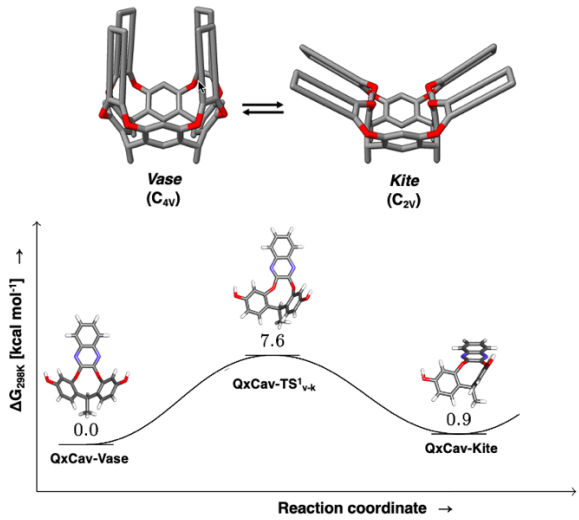

Figure 1.7. *Representation of vase-kite switching (top) and DFT calculation on the switching of a single quinoxaline cavitand wing (bottom).[36]*

More recently, our research group demonstrated that mechanical stimulation (tensile stress) is effective in inducing the expansion/contraction of these dimensionally variable units in cavitand-crosslinked matrices (**Figure 1.8** left). Preliminary studies were carried out on two different polymer matrices: an elastomeric polydimethylsiloxane (PDMS) and a more rigid polyurethane (PU), both crosslinked with a proper functionalized quinoxaline cavitands. In PDMS, known for the activation of mechanophores,[36-37] no evidences of *vase-kite* interconversion was observed upon tensile stimulation of polymer specimens. This was ascribed to the elastomeric nature of the matrix that dissipates the mechanical energy preventing the opening of the cavitand. Moving to the rigid polyurethane, spectroscopic analyses evidenced the appearance of a diagnostic band of the *kite* conformer in UV-Vis and fluorescence spectra proving the mechanically triggered *vase-to-kite* switching only of a fraction of cavitands (30 to 50%, **Figure 1.8** right).[39]

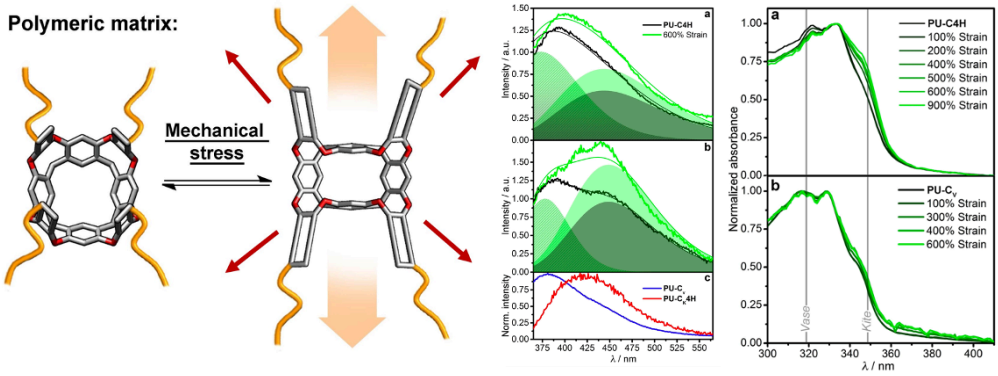

Figure 1.8. *Switching vase-kite in a generic polymeric matrix (left), experimental emission and UV-Vis spectra of cavitand crosslinked polyurethane upon tensile elongation (right).*[39]

The *vase-to-kite* switching is characterized by a large dimensional expansion of the molecule, driven by the lateral opening of its four wings. More in detail, by roughly approximation of the tetraquinoxaline cavitand with a parallelepiped, the volume of the two conformers result 2.85 nm^3 and 2.06 nm^3 for *kite* and *vase* conformation respectively, thus the volume increased by 1.4 times with respect to the closed form.[40] The lack of workable molecular auxetics make quinoxaline cavitands ideal and suitable platforms for the development of these materials.[41]

In the following two chapters two different matrices will be tested with the aim to develop molecular auxetic materials using a quinoxaline cavitand as crosslinker: liquid crystal elastomers (LCEs) and polymers of intrinsic microporosity (PIMs). The choice of LCEs lies in the highly order and collective behavior of liquid crystals (LC) in contrast to the random coil conformation of PDMS or polyurethane. Given the inherent orientation of LC polymer chains, the mechanical stress applied is more efficiently transferred to the cavitand molecules, leading a transition to the open conformation, and consequently an expansion in volume.

PIMs, instead, were selected for the high rigidity and microporosity of the polymeric matrix, which are pivotal to maximize the expansion effect of the cavitand opening by mechanical stress on the polymer network.

References

[1] K. E. Evans, M. A. Nkansah, I. J. Hutchinson, S. C. Rogers, *Nature* **1991**, *353*, 124.

[2] K. E. Evans, A. Alderson, *Adv. Mater.* **2000**, *12*, 617.

[3] K. E. Evans, *Endeavour* **1991**, *15*, 170.

[4] G. N. Greaves, A. L. Greer, R. S. Lakes, T. Rouxel, *Nature Mater* **2011**, *10*, 823.

[5] R. S. Lakes, K. Elms, *Journal of Composite Materials* **1993**, *27*, 1193.

[6] J. B. Choi, R. S. Lakes, *J Mater Sci* **1992**, *27*, 4678.

[7] J. B. Choi, R. S. Lakes, *Int J Fract* **1996**, *80*, 73.

[8] C. P. Chen, R. S. Lakes, *Journal of Engineering Materials and Technology* **1996**, *118*, 285.

[9] M. Alizadeh, I. K. Tennie, U. Steiner, A. F. M. Kilbinger, *Chimia* **2019**, *73*, 25.

[10] N. R. Keskar, J. R. Chelikowsky, *Nature* **1992**, *358*, 222.

[11] R. Gatt, L. Mizzi, J. I. Azzopardi, K. M. Azzopardi, D. Attard, A. Casha, J. Briffa, J. N. Grima, *Sci Rep* **2015**, *5*, 8395.

[12] G. W. Milton, *Journal of the Mechanics and Physics of Solids* **1992**, *40*, 1105.

[13] D. Y. Fozdar, P. Soman, J. W. Lee, L.-H. Han, S. Chen, *Adv. Funct. Mater.* **2011**, *21*, 2712.

[14] R. Lakes, *Science* **1987**, *235*, 1038.

[15] B. D. Caddock, K. E. Evans, *J. Phys. D: Appl. Phys.* **1989**, *22*, 1877.

[16] J. Dominec, P. Vašek, P. Svoboda, V. Plecháček, C. Laermans, *Mod. Phys. Lett. B* **1992**, *06*, 1049.

[17] P. J. Hine, R. A. Duckett, I. M. Ward, **n.d.**

[18] K. E. Evans, *Composite Structures* **1991**, *17*, 95.

[19] C. Schumacher, B. Bickel, J. Rys, S. Marschner, C. Daraio, M. Gross, *ACM Trans. Graph.* **2015**, *34*, 1.

[20] J. N. Grima, K. E. Evans, *Chem. Commun.* **2000**, 1531.

[21] R. H. Baughman, D. S. Galvão, *Nature* **1993**, *365*, 735.

[22] J. N. Grima, J. J. Williams, K. E. Evans, *Chem. Commun.* **2005**, 4065.

[23] N. Pour, L. Itzhaki, B. Hoz, E. Altus, H. Basch, S. Hoz, *Angew. Chem. Int. Ed.* **2006**, *45*, 5981.

[24] C. He, P. Liu, A. C. Griffin, *Macromolecules* **1998**, *31*, 3145.

[25] C. He, P. Liu, P. J. McMullan, A. C. Griffin, *phys. stat. sol. (b)* **2005**, *242*, 576.

[26] Y. Suzuki, G. Cardone, D. Restrepo, P. D. Zavattieri, T. S. Baker, F. A. Tezcan, *Nature* **2016**, *533*, 369.

[27] D. Mistry, S. D. Connell, S. L. Mickthwaite, P. B. Morgan, J. H. Clamp, H. F. Gleeson, *Nat Commun* **2018**, *9*, 5095.

[28] T. Raistrick, Z. Zhang, D. Mistry, J. Mattsson, H. F. Gleeson, *Phys. Rev. Research* **2021**, *3*, 023191.

[29] In *Monographs in Supramolecular Chemistry*, Royal Society Of Chemistry, Cambridge, **2007**, pp. P009-P014.

[30] M. Dionisio, L. Ricci, G. Pecchini, D. Masseroni, G. Ruggeri, L. Cristofolini, E. Rampazzo, E. Dalcanale, *Macromolecules* **2014**, *47*, 632.
[31] I. Pochorovski, F. Diederich, *Acc. Chem. Res.* **2014**, *47*, 2096.
[32] A. Rozzi, A. Pedrini, R. Pinalli, E. Cozzani, I. Elmi, S. Zampolli, E. Dalcanale, *Nanomaterials* **2022**, *12*, 2204.
[33] J. R. Moran, J. L. Ericson, E. Dalcanale, J. A. Bryant, C. B. Knobler, D. J. Cram, *J. Am. Chem. Soc.* **1991**, *113*, 5707.
[34] **N.d.**
[35] M. Frei, F. Marotti, F. Diederich, *Chem. Commun.* **2004**, 1362.
[36] *I. Pochorovski, Redox-Switchable Cavitands: Conformational Analysis and Binding Studies, Ph.D. Thesis, ETH- Dissertation Nr. 21351, ETH Zürich, 2013.*, **n.d.**
[37] C. L. Brown, M. H. Barbee, J. H. Ko, H. D. Maynard, S. L. Craig, *J. Chem. Educ.* **2017**, *94*, 1752.
[38] G. R. Gossweiler, C. L. Brown, G. B. Hewage, E. Sapiro-Gheiler, W. J. Trautman, G. W. Welshofer, S. L. Craig, *ACS Appl. Mater. Interfaces* **2015**, *7*, 22431.
[39] M. Torelli, F. Terenziani, A. Pedrini, F. Guagnini, I. Domenichelli, C. Massera, E. Dalcanale, *ChemistryOpen* **2020**, *9*, 261.
[40] R. Brighenti, F. Artoni, F. Vernerey, M. Torelli, A. Pedrini, I. Domenichelli, E. Dalcanale, *Journal of the Mechanics and Physics of Solids* **2018**, *113*, 65.
[41] M. Torelli, Molecular Strategies for Functional Materials: Soft Mechanochemistry and Surface Functionalization, PhD thesis, Università degli studi di Parma, **2017**.

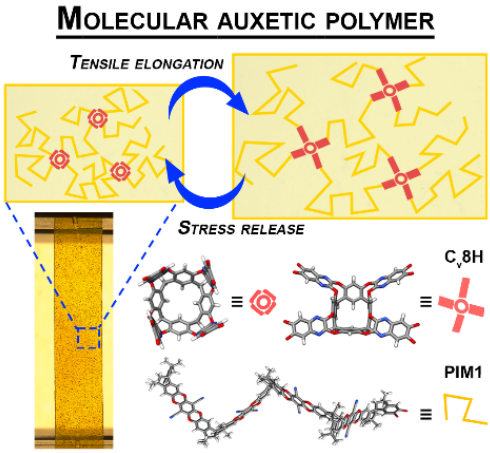

Abstract: Auxetics are materials characterized by a negative Poisson's ratio (NPR), an uncommon mechanical behavior corresponding to a transversal deformation tendency opposite to the traditional materials. Here we present the first example of a synthetic molecular auxetic polymer obtained by embedding a conformationally expandable cavitand as crosslinker into a rigid polymer of intrinsic microporosity (PIM). The rigidity and microporosity of the polymeric matrix are pivotal to maximize the expansion effect of the cavitand that, under mechanical stress, can assume two different conformations: a compact *vase* one and an extended *kite* form. The auxetic behavior and the corresponding NPR of the proposed material is predicted by a specific micromechanical model that considers the cavitand volume expansion ratio, the fraction of the cavitand crosslinker in the polymer, and the mechanical characteristics of the polymer backbone. The reversible auxetic behavior of the material is experimentally verified via Digital Image Correlation technique (DIC) performed during the mechanical tests on films obtained by blending the auxetic crosslinked polymer with pristine PIM. Two specific control experiments prove that the mechanically driven conformational expansion of the cavitand crosslinker is the sole responsible of the observed NPR of the polymer.

Adapted from: F. Portone, M. Amorini, M. Montanari, R. Pinalli, A. Pedrini, R. Verucchi, R. Brighenti, E. Dalcanale, *Adv. Funct. Mater.* **2023**, 2307605.

Chapter 2

Molecular Auxetic Polymer of Intrinsic Microporosity via Conformational Switching of a Cavitand Crosslinker

2.1 Introduction

2.1.1 Polymers of Intrinsic Microporosity (PIMs)

Polymers of intrinsic microporosity (PIMs) are a particular class of linear or networked microporous polymer containing a continuous network of interconnected intermolecular voids less than 2 nm in width,[1] making them promising membrane materials for several application such as pervaporation,[2,3] gas separation[4] and ion selective membranes[5,6].

PIMs concept derived from a study of phthalocyanine materials, known to be catalytically active, especially in oxidation reaction.[7] However, SBI (spirobisindane) units, in particular 5,5',6,6'-tetrahydroxy-3,3,3',3'-tetra-methyl-1,1-spirobisindane (TTSBI), were incorporated in phthalocyanine and porphyrin-based polymer to avoid co-facial aggregation of the large planar aromatic macrocycles yielding to a catalytically active porous network materials with apparent BET surface areas up to 1000 m^2g^{-1}.[8] Afterwards, the preparation of polymers with high surface area, named PIM, were designed with a general SN_{Ar} reaction based on appropriate halogenated monomers and multiple catechol derivatives, such as TTSBI. PIMs consist of two parts: a structural unit that introduces a site of contortion (e.g. spirocenter, non-planar rigid backbone or single covalent bond in which rotation is prevented) and a linking group (e.g. derived from dibenzodioxin or imide formation) that join the structural units during polymerization but prohibits rotation of one unit relative to

its neighbors. The resulting polymer chains consist of fused aromatic rings, with a rigid but kinked structure, that prevent efficient space packing of polymer chains, thereby creating large free volume and introducing microporosity. This feature kicks off several studies and investigations on non-networked porous polymers for their advantage of solubility, ease of characterization, and facile membranes fabrication.

Thereafter, numerous non-networked PIMs based on dibenzodioxin formation (**Table 2.1**) and imide linkages (PIM-PIs, **Table 2.2**)[9,10] were investigated. This latter was investigated for the commercial application of polyimides and the efficient formation of the linkage. However, in PIM-PIs the presence of imide bonds that allows rotation around them leads to a decrease in microporosity. For this reason, steric hindered group adjacent to the diamines are introduced to restrict the C-N rotation.

Table 2.1. *General scheme of most common PIM based on benzodioxin formation: monomers used, solubility and name of each polymer are reported.*

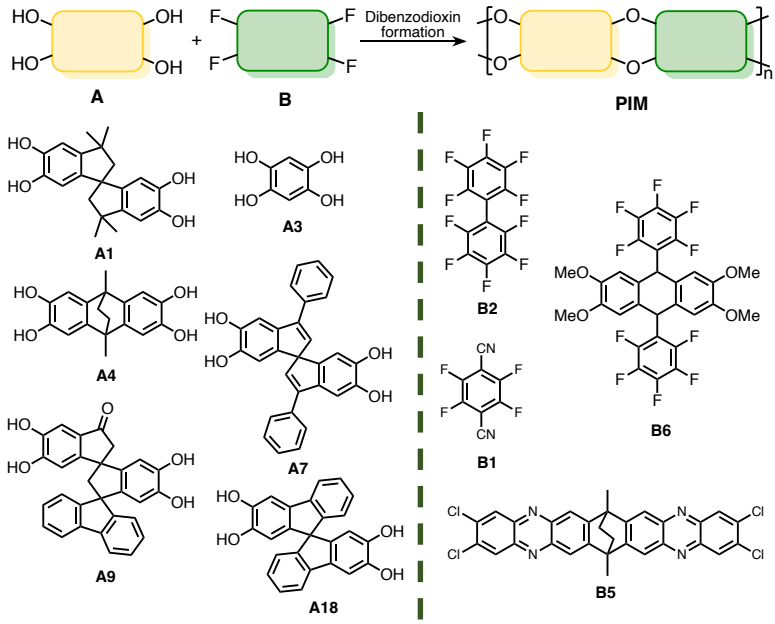

Monomers	Solubility	Name
A1+B1	$CHCl_3$, THF	PIM-1[1]
A3+B2	THF	PIM-6[1]
A7+B1	Quinoline	Polymer from 6[11]
A4+B5	m-cresolo	PIM-10[12]
A1+B6	$CHCl_3$	MP1[13]
A9+B1	DMF, quinoline	Polymer from 10[11]
A18+B1	$CHCl_3$	PIM-CH_3-HPB[14]

PIM-Pis are polyimides prepared from a cycloimidization reaction between a diamine and dianhydride.

Table 2.2. *General scheme of PIM-PI based on imide formation, monomers used, solubility and name of each polymer.*

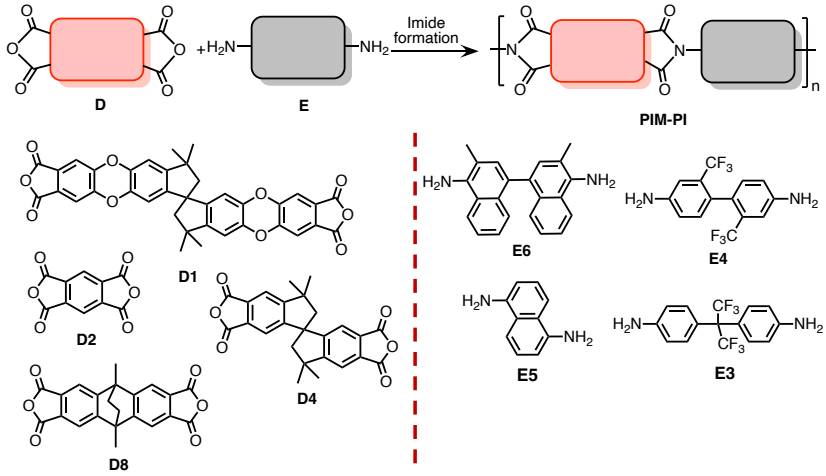

Monomers	Solubility	Name
D1+E3	$CHCl_3$	PIM-PI-3[15]
D1+E4	$CHCl_3$	PIM-PI-4[15]
D1+E5	$CHCl_3$	PIM-PI-7[15]
D1+E6	$CHCl_3$	PIM-PI-8[15]
D4+E6	$CHCl_3$	PIM-PI-10[16]
D8+E6	THF	PIM-PI-12[17]

The development of polymers with relatively more rigid components gave rise to a new class of PIMs (PIM-TB) prepared starting from diamine as the only monomer. The polymerization reaction, in this case, is based on an electrophilic aromatic substitution between a diamine and formaldehyde to generate a bridged bicyclic structure named Tröger's Base,[18] that provides both rigidity and site of contortion in the final polymer (**Table 2.3**).

Table 2.3. General scheme of PIM-TB, diamine used, solubility and name of each polymer.

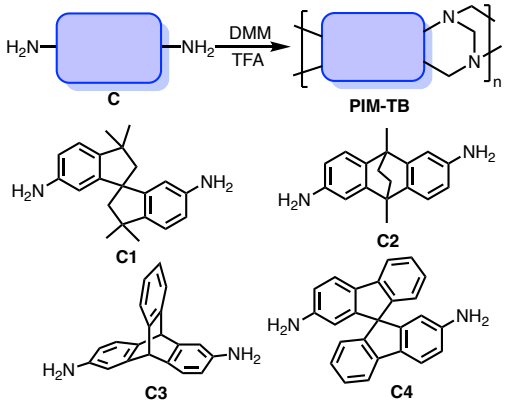

Monomers	Solubility	Nome
C1	$CHCl_3$	PIM-SBI-TB[19]
C2	$CHCl_3$	PIM-EA-TB[19]
C3	$CHCl_3$	PIM-Trip-TB[19]
C4	$CHCl_3$	PIM-SBF-TB[19]

2.1.2 PIM-1 synthesis and application

The first example of PIM studied was PIM-1, synthetized through a double nucleophilic aromatic substitution of TTSBI and 2,4,5,6-tetrafluoroterephthalonitrile (TFTPN, **Scheme 2.1**).[20]

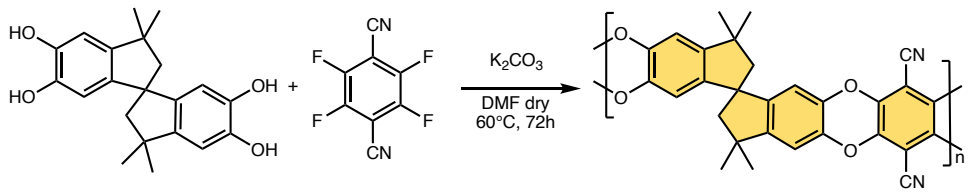

Scheme 2.1. *PIM-1 reaction scheme synthetized via LTM method.*

The spirocenter related to TTSBI exhibits a non-linear V-shaped geometry, affording a contortion site. After the formation of dioxine linkage, a ladder structure is then achieved lead to a limited rotational freedom as represented in **Figure 2.1**.

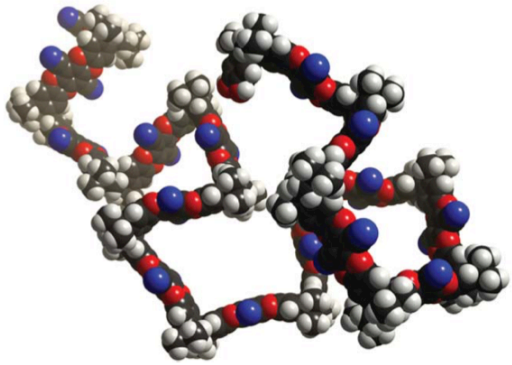

Figure 2.1. *3D fragment of PIM-1.*

In literature are present two methods for the synthesis of PIM-1. The first one is known as low temperature methos (LTM)[1] and is carried out using equimolar amount of monomers, K_2CO_3 as base in dry DMF at 60°C for 3 days. The second method, referred as high-temperature method (HTM)[21], differs from the first one in terms of time (40 minutes), temperature (150°C) and solvent (dimethyl acetamide). Another difference is the dilution of the two system, indeed in HTM toluene is added to the mixture to facilitate the stirring after the increasing of viscosity. Both methods provide polymer with high average molecular weight and film-forming capability. However, LTM should be favored for its ease of processability and scalability.[16]

Gas separation membrane, such as CH_4/CO_2, is the most well-known application of PIM-1 (BET surface area = 750 m^2 g^{-1}). However, there are various interesting application including laser sensor, due to his strong fluorescence behavior, sensitive in the detection of nitroaromatics [22], colorimetric sensor for organic vapor detection,[23] using the phenomenon of rapid change in the reflective index of a thin PIM-1 film, combined with its rapid change in color from green to red. It can be used as preconcentrator for the detection of chlorinated organic compounds and benzene in soil matrix.[24]

In this thesis, PIM-1 was employed as polymer matrix crosslinked with tetraquinoxaline cavitands for the developing of molecular auxetics. Recently Dichtel and co-workers developed cavitand-based porous organic polymers (POPs), which possess -OH functionalities that provides multiple sites for the polymerization with

TFTPN and tetrafluoroisonicotinonitrile (TFIN). The polymer with TFIN showed high surfaces area (1190 m^2 g^{-1}) capable to remove $CHCl_3$ or 1,4-dioxane in water.[25]
A tetraquinoxaline cavitand bearing eight hydroxyl groups at the upper rim was designed and polymerized with PIM-1 monomers. The intrinsic rigidity of the polymeric matrix is the key ingredient to translate the mechanically driven conformational switch of cavitands into an auxetic behavior, by avoiding that the molecular expansion could be adsorbed by local re-arrangements of the polymer backbone.

2.2 Results and discussion

2.2.1 Theoretical prediction of the auxetic behavior

The cavitand expandable unit embedded in the **PIM1** polymer network was defined as *auxeton*. **Figure 2.2a** shows the proposed auxeton in the *vase* and *kite* conformers, considering as expandable wings the four planar panels resulting from the reaction of the crosslinking unit **Cv8H** (**Figure 2.2a**) with **PIM1** monomers up to the first spirobiindane contortion site (red and green fragments in **Figure 2.2b**). The two structures have been optimized *via* molecular mechanics calculations using the geometrical parameters obtained by the crystal structures of the two related cavitands as base.[26,27] The linear conformational expansion in one direction is sizable, moving from 14 to almost 37 Å in elongation (**Figure 2.2a**). The corresponding volumes of the two conformers are shown in **Figure 2.2b**, leading to a cavitand expansion factor $J_{V\text{-}K} = V_{Kite}/V_{Vase}$ = 2.62. The length of the wings determines the cavitand expansion factor. The most relevant parameters influencing the final NPR are the cavitand expansion ratio, the cavitand volume fraction, combined with the intrinsic rigidity of the PIM matrix. The average mechanical properties of the proposed auxetic polymer are estimated by knowing the cavitand volume expansion ratio $J_{V\text{-}K}$, the fraction Φ of the cavitand crosslinker in the polymer, and the mechanical characteristics of the polymer backbone. The micromechanical model of the auxetic polymer is detailed below.

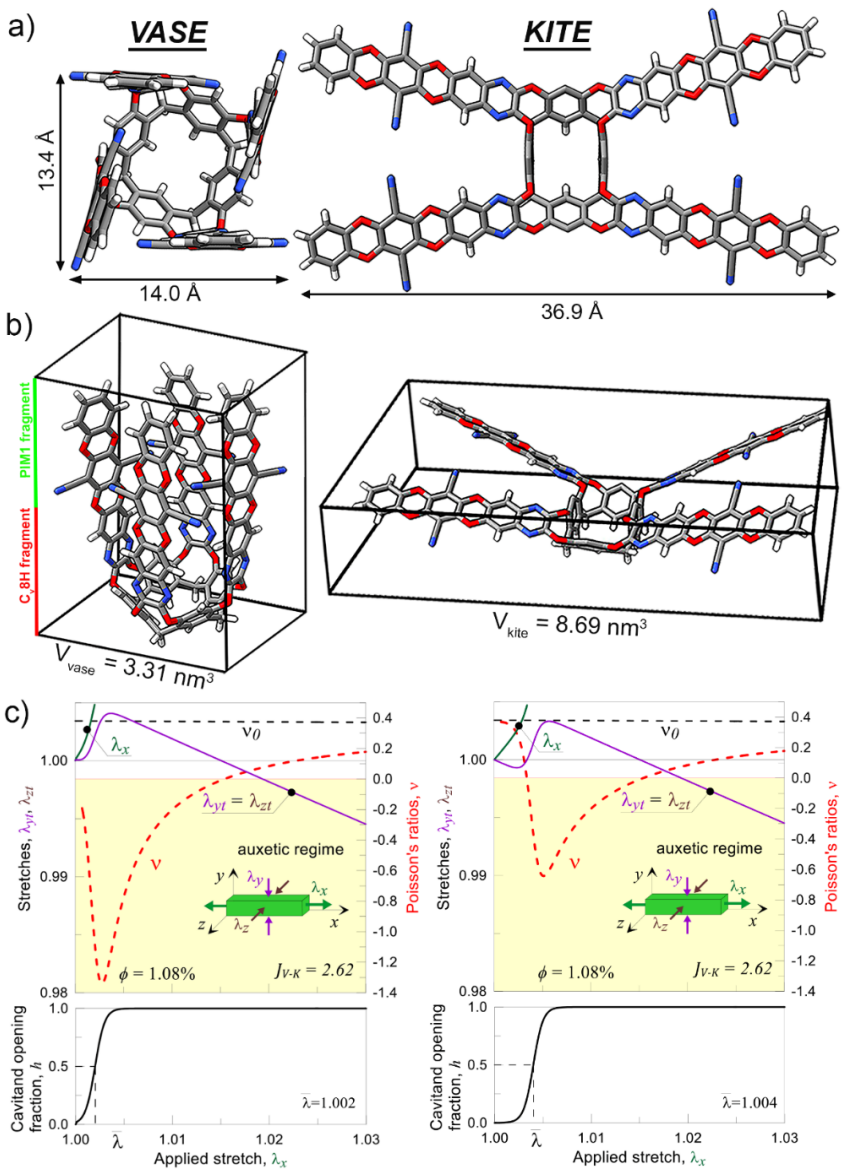

Figure 2.2. *Theoretical prediction of the auxetic behavior: a) Spartan optimized structures of the auxeton in the vase and kite form with the respective dimensions; b) volume of the auxeton in the vase and kite forms; c) Poisson's ratio for a PIM with cavitand molecules (Φ = 1.08% vol) vs applied stretch λ_x. Transversal stretches $\lambda_y = \lambda_z$ are also represented. Different values of the parameter $\bar{\lambda}$ of the cavitand opening function h have been used to underline the effect of such a parameter characterizing the theoretical model on the calculated Poisson's ratio.*

The mechanical properties of the PIM with crosslinked cavitand molecules are assessed by assuming that the smallest material volume element, referred to as the Representative Volume Element (R.V.E.)[28] (**Figure 2.3a**), correctly represents the average mechanical properties of the overall material having the same composition and microstructure of the R.V.E.

According to the Freely Jointed Chain (FJC) model, each polymer chain is modeled as a sequence of N rigid segments with length b,[29]whose 3D arrangement is typically assumed to obey to the random walk theory[30]: the vector lying between the initial and final point of the chain is denoted by $\boldsymbol{r}$ (end-to-end vector). According to the rubber elasticity theory, the mechanical state of the material depends only on the distribution of the chains end-to-end vectors. Such a distribution is usually assumed to be Gaussian (**Figure 2.3b**).[4] By stretching the material, the initial distribution f_0 (corresponding to the stress-free state) changes due to the elongation of the chains lying along the loading direction and the contraction of the chains perpendicular to it (**Figure 2.3c**).

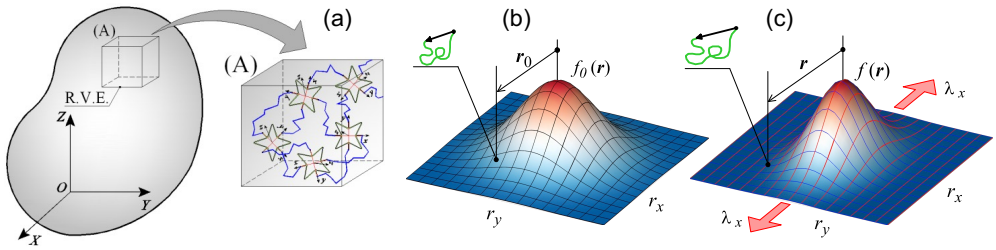

Figure 2.3. *Schematic of the Representative Volume Element (R.V.E.) of a polymeric material containing auxeton elements (a). Schematic of the polymer's chains end-to-end distance distribution $f_0(\boldsymbol{r})$, $\boldsymbol{r} = (r_x, r_y)$ in a 2D chain network arrangement in the undeformed (b) and in a generic deformed (c) configuration.*

The mechanical energy density of the material is evaluated as the difference between the energy density in the current (deformed) and in the initial (undeformed) state:

$$\Delta\Psi(t) = c_a\langle(f - f_0)\psi\rangle - p[J - (1 + \phi\, h\, J_{v\to k})] \qquad (1)$$

In Eq. (1) $\langle\ldots\rangle$ indicates the integration over the chain configuration space, ψ is the mechanical energy per single chain, p is the hydrostatic pressure and $(1 + \phi\, h\, J_{V-K})$ is the volume change ratio due to the opening of the fraction $(\phi\, h)$ of cavitands, while

c_a is the cross-link density. $J_{V-K} = V_k/V_v > 1$ (the subscripts K and V refer to the *kite* and *vase* configuration, respectively) indicates the volume ratio related to the *vase-kite* conformation change, $0 \leq h \leq 1$ is the fraction of the open ones, ϕ is the total volume fraction of cavitands present in the unit volume of polymer.

Such an energy depends only on the current (deformed state, described by $f(\mathbf{r})$) and on the initial (undeformed state, described by $f_0(\mathbf{r})$) polymer's chains configurations, and provides the mechanical state of the material.[31] The dynamic nature of the equilibrium state of the cavitand opening mechanism obeys a balance reaction law, analytically described by the standard kinetic Eq. (2)[32]:

$$\frac{d\phi_k}{dt} = k_A\, \phi_v - k_D\, \phi_k \qquad (2)$$

where $\phi = \phi_K + \phi_V$ is the total volume fraction of the cavitands, $\phi_K = h\,\phi$ and $\phi_V = (1-h)\phi$ are the volume fractions of the open (*kite* conformation) and close (*vase* conformation) molecules, while k_A, k_D are the activation and deactivation reaction rates, respectively.

Since the volume fraction of open molecules depends on the mechanical deformation of the network, we can write $\phi_K = h(\boldsymbol{F})\,\phi$, $\boldsymbol{F}$ being the deformation gradient tensor; Eq. (2) can be simply rewritten in term of h as follows:

$$\dot{h} = k_A - (k_A + k_D)h \qquad (3)$$

where the time derivative has been indicated as $\dot{\blacksquare} = d\blacksquare/dt$.

The activation and deactivation rates, k_A, k_D , are functions of the energy barriers ΔG_{A0}, ΔG_{D0} existing between the two stable conformation states of the cavitand molecule when no external actions are applied (**Figure 2.4**); typically, they are expressed through the Arrhenius equation as follows

$$k_{A0} = C_A\, \exp\left(-\frac{\Delta G_{A0}}{k_B T}\right), \qquad k_{D0} = C_D\, \exp\left(-\frac{\Delta G_{D0}}{k_B T}\right) \qquad (4)$$

where k_B, T are the Boltzmann constant and the absolute temperature, respectively, while C_A, C_D are the so-called frequency factors.[32]

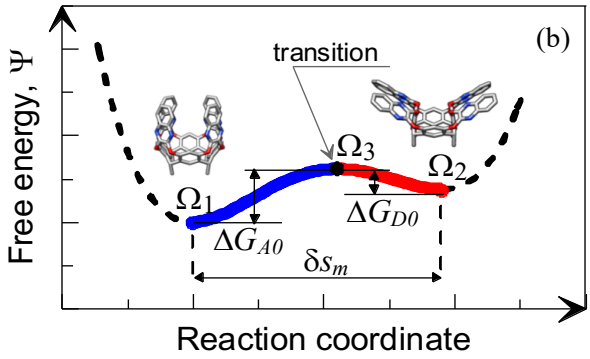

Figure 2.4. *Schematic of the free energy vs reaction coordinate; the two stable configurations of the cavitand (vase and kite) are indicated with Ω_1 and Ω_2, respectively.*

However, a mechanical force $\not{f}$ can affect the above-mentioned energy barriers, making the forward process (cavitand opening) favored and the backward one (cavitand closing) hindered.[33]

The increase of the forward and of the backward rates k_A, k_D, quantified with respect to their values in the unstressed state, k_{A0}, k_{D0}), can be expressed through the Arrhenius relationship as:

$$k_A = k_{A0}\ \exp\left(\frac{\not{f}\ \delta s_m}{k_B\ T}\right), \quad k_D = k_{D0}\ \exp\left(-\frac{\not{f}\ \delta s_m}{k_B\ T}\right) \tag{5}$$

being δs_m the size change of the molecule taking place between the close and the open state.[33,34]

2.2.2 Theoretical prediction of the Poisson's ratio

It is well-known that the Poisson's ratio (PR) of a material is defined only in the small deformation regime[34]; in the large deformation regime, the volume ratio $J = \det \boldsymbol{F}$ can be more conveniently adopted to quantify the volume change. A standard rubber usually has $\nu_0 \cong 0.5$ and, correspondingly, $J = 1$ because of its incompressibility (only isochoric deformations are possible); in other words, the volume ratio $J = V/V_0$ is constantly equal to 1 if the material cannot withstand volume variations. When a material is stretched along a given direction (say direction x) by an amount λ_x, it happens to be $J = \lambda_x$ when $\nu = 0$, while $J > \lambda_x$ when $\nu < 0$,

i.e. for an auxetic material the volume ratio is greater than the amount of the applied stretch.

In absence of any constraint, by applying the stretch λ_x the stretches $\lambda_y = \lambda_z$ arise in the material normal to the stretch direction. According to the Biot definition, the Poisson's coefficient *vs* the applied stretch λ_x is given by[35]:

$$\nu_{xy}(\lambda_x) = \nu_{xz}(\lambda_x) = \nu(\lambda_x) = -\frac{\lambda_y - 1}{\lambda_x - 1} = -\frac{\lambda_z - 1}{\lambda_x - 1} \qquad (6)$$

and results to be variable with the deformation. The Poisson's ratio becomes equal to the nominal PR ν_0, which is a characteristic value for any given material when the deformation tends toward zero, in the limit of no stretch applied, i.e. for $\lambda_x \to 1$. In other words, the standard or nominal Poisson's coefficient ν_0 is a material characteristic only for small deformations, while for large stretches it must be evaluated by using Eq. (6). According to our experimental measurements, the Poisson's ratio of the standard **PIM1** is equal to about $\nu_0 \cong 0.38$, obtained experimentally using Digital Image Correlation (DIC) technique (**Figure 2.5**).[36,37]

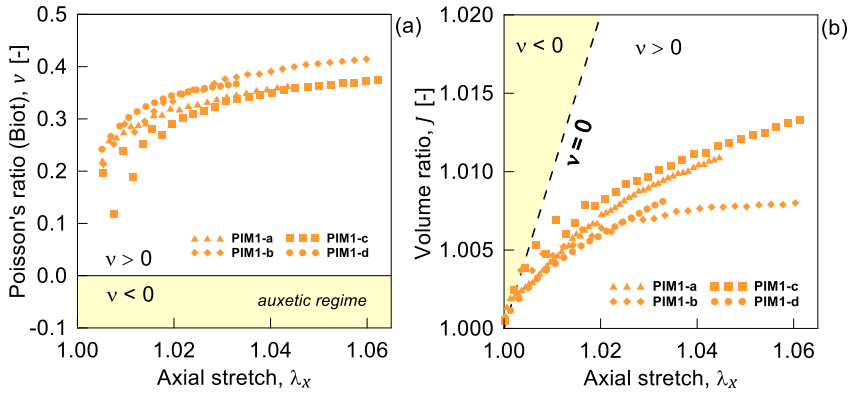

Figure 2.5. *DIC analyses of PIM1 specimens: (a): Average Poisson's ratio and (b) average volume ratio vs applied stretch* λ_x.

A simple micromechanical model to assess the Poisson's coefficient in PIM containing cavitand molecules can be defined according to the mechanism taking place at the chain network scale.

When the polymeric network is crosslinked to the cavitand molecules, their conformation change affects the deformation arising in the material; in this case, the above Eq. (6) has to be modified as follows:

$$\nu(\lambda_x) = -\frac{\lambda_{yt} - 1}{\lambda_x - 1} = -\frac{\lambda_{zt} - 1}{\lambda_x - 1} \tag{7}$$

where the total stretches λ_{yt}, λ_{zt} account for both the mechanical deformation and the deformation induced by the cavitand expansion effect.

We assume that the cavitand conformation change takes place at a critical microscopic stretch $\bar{\lambda}$ according to the following activation function $0 \leq h(\lambda_x) \leq 1$:

$$h(\lambda_x) = \frac{\exp\frac{(\lambda_x - \bar{\lambda})}{c}}{1 + \exp\frac{(\lambda_x - \bar{\lambda})}{c}} \tag{8}$$

where $\bar{\lambda}$, c are model parameters to be determined by fitting experimental data. In other words, the fraction of open cavitand molecules is zero if $\lambda_x \ll \bar{\lambda}$, it is $h = ½$ if $\lambda_x = \bar{\lambda}$, while $h(\lambda_x) \to 1$ when $\lambda_x \gg \bar{\lambda}$, while c defines the steepness with the applied deformation of the amount of cavitands switching from the *vase* to the *kite* state. When a uniaxial stretch λ_x is applied to a material whose Poisson's coefficient is ν, its volume ratio is expressed as:

$$J = \lambda_x - 2\nu(1 + \lambda_x) \tag{9}$$

As mentioned above, when microscopic deformations arise in the material such as in the case of cavitand molecules switching from the *vase* to the *kite* state, such a mechanism has to be considered using the total stretches in order to correctly evaluate the volume change.

Upon opening of all the cavitands (whose volume fraction is ϕ) contained in the generic volume V of material, the volume ratio of the polymer becomes:

$$J_n = \frac{V(1 - \phi) + \phi V J_{V-K}}{V} = 1 + \phi(J_{V-K} - 1) \tag{10}$$

In the above expression, $J_{V-K} = 2.62$ represents the volume ratio of a single cavitand molecule, i.e. the ratio between the final and the initial volume of a single molecule (**Figure 2.2b**). By considering that the cavitand molecules are homogeneously distributed in the polymer network and are randomly oriented in any direction of the 3D space leading to an isotropic material, the above-mentioned volume increase induces the following stretches in the polymer:

$$\lambda_{yc} = \lambda_{zc} = 1 + \phi\, h(\lambda_x)(\lambda_c - 1) \qquad (11)$$

where we have assumed the material to be mechanically stretched along the x-direction. The average cavitand stretch due to its *vase*→*kite* conformation change can be evaluated as $\lambda_c = J_n^{1/3}$.

Finally, the total value of the stretches arising in the material due to the combination of the externally applied stretch λ_x and to the cavitand opening are:

$$\lambda_{yt} = \lambda_y + (\lambda_c - 1), \qquad \lambda_{zt} = \lambda_z + (\lambda_c - 1) \qquad (12)$$

According to the above-described micromechanical model, upon opening of the cavitand molecules the Poisson's ratio starts from the nominal value $\nu_0 \cong 0.38$ and, by increasing the stretch, it rapidly decreases, reaching negative values (auxetic behavior, **Figure 2.2c**).

Based on the randomness of the cavitand arrangement within the polymer network due to its synthesis procedure, which does not introduce at the molecular scale any preferential direction in the material, in Eq. (7) it has been assumed that the Poisson's ratio is the same in the x-y and x-z planes, i.e. the material displays an isotropic 3D mechanical behavior.

The above-used total stretches λ_{yt}, λ_{zt}, taking place perpendicularly to applied stretch direction x, depend on both the applied deformation and on the cavitand switching from the *vase* to the *kite* conformation.

When all cavitands are already open, the fraction of the molecules in the *vase* conformation among all the cavitand molecules present in the unit volume (cavitand opening factor) is $h(\lambda_x) = 1$ **Figure 2.2c**, bottom. In this case, the cavitand opening mechanism does not provide any further microscopic expansion to the material; by

further increasing the applied stretch, the Poisson's ratio tends to reach that of the standard polymer without cavitand molecules (Eq. (6)). This happens because, for sufficiently high applied stretch values, the network deformation is not affected any more by the already completed cavitand expansion.

As can be observed from Eq. (8) and **Figure 2.2c**, the earlier the cavitand begin to open (small values of $\bar{\lambda}$ that defines the stretch at which half of the cavitands are open) the more auxetic is the material.

2.2.3 Experimental implementation of the theoretical model

To effectively transduce the mechanical stimulation in the expansion of the auxetons, these dimensionally variable units have been inserted as crosslinker in **PIM1** by covalently anchoring the four quinoxaline walls to the polymer backbone. To this purpose, a proper quinoxaline cavitand bearing eight hydroxyl groups at the upper rim (**Cv8H**) was synthetized in two steps starting from the corresponding hexyl-footed resorcinarene **Res[C_6H_{13}, H]**. The scaffold was initially bridged with 2,3-dichloro-6,7-dimethoxyquinoxaline (**Scheme 2.2**, upper) to form a quinoxaline cavitand with eight methoxy groups at the upper rim. Excision of the methyl groups gave the desired cross-linker **Cv8H** (**Scheme 2.2,** bottom).

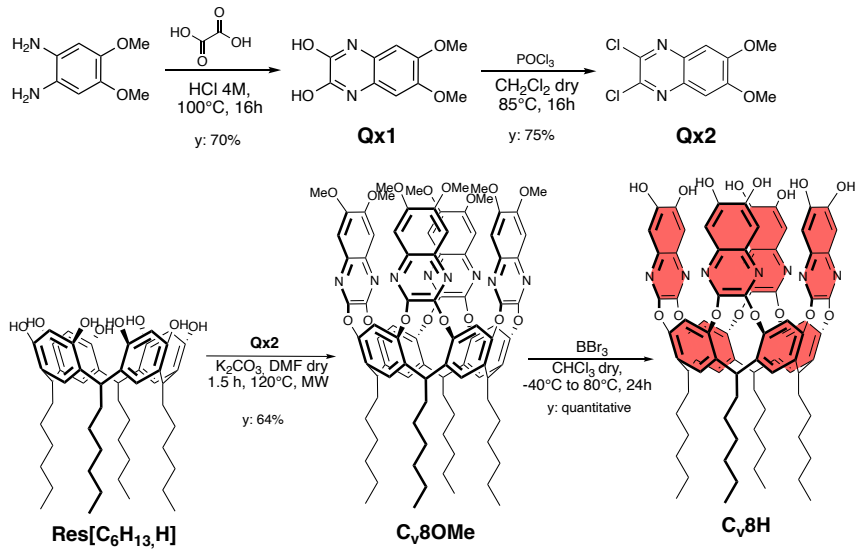

Scheme 2.2. *Synthetic pathway of **Qx2** (upper) and **Cv8H** (bottom, in red the cavitand crosslinker).*

The molecule was fully characterized by ^{1}H and ^{13}C NMR spectrometry and MS analysis (See Appendix, **Figure A1**, **A2**, **A3** respectively). The triplet of the methine protons of the resorcinarene scaffold at 5.70 ppm in ^{1}H NMR spectrum is diagnostic of the *vase* conformation of the cavitand in solution.[38] The corresponding fixed *kite* **CK8H** cavitand, used as control crosslinker, was prepared following the same synthetic procedure using **Res[C6H13, CH3]** as starting material (**Scheme 2.3**) and fully characterized (Appendix, **Figure 2.A4**, **2.A5**, **2.A6**).

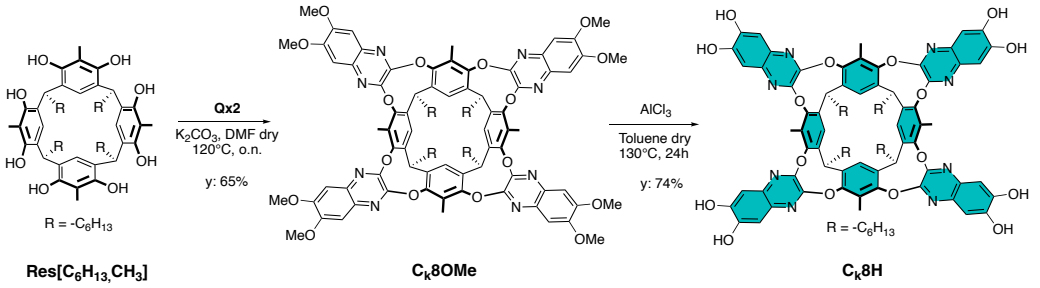

Scheme 2.3. *Synthesis of the fixed kite Ck8H cavitand.*

The introduction of four methyl groups in the apical position of the resorcinarene forces the corresponding cavitand to assume a blocked *kite* conformation, as confirmed by the shift of the methine signal at 3.60 ppm in ^{1}H NMR spectrum.[27,39] Crystals structure of the precursor **C$_v$8OMe** and **C$_k$8OMe** were obtained, to confirm unambiguously the conformation also in the solid state. In particular, the *vase* cavitand **C$_v$8OMe** crystallizes in the space group *P*-1 with two independent molecules in the asymmetric unit (the atoms of the four walls are labelled A, B, C and D in molecule 1, and E, F, G and H in molecule 2). The two molecules mainly differ for the positions of the alky chains (some of which are disordered over two different orientations) and of the four cavitand walls. **Figure 2.6** and **Figure 2.7** show some perspective views of molecules 1 and 2, respectively. Solvent molecules and alkyl chains have been omitted for clarity. The heigh of the cavity can be measured as the distance from the mean plane passing through the eight oxygens atoms O1/O2 (lower rim) and the eight oxygen atoms O22/O23 (upper rim). This distance is of 7.091(3) and 7.125(2) Å for molecule 1 and 2, respectively.

At the upper rim, the cavity entrance has the shape of a distorted parallelogram; in the case of molecule 1 it is roughly of dimensions 8.2(1) Å x 10.1(2) Å for molecule 1 and 8.5(3) Å x 10.0(4) Å for molecule 2.

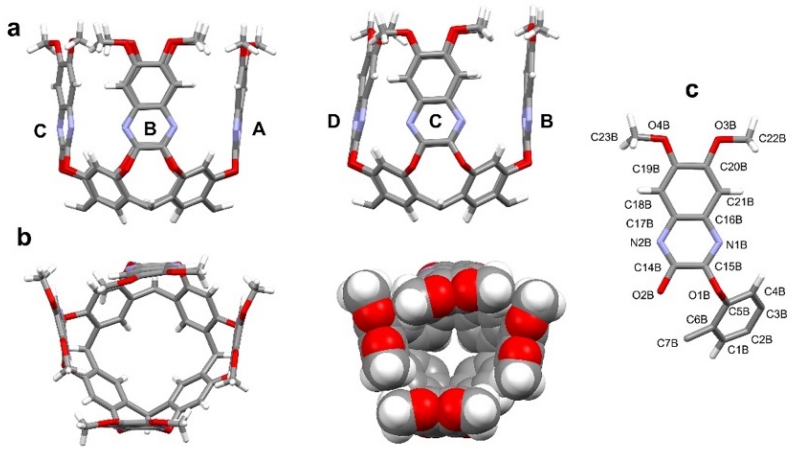

Figure 2.6. *Perspective view of* ***Cv8OMe*** *(molecule 1). a) lateral views; b) top views in capped stick and space filling mode; c) example of labelling scheme for one fourth of the cavitand.*

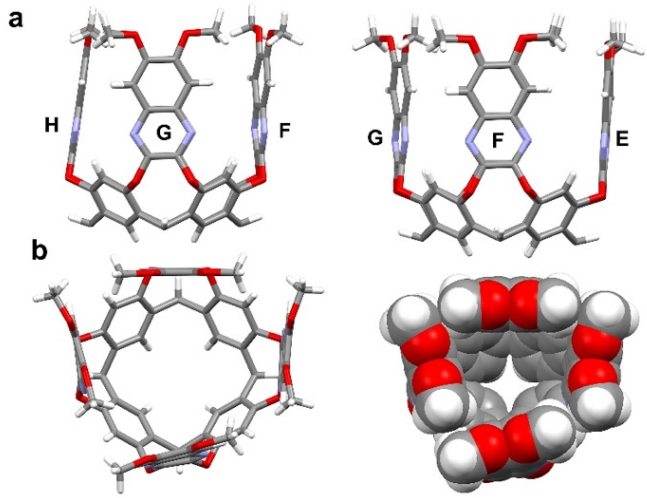

Figure 2.7. *Perspective view of* ***Cv8OMe*** *(molecule 2). a) lateral views; b) top views in capped stick and space filling mode.*

The *kite* cavitand **Ck8OMe** crystallizes with four independent molecules in the asymmetric unit (See **Figure 2.8**, DMSO molecules and chains are omitted for clarity) which tend to form π-π stacking between the aromatic walls. The geometrical parameters that give an idea of the dimensions of this cavitand are the distances between: C23A···C22B (18.1 Å), C23C···C22D (17.9 Å), C23A···C22D (15.4 Å) and

C22B···C23C (15.3 Å). The other three molecules show distances in the same ranges. In **Figure 2.9** are reported some perspective views of molecules **Cκ8OMe**.

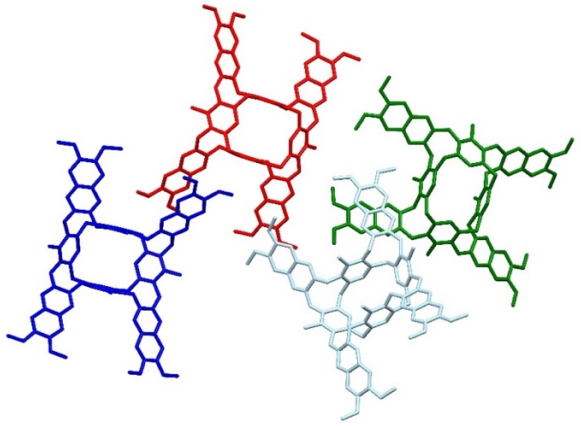

Figure 2.8. *View of the four independent molecules of* ***Cκ8OMe.***

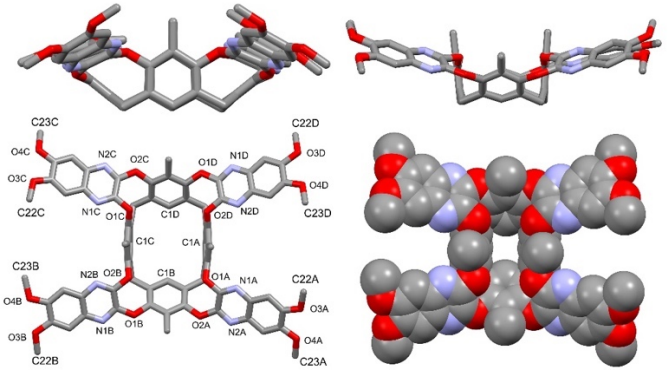

Figure 2.9. *Perspective view of one of the four independent molecules in* ***Cκ8OMe****. Above: lateral views; below, top views in capped stick (with labelling scheme) and space filling mode.*

The synthesis of the crosslinked network **PIM1-Cv8H** was conducted by adapting the standard **PIM1** recipe (**Figure 2.3a**, red and yellow product).[40] Considering that **Cv8H** has twice as many functional groups of **TTSBI**, the starting molar ratio of **TTSBI**/**Cv8H** was set to 0.92/0.04, corresponding to ≈12% w/w of auxeton in the final **PIM1-Cv8H**. The detailed synthetic procedure is reported in the experimental section. The same procedure was employed to prepare **PIM1-Cκ8H**, by replacing the

vase cavitand **Cv8H** with its fixed *kite* analogue **Cκ8H (Scheme 2.4**, blue and yellow product).

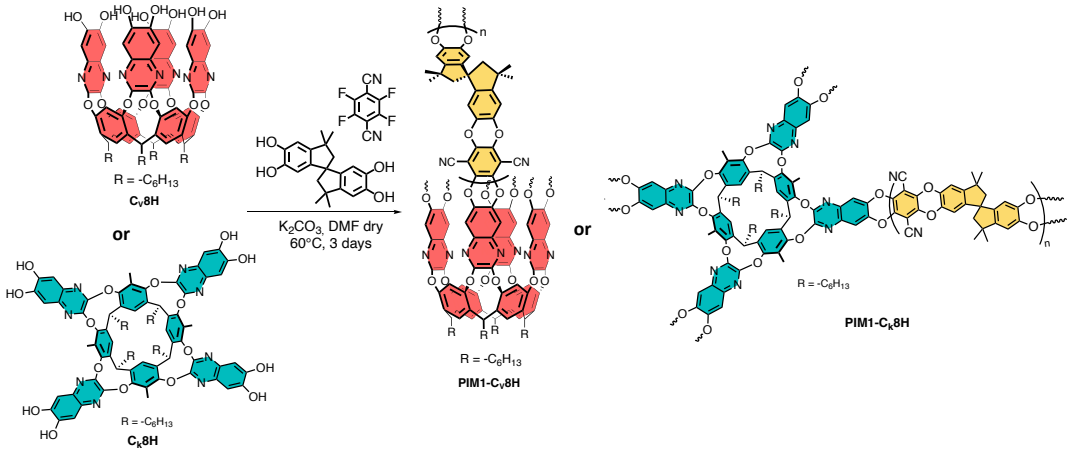

Scheme 2.4. *Synthesis of **PIM1-Cv8H** (red cavitand) and **PIM1-Cκ8H** (blue cavitand). Only one of the four polymer connections is shown for clarity.*

The effective embedding of **Cv8H** into the **PIM1** matrix was confirmed by IR spectroscopy, comparing the spectra of **PIM1-Cv8H**, **PIM1** and **Cv8H** (see Appendix, **Figure 2.A7**). Indeed, typical nitrile stretching at 2240 cm^{-1} of **PIM1** and the -C=N-C- peak at 1572 cm^{-1}, referred to the quinoxaline walls, are both present in the final polymer.

The presence and the amount of cavitand in the crosslinked polymer was evaluated via XPS analyses (**Figure 2.10**) from the study of the N1s core levels.

Contrary to **PIM1**, which possesses only the nitrogen species relative to the nitrile -C≡N, **PIM1-Cv8H** shows an additional photoemission referred to the quinoxaline ring nitrogen -C=N-. The upper graph in **Figure 2.10** shows the N1s core level for **PIM1**; the main peak at about 399.50 eV (full width at half-maximum FWHM = 1.5 eV) is related to nitrile groups.[41]

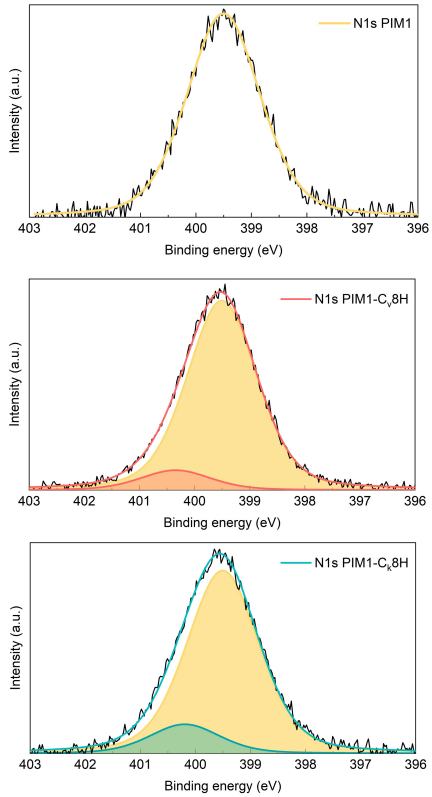

Figure 2.10. *N1 core levels XPS analysis of* ***PIM1****,* ***PIM1-Cv8H*** *and* ***PIM1-Cκ8H*** *showing the two different photoemission peaks related to the quinoxaline (orange and blue) and nitrile (yellow) nitrogen atoms.*

The N1s core level analysis of **PIM1-Cv8H** and **PIM1-Cκ8H** are shown in **Figure 2.10** (middle and bottom graph): the main component, related to nitrile groups observed in **PIM1**, is still located at 399.50 eV (FWHM 1.5 eV), while a second weak component is present at about 400.25 eV (FWHM 1.5 eV). The latter is related to the quinoxaline C=N-C species in **PIM1-Cv/κ8H**, as already observed in quinoxaline-based molecules[42,43] and cavitand bearing polythiophenes.[44] This second peak is the evidence of the cavitand presence in the polymer, while the intensity ratio between the two components determines the amount of **Cv/κ8H** crosslinker effectively incorporated into **PIM1-Cv/κ8H**.

For **PIM1-Cκ8H** this value mirrors the molar ratio of the monomers in the reaction medium, while the percentage of **Cv8H** inserted in the **PIM1-Cv8H** polymer is estimated in 8.0 % w/w.

The N1s photoemission signal must be normalized by the number of emitting nitrogen atoms for a proper quantification. Considering that homogeneous **PIM1-Cv8H** polymeric units P are analyzed, the N1s signal of **Cv8H** originated by $8\,P$ nitrogen atoms. At the same time, **PIM1** signal derives from $2\,n\,P$ nitrogen atoms, where n is the number of **PIM1** units (yellow part in **Figure 2.10**) for each cavitand. Thus, the intensity ratio between the two peaks is:

$$n = 4 \cdot \frac{Int_{PIM1}}{Int_{CAV}} \tag{13}$$

The maximum error for n is about ±10%, mainly due to the uncertainty for the weak quinoxaline C=N-C component area. Thus, we conclude that the crosslinked **PIM1-Cv8H** and **PIM1-Cκ8H** have about 38 and 26 **PIM1** units for each cavitand respectively (**Table 2.4**), i.e., about 9 and 6 monomers for each "wing", provided that the polymer structure is homogenous in the analyzed film.

Table 2.4. *Number of **PIM1** monomers for each cavitand calculated from the N1s core level analysis for the two crosslinked polymers.*

	Exp. Int_{PIM}/Int_{CAV}	**n, PIM monomers (±10%)**
PIM1-C_V8H	9.5	38.1±4
PIM1-C_K8H	6.5	25.9±3

We can speculate that the lower reactivity of **Cv8H** compared to **Cκ8H** is due to steric reasons, i.e. to the closed proximity of the OH groups in the reacting cavitand. Traces of fluorine (<1%) were detected in all samples, related to the presence of a small amount of **DFTPN** as terminal unit.

The thermal stability of **PIM1-Cv8H** was determined via thermogravimetric analysis (TGA, **Figure 2.11**). A small weight loss, ascribable to the presence of residual solvent trapped in the pores, was observed at temperature below 200 °C, followed by thermal

degradation around 400 °C, which is in line with the TGA profile of pristine **PIM1** (**Figure 2.11**, yellow line).

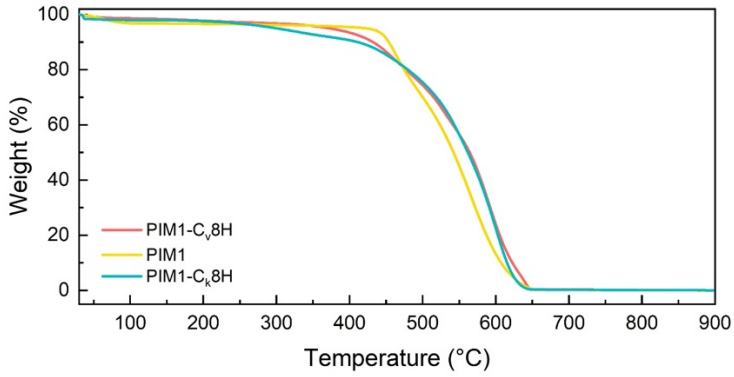

Figure 2.11. *TGA curves of PIM1, PIM1-Cv8H and PIM1-Cκ8H.*

PIM1 films were prepared by solvent casting from chloroform solutions. A film of pristine **PIM1** (M_w=79 kDa; PDI=1.5) was prepared for blank experiment dissolving 1.3 g of **PIM1** in 25 mL of chloroform. The solvent was allowed to slowly evaporate at room temperature over 48 hours. Crosslinked **PIM1-Cv8H** and **PIM1-Cκ8H** are insoluble in solvents commonly used for **PIM1**, jeopardizing the formation of the corresponding films via solvent casting. To overcome this problem, a blending strategy[45] was selected for the preparation of crosslinked films, consisting in mixing a dispersion of **PIM1-Cv8H** in chloroform with a solution of **PIM1** in the same solvent (**Figure 2.12**).

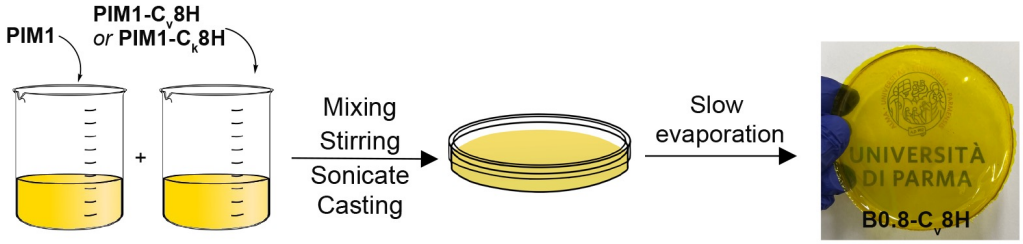

Figure 2.12. *Scheme of the blends preparations and picture of* ***B0.8-Cv8H****.*

Four different blends were prepared to investigate the effect of the quantity of cavitands present in the network on its auxeticity, named **B0.1-Cv8H, B0.4-Cv8H, B0.8-Cv8H, B1.2-Cv8H**. The number after the letter B (blend) is referred to 0.1, 0.4, 0.8, 1.2% w/w of **PIM1-Cv8H** portion in the final film. The quantity of each component used for the blends and the blend preparation procedure are reported in the experimental section. **B1.2-Cκ8H** was prepared accordingly. Defects start to appear in the films upon increasing the amount of crosslinked polymer in the blend, resulting in opacity for the more concentrated **B1.2-Cv8H** (**Figure 2.13**). On the contrary, **B1.2-Cκ8H** remained transparent (**Figure 2.13f**). Therefore, **B1.2-Cv8H** will not be discussed from now onward.

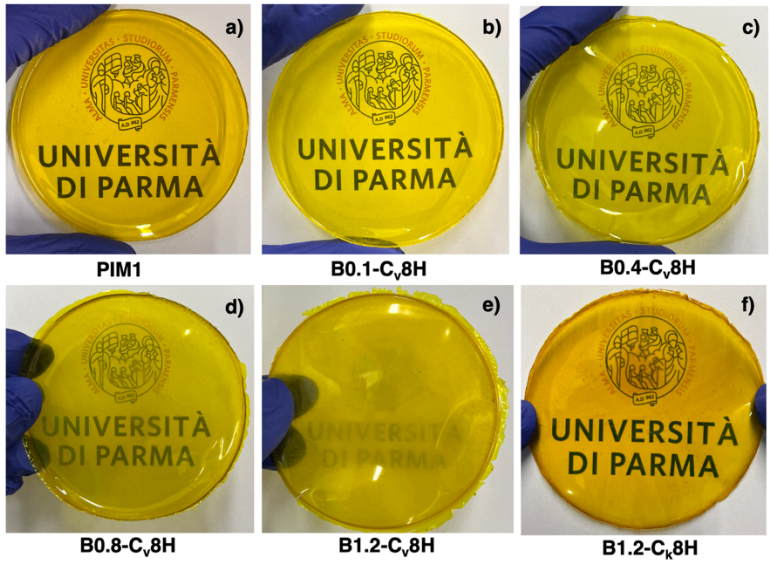

Figure 2.13. *Photographs of: a)* ***PIM1*** *film, b-e) blends prepared via blending approach containing different portions of* ***PIM1-Cv8H.*** *It is visible, increasing the amount of crosslinked fraction in the blend, more defects appear in the film, thus resulting in opacity trend, f) blend with* ***PIM1-Cκ8H****.*

The blends morphology was investigated by scanning electron microscopy (SEM). The cross sections were obtained by freeze fracturing the specimens (**PIM1**, **B0.4-Cv8H**, **B0.8-Cv8H**, **B1.2-Cκ8H)** in liquid nitrogen and the relative images are provided in **Figure 2.14**, all the magnification are reported in the Appendix**, Figure 2.A8**.

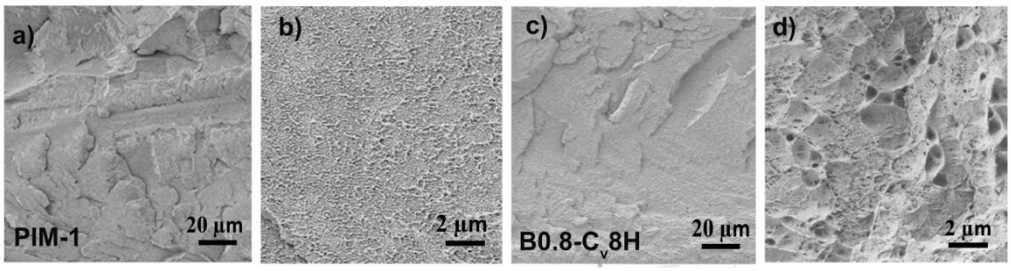

Figure 2.14. *a, b) SEM images of fractured* ***PIM1*** *at different magnifications; c,d) SEM images of fractured* ***B0.8-Cv8H*** *at different magnifications.*

None of the samples shows macro- or mesoscopic defects along the cross section, indicating the formation of a dense material. As highlighted in **Figure 2.14 a-d**, at higher magnification **PIM1** presents a jagged pattern, while blends have a more rough/corrugated structure, with alveoli surrounded by the same **PIM1** microstructure.

2.2.4 Experimental evidence of auxeticity and quantitative prediction of the observed auxeticity

The predicted *vase*-to-*kite* conformational switch responsible for the NPR in the material, triggered by tensile elongation, is sketched in **Figure 2.15**.

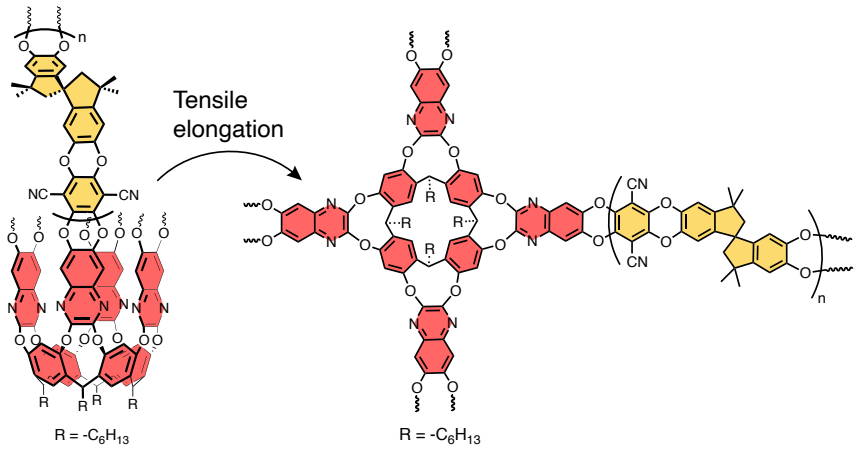

Figure 2.15. *Molecular representation of vase to kite conformational switch triggered by tensile elongation.*

Mechanical tests were performed by stretching the polymer specimens, prepared in the shape of thin strips (size 10 x 50 x 0.2 mm). Tensile tests until the final failure as well as tensile cyclic tests were performed on at least three specimens of the same blend. The elastic modulus of the blends is comparable to that of pristine **PIM1**.

PIM1 shows a greater decrease of the tangent Young's modulus with the deformation (**Figure 2.16,** top), while the blend tends to have a more linear elastic behavior (slight decrease of the tangent Young's modulus with the applied deformation, **Figure 2.16**, bottom) and results to be more brittle, showing a lower maximum deformation at failure. The deformation was applied at a small rate equal to $\dot{\lambda}_x = 5 \cdot 10^{-4}\ s^{-1}$. Pictures of the sample at equally spaced time instants were taken with a high-resolution camera, and then used in DIC to obtain the strains of the material in the stretched and in the transversal direction (**Figure 2.17a**).

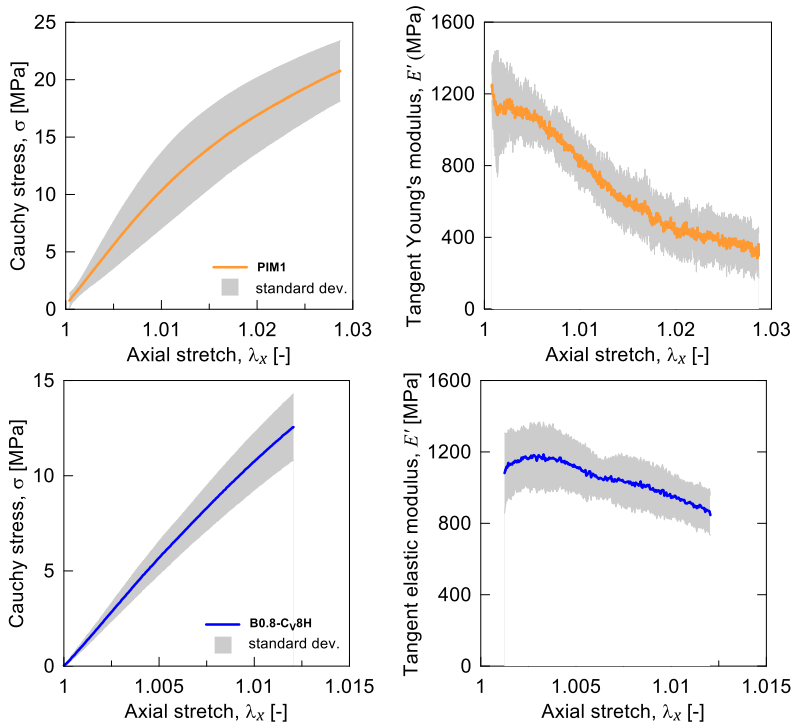

Figure 2.16. *True Cauchy stress (left) and tangent elastic modulus (right) vs stretch for the standard **PIM1** (top) and for **B0.8-Cv8H** (bottom) specimens.*

The prediction of the Poisson's ratio through the theoretical micromechanical model is performed firstly by determining the parameters $\bar{\lambda}$, c; they are used in Eq. (8) for

calculating the fraction h of cavitand molecules switched from the *vase* to the *kite* conformation at a given applied stretch level λ_x. In particular, the above-mentioned values were determined by best fitting the average experimentally determined Poisson's ratio vs stretch curve of the case **B0.8-Cv8H** and resulted to be: $\bar{\lambda} = 1.002$, $c = 0.005$. These values were adopted for estimating the Poisson's ratio as follows:

- The average stretches λ_c of the cavitand molecules are evaluated by using Eq. (12), where $J_{V\text{-}K} = 2.62$ (**Figure 2.2b**), ϕ is the volume fraction of the cavitand molecules in the polymer, and h is determined as detailed in Eq. (8);
- The stretches $\lambda_{yc} = \lambda_{zc}$ arising in the material due to cavitand molecules opening are determined by using Eq. (11);
- The total stretch λ_{yt} (i.e. due to mechanical deformation and to the cavitand opening) in direction γ is determined through Eq. (13);
- The Poisson's ratio $\nu(\lambda_x)$ is finally determined by using Eq. (1).

The DIC experimental NPR trend of the best performing blend **B0.8-Cv8H** is reported in **Figure 2.17b** (left) for three different film specimens, while the corresponding volume ratio is shown in **Figure 2.17b** (right). The volume ratio of **PIM1**, polycarbonate (PC) and polymethylmethacrylate (PMMA) are outlined for comparison.[46]

In **Figure 2.17c** the average Poisson's ratio values determined from DIC measurements are illustrated for three different cases, namely **B0.1-Cv8H** (0.1% w/w), **B0.4-Cv8H** (0.4% w/w), and **B0.8-Cv8H** (0.8% w/w). Blend **B1.2-Cv8H** is excluded because its inhomogeneity led to irreproducible NPR values (**Figure 2.17d**), even if the trend of larger NPR upon increased cavitand content is respected. For the first two cases, a simple tensile test has been performed, while two identical tensile cycles (each one up to the maximum deformation $\varepsilon_x = 1\%$) have been applied to the specimen made of **B0.8-Cv8H**. The case with 0.1% crosslinking auxeton does not show any auxeticity, while for the polymer **B0.4-Cv8H** NPR emerges for small deformation values and quickly disappears as the applied stretch increases.

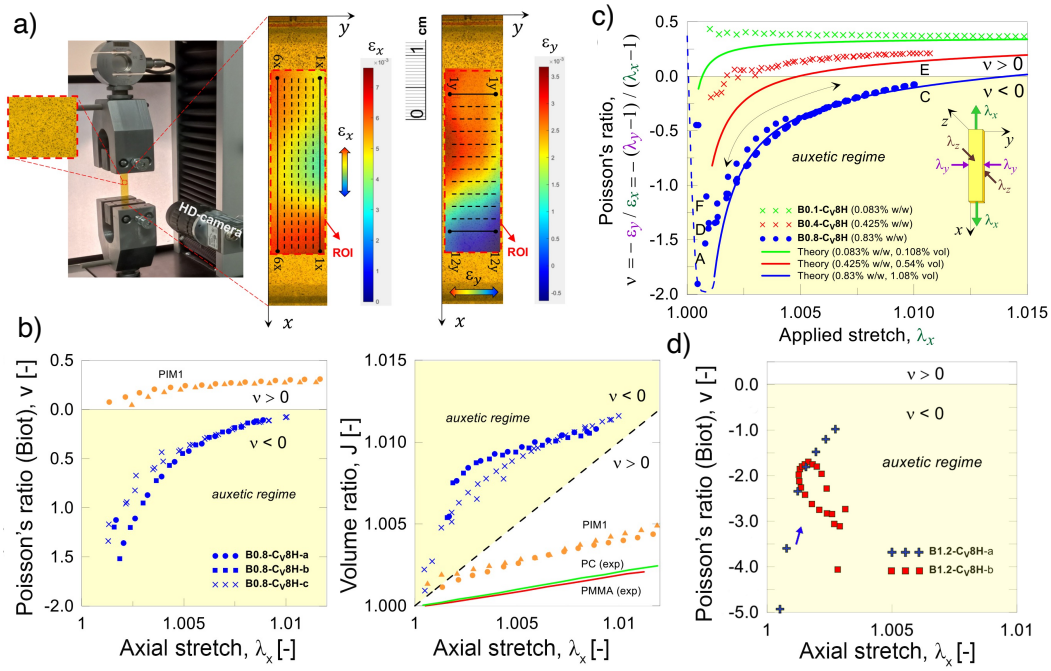

Figure 2.17. *a) Mechanical Test setup with the high-resolution camera for the DIC elaboration (left). DIC images of the specimen showing the longitudinal and transversal strain maps determined in the Region Of Interest (ROI, right); virtual strain gauges are sketched as dashed lines; b) Trend of the NPR and of the volume ratio vs the applied stretch for* ***PIM1*** *and* ***B0.8-Cv8H*** *specimens; c) Comparison of the average Poisson's ratio vs the applied stretch* λ_x *obtained from experimental tests and that provided by the theoretical model for different cavitand molecule contents (0.1% w/w; 0.4% w/w; 0.8% w/w). The corresponding volume fractions of the cavitand molecules are also indicated. The specimens* ***B0.1-Cv8H*** *and* ***B0.4-Cv8H*** *were tested under simple uniaxial tension, while the specimen* ***B0.8-Cv8H*** *was tested under two identical uniaxial stretch cycles (letters A-C-D-E-F, see* ***Figure 2.21b****); d) DIC analyses of* ***B1.2-Cv8H*** *on two different specimens showing irreproducible and anomalous NPR trend.*

Finally, the case **B0.8-Cv8H** shows a quite large NPR (up to about -2) for low values of the applied deformation; proceeding further with stretching the material, the Poisson's ratio increases and tends to the value typical of the **PIM1** polymer. The maximum auxeticity appears for low values of the applied deformation due to transversal deformation caused by the cavitands opening, which is larger in comparison to the axial stretch. As far as the longitudinal stretch increases, the cavitands molecules are almost all open and their expansion effects is not effective any more to induce the auxetic response. The application of two identical tensile

cycles of **Figure 2.17c** for the case **B0.8-Cv8H** has been performed to prove the reproducibility of the NPR response. It is worth mentioning that for very low values of the applied deformation ($1 \leq \lambda_x <\approx 1.001$), the determination of the Poisson's ratio is not reliable due to the excessively small values of the displacements, which cannot be precisely managed by the DIC measurements. The theoretical fitting performed through the model illustrated above are reported in **Figure 2.17d** with continuous lines; both the trend and the determined values are in satisfactory agreement with the experimental outcomes. The theory provides the same increasing trend of the Poisson's ratio with increasing the applied axial deformation; in the case of **B0.8-Cv8H**, the Poisson's ratio negativity ends when the applied deformation is roughly equal to $\lambda_x \approx 1.015$.

Due to the thin conformation of the specimen lying on the *x*-*y* plane, the deformation on the *y*-*z* plane cannot be determined from the DIC measurements. These polymers are processable only via solvent or freeze casting leading to films of limited thickness (<1 mm),[47] not compatible with DIC analysis, which requires a thickness of at least 3-4 mm. However, due to the randomness of the spatial orientation of the cavitand molecules crosslinked to the polymer backbone, the measured transversal deformation λ_y is expected to be the same of that taking place along the other transversal direction *z*, namely λ_z. Albeit presently not experimentally measurable, the emerging auxetic behavior is potentially tridimensional, leading to a 3D molecular auxetic.

The auxetic behavior, ascribable to the *vase* to *kite* interconversion of the cavitand crosslinker, can be also evaluated via spectroscopic analyses exploiting the different emission wavelengths of the two conformers.[48]

UV-Vis absorption and emission spectra of **PIM1** and **Cv8H** were first performed in chloroform and THF respectively. The cavitand **Cv8H** presents a maximum of absorption (λ_{max}) at 340 nm in a window of transparency for the matrix PIM1 (**Figure 2.18a**). The emission spectra in solution of **PIM1** and **Cv8H** show only one main peak (**Figure 2.18b**). With the aim to selectively excite the cavitand when embedded into the polymeric matrix to observe a shift of the wavelength once stretched, solid-state

fluorescence measurements were performed on **B0.8-Cv8H** and **B1.2-Cκ8H**, exciting the system at 340 nm. Both blends present one emission peak at 515 nm and a shoulder around 480 nm (**Figure 2.18c**). Deconvolution of the profile give rise to two different bands: the main peak is attributed to **PIM1** emission while the secondary peak is related to the *vase*/*kite* cavitands present in the polymeric matrix. Regrettably, the wavelengths emission of the two deconvoluted peak is the same making the *vase* and *kite* conformations undistinguishable. Moreover, part of the emission of the polymers tested is "auto-absorbed" by the PIM1 matrix itself (**Figure 2.18c**, grey line), thereby making fluorescence not suitable technique to follow the auxetic behavior.

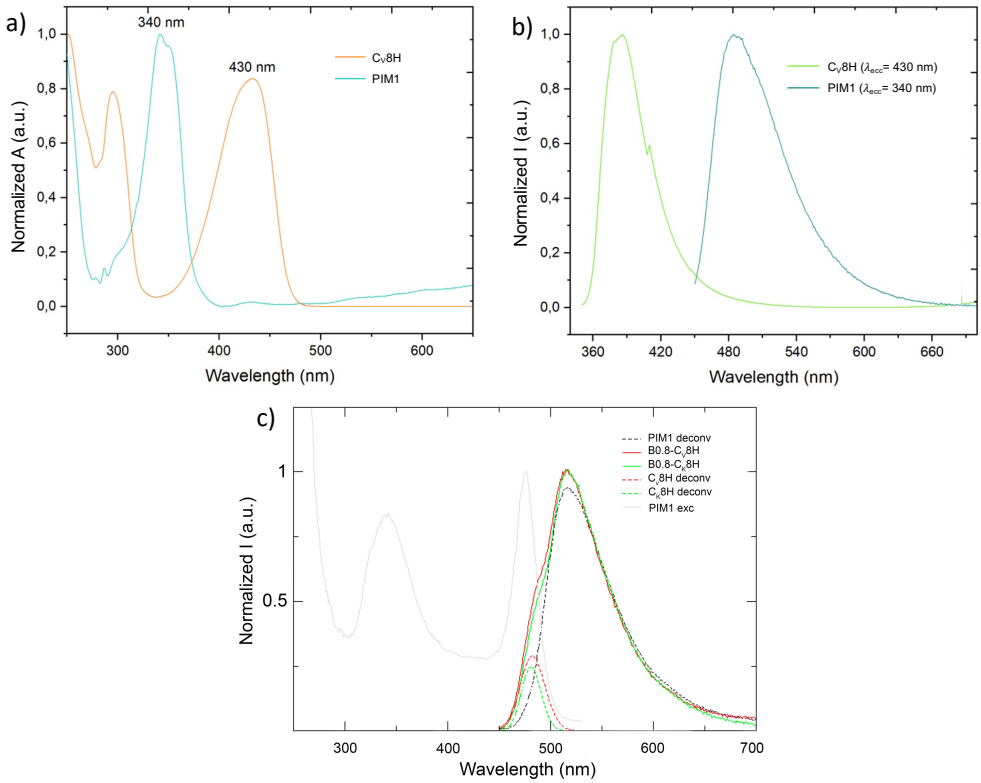

Figure 2.18. *a) UV-Vis absorption spectra of **PIM1** and **Cv8H** in solution; b) emission profiles of **PIM1** and **Cv8H** in solution; c) solid-state emission profile of **B0.8-Cv8H** (red line), **B1.2-Cκ8H** (green line). Deconvolution spectra of the curve are reported with dotted lines.*

2.2.5 Control experiments

Two control experiments have been devised and conducted to prove that the auxetic behavior of **PIM1-Cv8H** is solely due to the mechanically driven conformational expansion of the cavitand crosslinker. The first control experiment was implemented to prove that covalent crosslinking of the auxeton through the quinoxaline wings is necessary to induce the conformational switch. To this purpose, *vase* and *kite* cavitands lacking of hydroxyl groups at the upper rim (**Cv** and **Cκ**, respectively) were homogenously dispersed in **PIM1** in a 1% w/w ratio to give **PIM1-Cv** and **PIM1-Cκ** respectively (**Figure 2.19**).

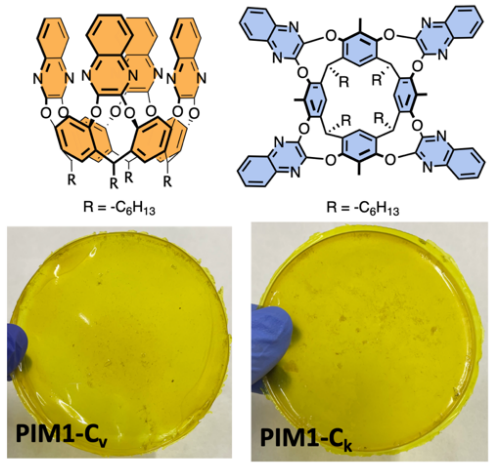

Figure 2.19. *Chemical structure of* ***Cv*** *and* ***Cκ*** *(top) dispersed in* ***PIM1*** *control film (bottom).*

The corresponding specimens were prepared and tested. In both cases no auxetic behavior was observed, with measured Poisson's ratio values close to the value ν_0 of pristine **PIM1** and a volume ratio trend typical of a non-auxetic material (**Figure 2.20a**).

A second, more demanding control experiment was devised to prove that the cavitand molecular expansion is the origin of auxeticity. This test required the synthesis of **PIM1-Cκ8H** and its blending with **PIM1** in a 10% w/w ratio, to give **B1.2-Cκ8H** (**Scheme 2.4**), to compare with **B0.8-Cv8H**, the best performing auxetic blend. The introduction of four methyl groups in the apical position of the resorcinarene scaffold

forces the corresponding cavitand to assume the blocked *kite* conformation,[27] rendering **B1.2-Cκ8H** the perfect candidate for the test. The results of the DIC analyses on three stretched specimens are reported in **Figure 2.20b**. None of them showed auxetic behavior, validating the cavitand conformational switching as the unique source of the material auxeticity.

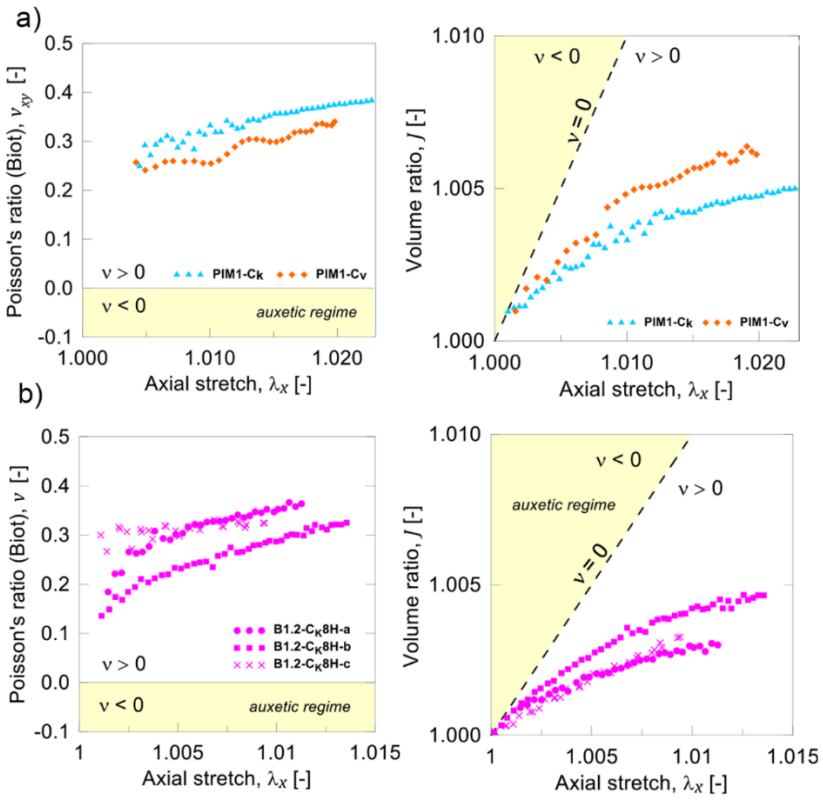

Figure 2.20. *a) PIM1 specimens with dispersed cavitand molecules both in the vase (**PIM1-Cv** red dots) and in the kite (**PIM1-Cκ** blue dots) conformations. Poisson's ratio (left) and average volume ratio (right) vs the applied stretch λx determined from DIC analyses; b) **B1.2-Cκ8H** specimens with crosslinked cavitand molecules in the kite conformations. Poisson's ratio (left) and volume ratio (right) vs the applied stretch λx determined from DIC analyses for three tested specimens.*

2.2.6 *Reversibility of the auxetic behavior*

In order to verify the reversibility of the auxetic response induced by the crosslinking auxeton, cyclic tensile tests were performed. In particular, **B0.8-Cv8H** was tested by applying two subsequent cycles in which the specimen has been deformed with a

constant stretch rate up to about a longitudinal deformation equal to λ_x = 1.01 (A-C), then unstretched to zero (C-D), followed by an identical second deformation cycle (D-E-F, **Figure 2.21b**).

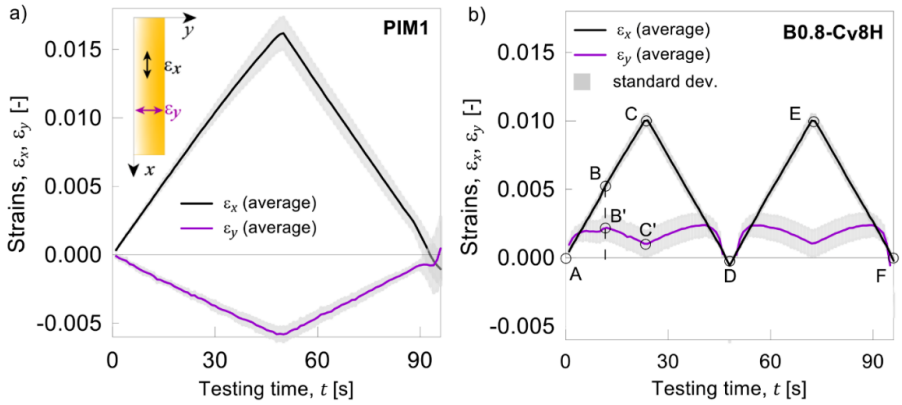

Figure 2.21. *Average strain $\varepsilon_y = \lambda_y - 1$ determined from experimental tests vs the applied stretch $\varepsilon_x = \lambda_x - 1$. a) Standard **PIM1** subjected to one stretch cycle; b**) B0.8-CV8H** subjected to two stretch cycles. It can be noted that under an applied tensile (positive) deformation ε_x the transversal deformation ε_y is negative (contraction) for **PIM1**, while it is positive (expansion) for **B0.8-Cv8H**. The reversibility of the deformation is clearly visible, being the two deformation cycles almost identical. The standard deviation shown in the figure is evaluated by using the measurements provided by the virtual extensometers of the DIC analysis (6 in x-direction and 12 in y-direction, see **Figure 2,17a**) placed on a single specimen.*

The behavior of **B0.8-Cv8H** is compared to that of **PIM1**, for which one single deformation cycle was applied (**Figure 2.21a**). The strains in the longitudinal (ε_x) and transversal (ε_y) directions were determined from DIC measurements; the average value and the standard deviation of the strains were determined by using several measurements done within the ROI area (**Figure 2.17a**).

The transversal deformation of the **PIM1** specimen results to be negative (pink curve **Figure 2.21a**), indicating a contraction of the material, while for the **B0.8-Cv8H** specimen the transversal deformation results to be positive (pink curve **Figure 2.21b**), corresponding to an expansion of the material transversally to the tensile direction (auxetic behavior). It is worth noting that for the **B0.8-Cv8H** specimen the transversal deformation increases (part A-B' in **Figure 2.21b**) by stretching the

material up to certain value, then it slightly decreases (part B'-C' in **Figure 2.21b**) even if the material is further stretched (B-C). This is due to the early opening of the cavitand molecules, which occurs for low stretching values. As soon as all the cavitand molecules are open, the macroscopically detectable expansion is not promoted anymore by the auxeton and the material starts behaving as a standard **PIM1** specimen, so the transversal deformation decreases. Upon unstretching (C-D), the longitudinal deformation decreases and the transversal one increases a little and then goes back to zero (point D in **Figure 2.21b**). During the second cycle (D-E-F), the same trend was observed, confirming that the conformational opening/closing mechanism of the cavitand molecules is fully reversible. This behavior is confirmed also by observing the Poisson's ratio vs stretch curve reported in **Figure 2.17d**: upon stretching and unstretching the trend of the curve $\nu(\lambda_x)$ is almost superimposable during the two subsequent cycles. A more extensive stretch cycling test has been conducted on a **B0.8-Cv8H** specimen to test more thoroughly the reproducibility of NPR behavior upon repeated loading cycles.

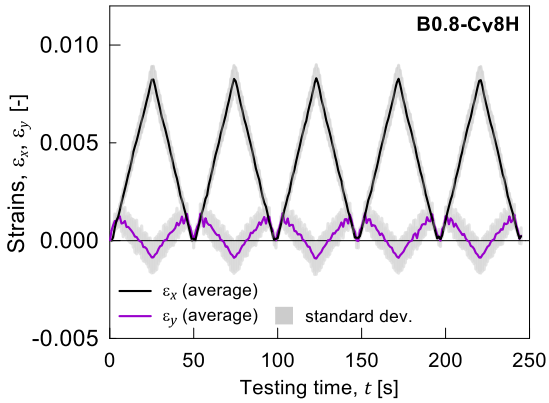

Figure 2.22. *Average strain $\varepsilon_y = \lambda_y - 1$ determined from experimental tests vs the applied stretch $\varepsilon_x = \lambda_x - 1$. **B0.8-Cv8H** subjected to five stretch cycles. It can be noted that under an applied tensile (positive) deformation ε_x the transversal deformation ε_y is is positive (expansion). The reversibility of the deformation is clearly visible, being the two deformation cycles almost identical. The standard deviation shown in the figure is evaluated by using the measurements provided by the virtual extensometers of the DIC analysis (6 in x-direction and 12 in y-direction, see **Figure 2.17a)** placed on a single specimen.*

The results, shown in **Figure 2.22** for five runs, confirm the complete reversibility of the auxetic behavior.

2.3 Conclusions

The long-standing problem of generating artificial molecular auxetics has now a promising solution. The proposed auxetic polymer does not mimic metamaterials at the molecular level like rotating triangles,[49] egg rack structures[50] or reentrant honeycombs.[51] Instead, it relies on a completely novel approach of mechanically-driven conformational expansion of a cavitand, which has the unique property to switch between two well-defined conformations: the compact *vase* and the extended *kite*. The macroscopic expression of cavitands conformational expansion is obtained by introducing the cavitand auxetic unit as crosslinkers in a PIM. In this way, the two discrete conformational states of the cavitand provide the desired kinematic response responsible of the NPR at the macroscopic level.

The **PIM1** polymer matrix presents a rigid structure capable to transfer the mechanical stress into a conformational expansion of the crosslinking unit. The conformational expansion propagates to the polymer backbone, triggering the NPR in the material. On the cavitand side, the direct covalent linking of the quinoxaline wings to the PIM structure combined with its conformational flexibility are the requirements to be mechanically responsive, as proven by the two control experiments. At present, the NPR has been experimentally measured in the *x-y* plane only and not in the *x-z* plane, since the blends are processable only via solvent casting, leading to films of no more than 200-220 μm thickness (**Figure 2.A8**). The DIC technique requires a thickness of at least 3-4 mm for reliable NPR evaluation. Nevertheless, being the cavitand molecules randomly oriented in the polymer network, the material can be reasonably assumed to be isotropic from the mechanical viewpoint. Therefore, **PIM1-Cv8H** is expected to behave as 3D molecular auxetic, according to the prediction provided by the developed theoretical model.

The auxeton micromechanical model proposed is able to match both the observed experimental NPR values and the kinematic behavior of the material, validating the

cavitand conformational expansion as the origin of the auxeticity. The agreement of the theory with the experimental data bodes well for the use of this model to design other auxetic materials and predict their NPR values.

Finally, the complete reversibility of the auxetic response singles out this material as promising candidate for the fabrication of auxetic objects. Work is in progress to obtain the solution processable version of this auxetic PIM, overcoming the processability limits of the present material.

Acknowledgements

Thanks to prof. Francesca Terenziani from University of Parma for the helpful interpretation of the spectroscopic analyses on solid state samples. Special thanks to prof. Chiara Massera and Dr. Marchetti Danilo from University of Parma for the crystallographic data and structure provided. Thanks to Dr. Andrea Faccini of Centro Intefacoltà di Misure "G. Casnati" of the University of Parma for high-resolution MALDI-TOF MS analyses

2.4 Experimental procedures

2.4.1 Materials and methods

All reagents and solvent were purchased from certified commercial sources and used as received, without further purification. For the synthesis, all solvents were dried and distilled according to standard procedures known in the literature.[52]

NMR spectroscopy: NMR spectra were collected on Bruker Avance 400 (400 MHz) and JEOL ECZ600R (600 MHz) spectrometer at 25 °C. ^{1}H and ^{13}C NMR chemical shifts (δ) are given in part per million (ppm) and calibrated to either residual solvent signal.

Mass spectrometry: High resolution ESI-MS was performed using an LTQ ORBITRAP XL Thermo spectrometer. High-resolution MALDI-TOF was performed using an AB SCIEX MALDI TOF-TOF 4800 Plus (matrix: α-cyano-4-hydroxycinnamic acid). GC-MS analyses were performed using an Agilent Technologies 6890N Network GC System.

Computational Modeling: Modeling studies were carried out by means of molecular mechanics (MM) calculations, using the Spartan 16 MMFF force field.[53]

X-Ray photoemission spectroscopy (XPS): X-ray photoelectron spectroscopy (XPS) analyses were performed in an Ultra-High-Vacuum (UHV) system using a VSW HA100 hemispherical electron energy analyzer with PSP power supply and control and a non-monochromatized Mg Kα source (photon at 1253.6 eV), with a final energy resolution of 0.86eV.[54] The binding energy (BE) scale were calibrated from the Au4f 7/2 peak at 84.0 eV of a sputtered Au surface. The core level analysis was performed by Voigt line-shape deconvolution after the background subtraction using a Shirley function. The typical precision for each component's energy position is ±0.05 eV. The uncertainty for the full width at half-maximum (FWHM) is less than ±2.5%, while it is about ±2% for the area evaluation.

ATR-IR spectroscopy: Infrared absorption spectroscopy analyses were performed with a Perkin Elmer FT-IR Spectrum Two instrument using powder samples. The background was subtracted from every spectrum recorded.

TGA analysis: TGA analysis were performed on a Perkin Elmer TGA 8000. Heating run: 25° to 900°C at 10°C/min, in air.

Scanning electron microscopy (SEM): The morphology and composition of the samples were investigated with a Zeiss Auriga Compact Field-Emission SEM. SEM images were acquired by using 1 kV acceleration voltages of the primary electron beam.

Tensile tests: Mechanical testing has been performed by using a universal testing machine Galdabini® Quasar 2.5 on rectangular specimens having the size 50x10x0.2 mm. A tensile stretch has been applied to the specimens at a constant deformation rate equal to $\dot{\lambda_x} = 5 \cdot 10^{-4}\ s^{-1}$ until the maximum deformation was reached. The specimens have been prepared for the mechanical testing by spray-painting a pattern of small irregular dots (size roughly between 0.1 and 0.5 mm) whose position is tracked, and the displacements quantified by the subsequent DIC analyses. Single or double cycle tensile mechanical tests have been conducted by recording the force and displacement with a frequency of 10 Hz, while pictures of the specimen (to be used in the digital image correlation (DIC) analyses) have been acquired by a Basler® acA5472-17uc USB 3.0 camera with a resolution of about 3000x1000 pixels at a frequency of 1 Hz.

DIC measurements: The DIC analyses have been conducted by using the Ncorr[55] software by setting the region of interest (ROI, with size equal to about 30x7 mm). The deformations along the $x-$ and the $y-$ directions have been determined through the Ncorr post processing software. The average deformations required to determine the Poisson's ratio have been obtained by considering the values of the deformations evaluated through 6 virtual extensometers placed in x direction for determining the average deformation λ_x and 12 virtual extensometers placed in y direction for determining the average deformation λ_y.

UV-Vis (UltraViolet-Visible) absorption spectra were collected using a PerkinElmer Lambda650 spectrophotometer. Absorption spectra were collected in transmission as diluted solution ($\approx 10^{-6}$), with the light beam orthogonal to the sample, using THF or chloroform as reference.

Fluorescence measurements were performed on a FLS1000 Edinburgh Fluorometer; the samples were prepared in the same way of the UV-Vis analysis. Emission spectra on solid samples were collected on thinner layers with respect to the absorption spectra, to minimize the inner-filter effects and to obtain an excitation profile comparable to the absorption spectra. Fluorescence analyses were performed placing the quartz support at 45° with respect to the excitation beam and tilted off the vertical. Furthermore, long pass filters were employed in the emission path ($l_{cut\text{-}off}$[emission] = 330 nm).

6,7-dimethoxyquinoxaline-2,3-dione (Qx1)

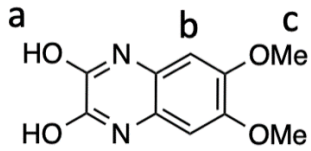

2-diamino-4,5-dimethoxy benzene (2 g, 10 mmol) was dispersed in HCl 4M (15 mL) and the suspension added to a solution of oxalic acid (1 g, 10 mmol) in HCl 4M (15 mL). The reaction mixture was heated at 100°C for 16 h. The formed precipitated was filtered and washed several times with water. The final product was obtained as dark purple solid. Yield: 1.81 g, 70%.

^{1}H NMR (400 MHz, DMSO-d_6) δ (ppm): 11.73 (s, 2H, H_a), 6.73 (s, 2H, H_b), 3.73 (s, 6H, H_c).

^{13}C NMR (101 MHz, DMSO-d_6) δ (ppm): 155.36, 140.90, 116.23, 105.36, 56.85.

GC-MS: m/z 223.40 $[M+H]^+$.

2,3-dichloro-6,7-dimethoxyquinoxaline (Qx2)

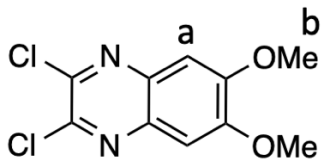

To a solution of 6,7-dimethoxyquinoxaline-2,3-dione (1 g, 4.5 mmol) in 40 mL of dry CH_2Cl_2 (40 mL), $POCl_3$ (1.71 mL, 18 mmol) and three drops of DMF were added. The reaction mixture was stirred at 85°C for 16 h. Afterwards, the solvent was removed under vacuum and the obtained solid was dissolved in CH_2Cl_2 (DCM) and filtered through celite. The final product was purified by flash column chromatography on silica gel in DCM giving a white powder. Yield: 750 mg, 75%.

^{1}H NMR (400 MHz, $CDCl_3$) δ (ppm): 7.31 (s, 2H, H_a), 4.06 (s, 6H, H_b).

^{13}C NMR (101 MHz, $CDCl_3$) δ (ppm): 153.72, 137.91, 105.70, 56.53.

GC-MS: m/z 260.1 $[M+H]^+$.

Octamethoxy-tetraquinoxaline cavitand C_V8OMe

In a microwave reactor, under dry condition, **Res[C_6H_{13},H]** (168 mg, 0.20 mmol), anhydrous potassium carbonate (280 mg, 2.0 mmol) and **Qx2** (232 mg, 0.90 mmol) were dissolved in dry DMF (9 mL). The mixture was heated at 120°C for 1.5 h (200

W). Subsequently, the solvent was removed under reduced pressure and the crude product was then purified by flash column chromatography on silica gel (DCM/EtOAc 100/0 → 95:5). The final product was obtained as pale-yellow solid. Yield: 205 mg, 64%.

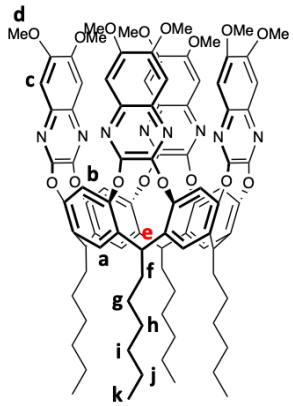

^{1}H NMR (400 MHz, $CDCl_3$) δ (ppm): 7.59 (s, 4H, H_a), 7.23 (s, 8H, H_c), 7.01 (s, 4H, H_b), 4.56 (m, 4H, H_e), 3.98 (s, 24H, H_d), 2.13 (m, 8H, H_f), 1.29 (m, 32H, $H_{g\text{-}j}$), 0.88 (t, 12H, J = 8Hz, H_k).

^{13}C NMR (101 MHz, $CDCl_3$) δ (ppm): 152.86, 152.14, 150.61, 148.52, 135.83, 133.66, 123.82, 106.21, 56.34, 36.04, 32.23, 31.81, 29.29, 27.49, 22.75, 14.15.

MALDI-TOF: calculated for $C_{92}H_{96}N_8O_{16}$ $[M + H]^+$ m/z: 1569.70, found m/z: 1569.51.

Octahydroxy-tetraquinoxaline cavitand Cv8H

Cv8OMe (110 mg, 0.07 mmol) was dissolved in dry chloroform (20 mL) and cooled in acetone/liquid nitrogen bath at -40°C. BBr_3 1M in CH_2Cl_2 (8.4 mL, 8.4 mmol) was added dropwise. The mixture was stirred for 24 h at 80°C. After cooling to room temperature, the rection was quenched with water and some drops of HCl 1M. The residual chloroform was removed under vacuum and the yellow precipitate was filtered and dried under vacuum to obtain the final product in quantitative yield.

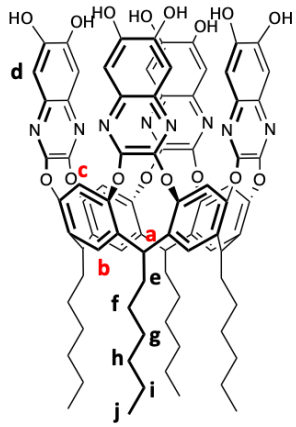

^{1}H NMR (400 MHz, acetone-d$_6$) δ (ppm): 8.14 (s, 4H, H$_c$), 7.82 (s, 4H, H$_b$), 7.27 (s, 8H, H$_d$), 5.70 (t, 4H, H$_a$), 2.42 (q, 8H, H$_e$), 1.33 (m, 32H, H$_{f\text{-}i}$), 0.94 (t, 12H, J = 8Hz, H$_j$).
^{13}C NMR (101 MHz, acetone-d$_6$) δ (ppm): 152.79, 150.14, 149.13, 136.07, 124.60, 118.52, 109.25, 34.23, 31.98, 31.85, 28.07, 22.48, 13.48.
HR-ESI-MS: calculated for $C_{92}H_{96}N_8O_{16}$ [M + H]$^+$ m/z: 1457.58151, found m/z: 1457.58523.

Octamethoxy-tetraquinoxaline cavitand kite C$_K$8OMe

Res[C$_6$H$_{13}$, CH$_3$] (100 mg, 0.11 mmol), anhydrous potassium carbonate (157 mg, 1.13 mmol) and **Qx2** (129 mg, 0.50 mmol) were added in dry DMF (4mL) and reacted at 120°C for 16 h. The reaction mixture was then precipitated in HCl 1M and the collected filtrate was purified by column chromatography on silica gel (DCM/EtOAc 9/1 → 7/3). The final product was obtained as yellow solid. Yield: 120 mg, 65%.

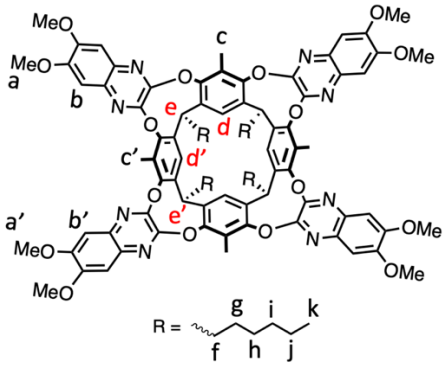

^{1}H NMR (400 MHz, CDCl$_3$) δ (ppm): 7.00 (s, 4H, H$_b$), 6.87 (s, 2H, H$_d$), 6.58 (s, 4H, H$_{b'}$), 6.15 (s, 2H, H$_{d'}$), 4.17 (s, 12H, H$_a$), 3.95 (s, 12H, H$_{a'}$), 3.68-3.64 (m, 4H, H$_{d\text{-}d'}$), 3.08 (s, 6H, H$_c$), 2.26 (s, 6H, H$_{c'}$), 1.86 (m, 8H, H$_f$), 1.13-1.10 (m, 32H, H$_{g\text{-}j}$), 0.73 (t, 12H, J = 8Hz, H$_k$).

^{13}C NMR (101 MHz, $CDCl_3$) δ (ppm): 152.70, 151.39, 150.65, 150.31, 148.17, 144.37, 134.57, 133.96, 133.23, 129.94, 128.66, 122.54, 117.57, 117.20, 106.23, 105.22, 56.38, 55.92, 37.54, 32.25, 31.50, 29.71, 29.24, 27.11, 22.51, 13.90, 12.16, 11.30, 1.03.
MALDI-TOF: calculated for $C_{96}H_{104}N_8O_{16}$ $[M + H]^+$ m/z: 1625.76, found m/z: 1625.60.

Octahydroxy-tetraquinoxaline cavitand kite Cκ8H

Under dry conditions, $AlCl_3$ (110 mg, 0.86 mmol) was added to a solution of **Cκ8OMe** (70 mg, 0.043 mmol) in dry toluene (4 mL), and the mixture reacted at 130°C for 24 h. The reaction was then quenched in HCl 1M and the precipitate was filtered and washed several times with water. The product was further purified by dissolving in methanol and precipitating in hexane. Yield: 48 mg, 74%.

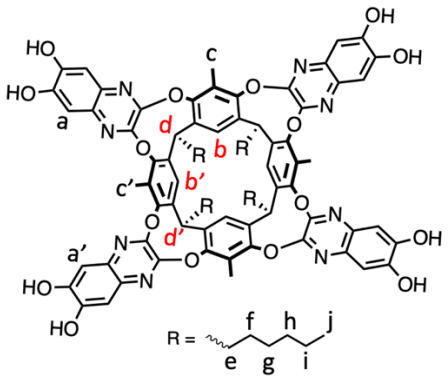

^{1}H NMR (400 MHz, CD_3OD) δ (ppm): 7.04 (s, 4H, H_a), 6.92 (s, 2H, H_b), 6.57 (s, 4H, $H_{a'}$), 6.24 (s, 2H, $H_{b'}$), 3.61-3.59 (m, 4H, $H_{d\text{-}d'}$), 3.09 (s, 6H, H_c), 2.14 (s, 6H, $H_{c'}$), 1.96-1-86 (m, 8H, H_e), 1.15-1.09 (m, 32H, $H_{f\text{-}i}$), 0.75 (t, 12H, J = 8Hz, H_i).
^{13}C NMR (101 MHz, CD_3OD) δ (ppm): 152.79, 150.48, 149.45, 148.55, 147.47, 143.86, 133.76, 133.38, 129.80, 118.20, 117.67, 108.82, 107.21, 37.25, 33.85, 31.63, 31.43, 29.35, 29.07, 28.63, 28.54, 28.13, 26.74, 22.34, 22.17, 18.51, 13.05, 12.95, 12.25, 11.47.
HR-ESI-MS: calculated for $C_{88}H_{88}N_8O_{16}$ $[M + H]^+$ m/z: 1513.63911, found m/z: 1513.64845, calculated for $[2M + 2H]^{2+}$ m/z: 1513.63911, found m/z: 1513.64845.

Synthesis of the crosslinked polymer PIM1-CV8H

TTSBI (470 mg, 1.38 mmol, 0.92 eq) and **Cv8H** (88 mg, 60 μmol, 0.04 eq) were dissolved in dry DMF (45 mL). Anhydrous potassium carbonate (932 mg, 6.75 mmol) was added to the solution and the mixture was kept stirring at room temperature for 15 minutes, followed by the addition of **TFTPN** (300 g, 1.5 mmol, 1 eq). The reaction was stirred at 60 °C for 3 days, observing the formation of a yellow

precipitate. The mixture was quenched in water (300 mL), allowing the precipitation of the polymer that was filtered and washed several times with water and methanol. The product was further purified by refluxing in water (300 mL) for 4 hours, and 0.722 g of the product were recovered as yellow powder after filtration and drying in a vacuum oven at 60 °C for 2 days.
The procedure described above was adopted for the synthesis of **PIM1-Cκ8H** (**Scheme 2.4**), replacing **Cv8H** with **Cκ8H,** using the same equivalents of the components.

Crystal structure geometric parameters

The crystal structure of the *vase* cavitand **Cv8OMe** was determined by X-ray diffraction on single crystals grown from slow evaporation from a DMSO solution. Crystal data and experimental details for data collection and structure refinement are reported in **Table 5**. Intensity data and cell parameters were recorded at 100(2) K on a Bruker D8 Venture PhotonII diffractometer (CuK radiation = 1.54178 Å). The raw frame data were processed using SAINT and SADABS to yield the reflection data files.[56] The structures were solved by Direct Methods using the SHELXT program[57] and refined on F_o^2 by full-matrix least-squares procedures, using SHELXL-2018[58] in the WinGX suite v.2014.1.[59] All non-hydrogen atoms were refined with anisotropic atomic displacements, with the exception of some atoms of the disordered alkyl chains or DMSO molecules. The hydrogen atoms were included in the refinement at idealized geometry and refined "riding" on the corresponding parent atoms.
Crystals were obtained also for the kyte cavitand **Cκ8OMe**. Intensity data and cell parameters were recorded at 150(2) K on a Bruker D8 Venture PhotonII diffractometer (CuKα radiation α = 1.54178 Å). In this case however the crystals diffracted poorly, and the final data were not good enough for a complete structural refinement. It was nonetheless possible to determine the bond connectivity of **Cκ8OMe** and to infer some information on the geometry of the compound.
Main crystallography data for cavitand Cκ8OMe: Monoclinic, $P2_1/c$, a = 36.212(2) Å, b = 34.656(2) Å, c = 34.771(2) Å, β = 114.803(3)°, V = 39611.8 $Å^3$, Z = 4. Theta range for data collection: 1.852 to 60.239°. Reflections collected / unique: 848479 / 57733 [R(int) = 0.3624].

Table 2.5. Crystallographic data for **C$_v$8OMe**.

	C$_v$8OMe
Formula	$C_{92}H_{96}N_8O_{16}\cdot 4C_2H_6SO$
Formula weight	1882.27
Crystal system	Triclinic
Space group	*P*-1
a/Å	17.841(4)
b/Å	22.924(5)
c/Å	24.363(5)
□/°	78.29(3)
β/°	89.60(3)
□/°	85.72(3)
V/Å^3	9729(4)
Z	4
D_c/g cm^{-3}	1.285
F(000)	4000
μ/mm^{-1}	1.497
$\theta_{min,max}$/°	1.85, 59.47
Reflections collected	28105
R [Fo>4□(Fo)][a], w*R*2[a]	0.0695, 0.1727

[a] $R1 = \Sigma \| F_o \| - | F_c \| / \Sigma | F_o |$, $wR2 = [\Sigma[w(F_o^2 F_c^2)^2]/\Sigma[w(F_o^2)^2]]^{1/2}$

Preparation of the auxetic blends

PIM1 was synthetized according to the reported procedure in literature.[1]

PIM1, **PIM1-Cv8H** and **PIM1-Cκ8H** were used for the preparation of the blend (**B0.1-Cv8H**, **B0.4-Cv8H, B0.8-Cv8H, B1.2-Cv8H**, **B1.2-Cκ8H**) in different weight (**Table 2.6)**. Each blend weights 1.3 g and was obtained in a Petri dish of 9 cm ∅.

Table 2.6. Quantity of **PIM1**, **PIM1-Cv8H** and **PIM1-Cκ8H** used for each blend.

	PIM1 (g)	Crosslinked polymer (g)
B0.1-Cv8H	1.287	0.013
B0.4-Cv8H	1.235	0.065
B0.8-Cv8H	1.170	0.130
B1.2-Cv8H	1.105	0.195
B1.2-Cκ8H	1.170	0.130

General procedure for auxetic blend preparation
PIM1 was dissolved in chloroform and stirred overnight at room temperature. In a separated flask, a dispersion of **PIM1-Cv8H** (or **PIM1-Cκ8H** for **B1.2-Cκ8H** preparation), in chloroform was prepared and stirred overnight at room temperature. The two samples were mixed, vigorously stirred for 3 hours and then sonicated using an ultrasonic homogenizer (Hielscher UP200Ht, 200 W, 26 KHz) for 20 minutes. The dispersion was casted in a Petri dish (9 cm ∅), kept in a closed environment under a gently flow of nitrogen to allow the slow evaporation of the solvent over 48-72 hours. The dried film was then removed by detaching it carefully. The films obtained are reported in **Figure 2.13**.

Control film preparations

PIM1 (1.287 g) was dissolved in chloroform (30 mL), then **Cv** (13 mg) was added. The solution was stirred overnight at room temperature and casted in a Petri dish (9 cm ∅), and the solvent was allowed to evaporate in a closed compartment under a gentle nitrogen flow over 3 days. The same procedure and quantity were followed for the preparation of control film with **Cκ**. The obtained final films are shown in **Figure 2.19**.
Cv and **Cκ** and their corresponsive resorcinarenes scaffold were prepared according to procedures reported in literature.

Appendix Chapter 2

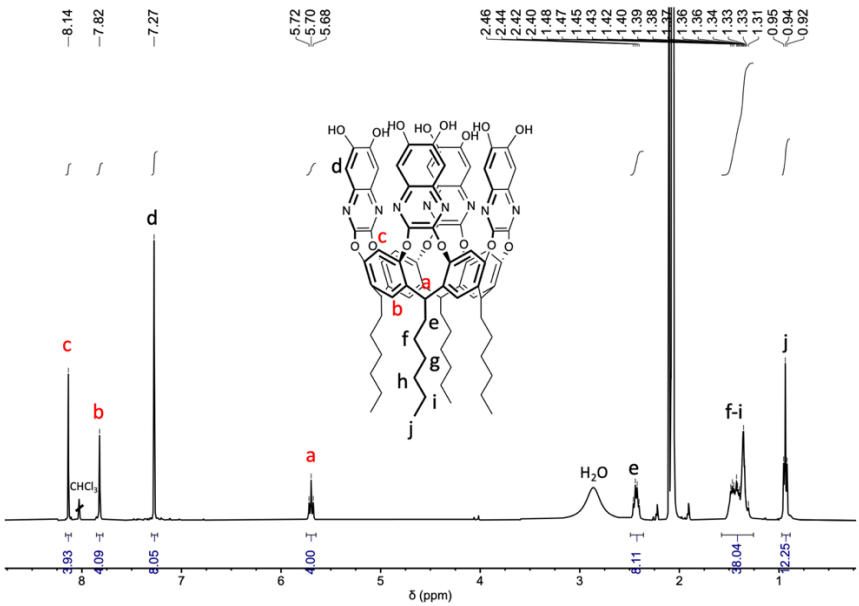

Figure* 2.*A1. *^{1}H NMR spectrum of **Cv8H** (acetone-d$_6$, 400 MHz, 25°C).*

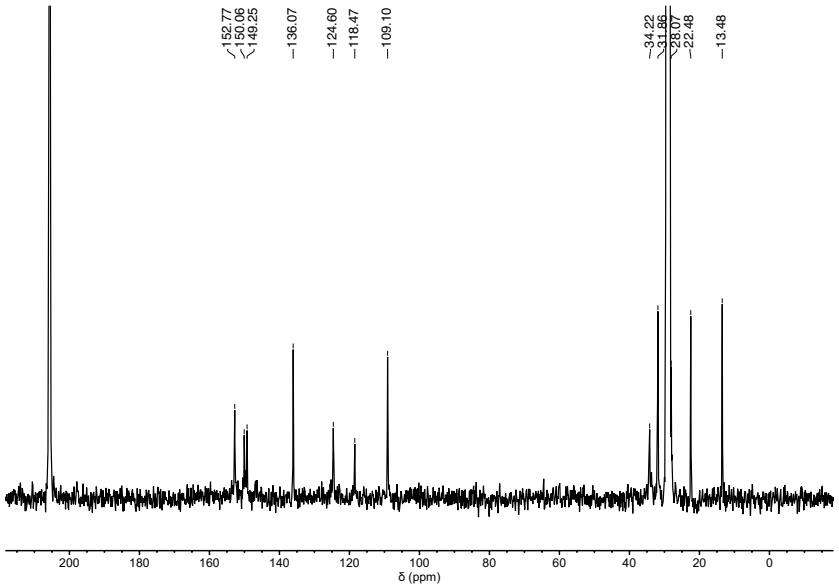

Figure* 2.*A2. *^{13}C NMR spectrum of **Cv8H** (acetone-d$_6$, 101 MHz, 25°C).*

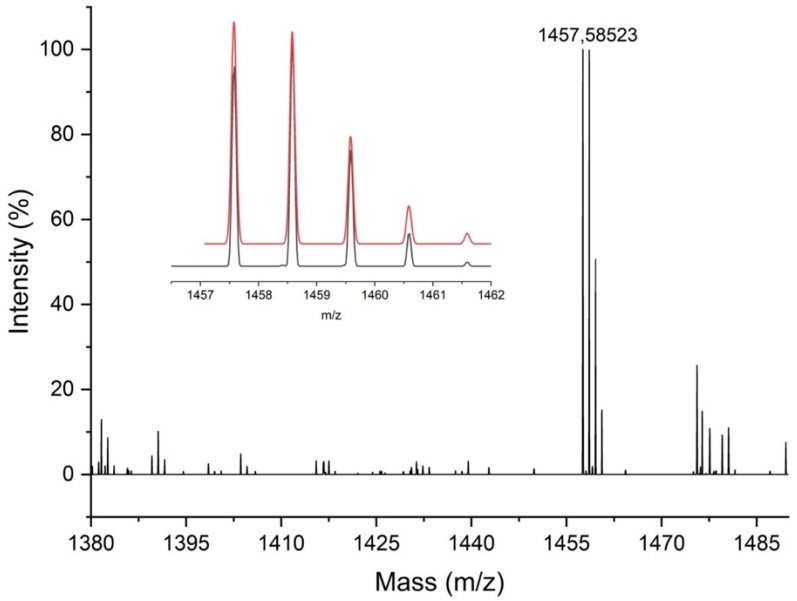

Figure 2.A3. *HR-ESI-MS spectrum of* ***Cv8H*** *with experimental (black line) versus theoretical (red line) isotopic distribution in the inset.*

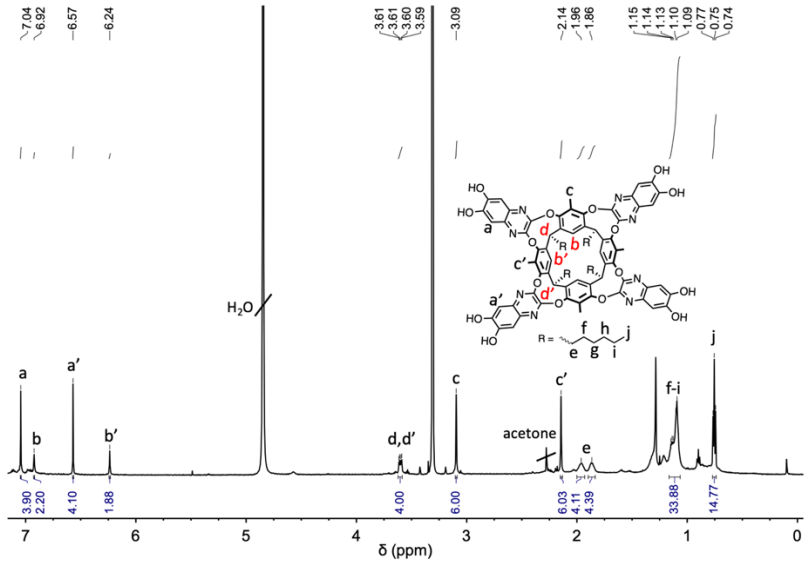

Figure 2.A4. *^{1}H NMR spectrum of* ***Cк8H*** *(CD_3OD, 400 MHz, 25°C).*

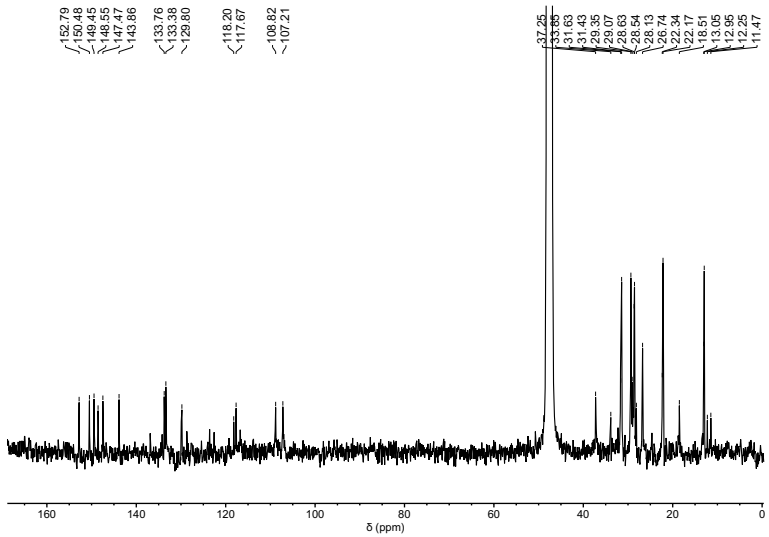

Figure* 2.*A5. *^{13}C NMR spectrum of **Cк8H** (CD_3OD, 101 MHz, 25°C).*

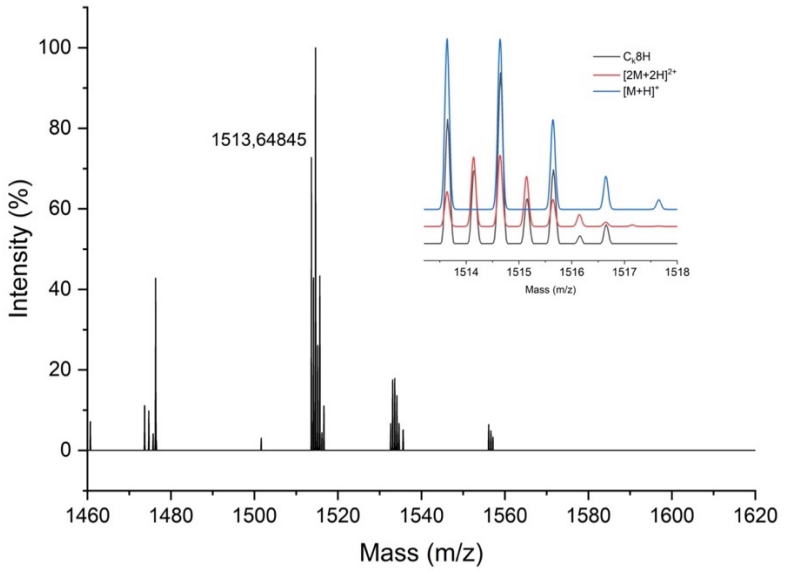

Figure* 2.*A6. *HR-ESI-MS spectrum of **Cк8H** with experimental (black line) versus theoretical (red and blue line) isotopic distributions in the inset.*

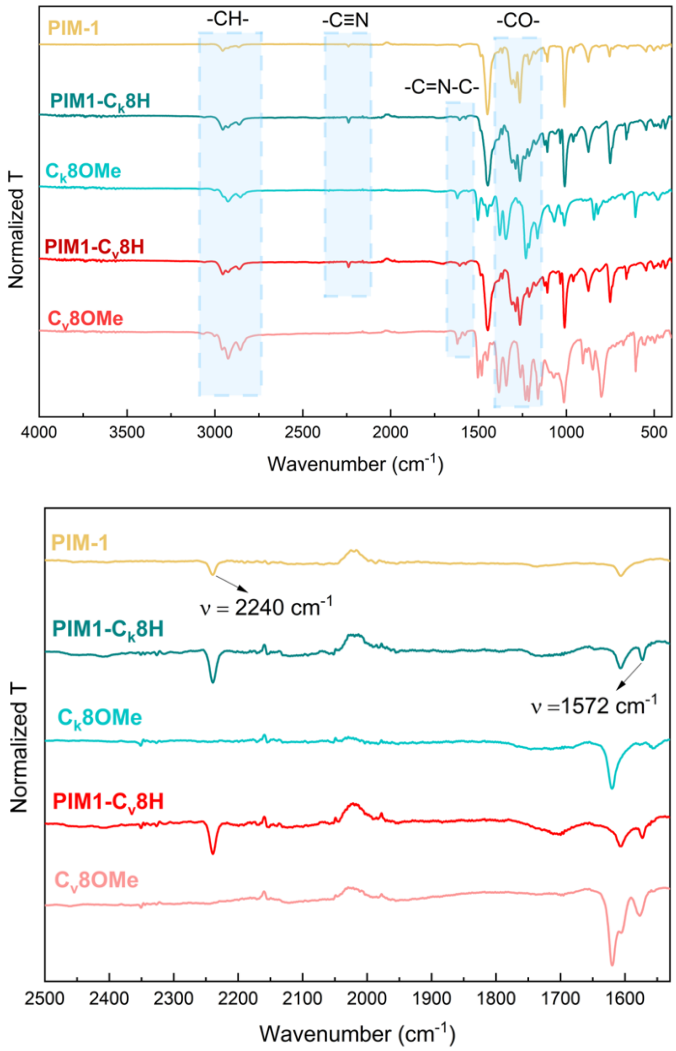

Figure 2.A7. FT-IR full spectra (top) and zoom from 2500 to 1500 cm^{-1} (bottom) of **PIM1-Cv8H** and **PIM1-Cκ8H** in comparison to the spectra of **Cv8OMe**, **Cκ8OMe** and **PIM1**.

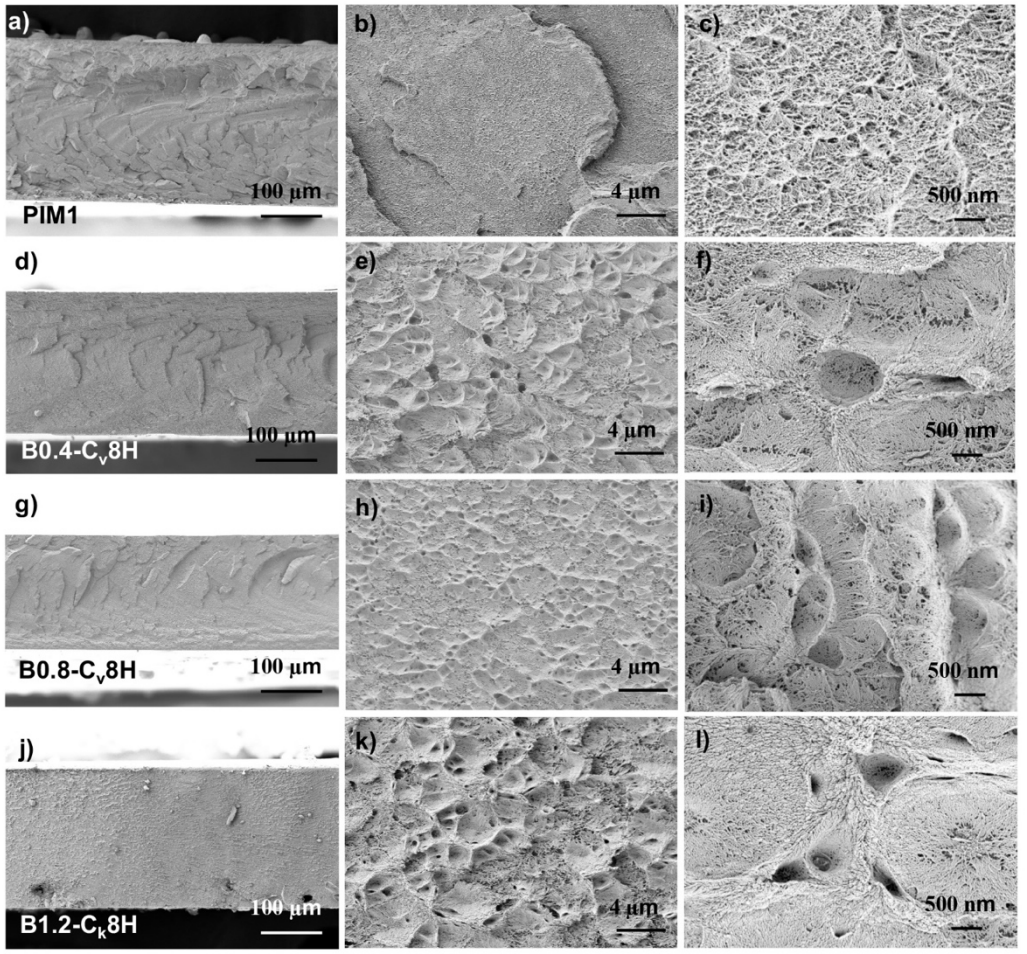

Figure 2.A8. SEM cross section images and magnification images of **PIM1** (a, b, c), **B0.4-Cv8H** (d, e, f), **B0.8-Cv8H** (g, h, i), **B1.2-Cκ8H** (j, k, l).
B0.1-Cv8H was not analyzed at SEM since it has not shown NPR, while **B1.2-Cv8H** exhibits an anomalous NPR trend, see **Figure 2.16d**.

References

[1] P. M. Budd, B. S. Ghanem, S. Makhseed, N. B. McKeown, K. J. Msayib, C. E. Tattershall, *Chem. Commun.* **2004**, 230.

[2] P. M. Budd, E. S. Elabas, B. S. Ghanem, S. Makhseed, N. B. McKeown, K. J. Msayib, C. E. Tattershall, D. Wang, *Adv. Mater.* **2004**, *16*, 456.

[3] L. Gao, M. Alberto, P. Gorgojo, G. Szekely, P. M. Budd, *J. Membr. Sci.* **2017**, *529*, 207.

[4] F. J. Vernerey, R. Long, R. Brighenti, *J. Mech. Phys. Solids* **2017**, *107*, 1.

[5] C. Li, A. L. Ward, S. E. Doris, T. A. Pascal, D. Prendergast, B. A. Helms, *Nano Lett.* **2015**, *15*, 5724.

[6] R. Tan, A. Wang, R. Malpass-Evans, R. Williams, E. W. Zhao, T. Liu, C. Ye, X. Zhou, B. P. Darwich, Z. Fan, L. Turcani, E. Jackson, L. Chen, S. Y. Chong, T. Li, K. E. Jelfs, A. I. Cooper, N. P. Brandon, C. P. Grey, N. B. McKeown, Q. Song, *Nat. Mater.* **2020**, *19*, 195.

[7] D. C. Sherrington, A. P. Kybett, N. B. McKeown, H. Li, S. Makhseed, in *Supported Catalysts and Their Applications* (Eds.: D. C. Sherrington, A. P. Kybett), The Royal Society Of Chemistry, **2001**, pp. 214–218.

[8] H. J. Mackintosh, P. M. Budd, N. B. McKeown, *J. Mater. Chem.* **2008**, *18*, 573.

[9] B. S. Ghanem, N. B. McKeown, P. M. Budd, J. D. Selbie, D. Fritsch, *Adv. Mater.* **2008**, *20*, 2766.

[10] B. S. Ghanem, N. B. McKeown, P. M. Budd, N. M. Al-Harbi, D. Fritsch, K. Heinrich, L. Starannikova, A. Tokarev, Y. Yampolskii, *Macromolecules* **2009**, *42*, 7881.

[11] M. Carta, K. J. Msayib, P. M. Budd, N. B. McKeown, *Org. Lett.* **2008**, *10*, 2641.

[12] B. S. Ghanem, N. B. McKeown, P. M. Budd, D. Fritsch, *Macromolecules* **2008**, *41*, 1640.

[13] S. Makhseed, J. Samuel, A. Bumajdad, M. Hassan, *J. Appl. Polym. Sci.* **2008**, *109*, 2591.

[14] M. Carta, P. Bernardo, G. Clarizia, J. C. Jansen, N. B. McKeown, *Macromolecules* **2014**, *47*, 8320.

[15] B. S. Ghanem, N. B. McKeown, P. M. Budd, N. M. Al-Harbi, D. Fritsch, K. Heinrich, L. Starannikova, A. Tokarev, Y. Yampolskii, *Macromolecules* **2009**, *42*, 7881.

[16] Y. Rogan, L. Starannikova, V. Ryzhikh, Y. Yampolskii, P. Bernardo, F. Bazzarelli, J. C. Jansen, N. B. McKeown, *Polym. Chem.* **2013**, *4*, 3813.

[17] Y. Rogan, R. Malpass-Evans, M. Carta, M. Lee, J. C. Jansen, P. Bernardo, G. Clarizia, E. Tocci, K. Friess, M. Lanč, N. B. McKeown, *J. Mater. Chem. A* **2014**, *2*, 4874.

[18] M. Carta, R. Malpass-Evans, M. Croad, Y. Rogan, J. C. Jansen, P. Bernardo, F. Bazzarelli, N. B. McKeown, *Science* **2013**, *339*, 303.

[19] M. Carta, M. Croad, J. C. Jansen, P. Bernardo, G. Clarizia, N. B. McKeown, *Polym. Chem.* **2014**, *5*, 5255.

[20] N. B. McKeown, *Polymer* **2020**, *202*, 122736.
[21] N. Du, J. Song, G. P. Robertson, I. Pinnau, M. D. Guiver, *Macromol. Rapid Commun.* **2008**, *29*, 783.
[22] Y. Wang, N. B. McKeown, K. J. Msayib, G. A. Turnbull, I. D. W. Samuel, *Sensors* **2011**, *11*, 2478.
[23] J. C. Thomas, J. E. Trend, N. A. Rakow, M. S. Wendland, R. J. Poirier, D. M. Paolucci, *Sensors* **2011**, *11*, 3267.
[24] A. Fuoco, M. Khdhayyer, M. Attfield, E. Esposito, J. Jansen, P. Budd, *Membranes* **2017**, *7*, 7.
[25] L. P. Skala, A. Yang, M. J. Klemes, L. Xiao, W. R. Dichtel, *J. Am. Chem. Soc.* **2019**, *141*, 13315.
[26] E. Dalcanale, P. Soncini, G. Bacchilega, F. Ugozzoli, *J. Chem. Soc., Chem. Commun.* **1989**, 500.
[27] L. Pirondini, A. G. Stendardo, S. Geremia, M. Campagnolo, P. Samorì, J. P. Rabe, R. Fokkens, E. Dalcanale, *Angew. Chem. Int. Ed.* **2003**, *42*, 1384.
[28] S. Nemat-Nasser, M. Hori, J. D. Achenbach, *Micromechanics: Overall Properties of Heterogeneous Materials, Elsevier Science, Amsterdam* **2014**.
[29] W. Kuhn, F. Grün, *Kolloid-Zeitschrift* **1942**, *101*, 248.
[30] E. Helfand, *The Journal of Chemical Physics* **1975**, *62*, 999.
[31] E. M. Arruda, M. C. Boyce, *J. Mech. Phys. Solids* **1993**, *41*, 389.
[32] P. Hänggi, P. Talkner, M. Borkovec, *Rev. Mod. Phys.* **1990**, *62*, 251.
[33] H. A. Kramers, *Physica* **1940**, *7*, 284.
[34] R. Brighenti, F. Artoni, F. Vernerey, M. Torelli, A. Pedrini, I. Domenichelli, E. Dalcanale, *J J. Mech. Phys. Solids* **2018**, *113*, 65.
[35] M. F. Beatty, D. O. Stalnaker, *J. Appl. Mech.* **1986**, *53*, 807.
[36] T. Fíla, P. Koudelka, P. Zlámal, J. Falta, M. Adorna, M. Neuhäuserová, J. Luksch, O. Jiroušek, *Adv. Eng. Mater.* **2019**, *21*, 1900204.
[37] L. Francesconi, M. Taylor, K. Bertoldi, A. Baldi, *Exp Mech* **2018**, *58*, 283.
[38] J. R. Moran, J. L. Ericson, E. Dalcanale, J. A. Bryant, C. B. Knobler, D. J. Cram, *J. Am. Chem. Soc.* **1991**, *113*, 5707.
[39] D. J. Cram, H. J. Choi, J. A. Bryant, C. B. Knobler, *J. Am. Chem. Soc.* **1992**, *114*, 7748.
[40] P. M. Budd, E. S. Elabas, B. S. Ghanem, S. Makhseed, N. B. McKeown, K. J. Msayib, C. E. Tattershall, D. Wang, *Adv. Mater.* **2004**, *16*, 456.
[41] G. Beamson, D. Briggs, *High Resolution XPS of Organic Polymers: The Scienta ESCA300 Database*, Wiley, Chichester [England]; New York, **1992**.
[42] D. Sindhuja, M. Gopiraman, P. Vasanthakumar, N. Bhuvanesh, R. Karvembu, *J. Organomet. Chem.* **2021**, *949*, 121933.
[43] C. Christodoulou, A. Giannakopoulos, M. V. Nardi, G. Ligorio, M. Oehzelt, L. Chen, L. Pasquali, M. Timpel, A. Giglia, S. Nannarone, P. Norman, M. Linares, K. Parvez,

K. Müllen, D. Beljonne, N. Koch, *J. Phys. Chem. C* **2014**, *118*, 4784.

[44] M. Giannetto, A. Pedrini, S. Fortunati, D. Brando, S. Milano, C. Massera, R. Tatti, R. Verucchi, M. Careri, E. Dalcanale, R. Pinalli, *Sens. and Actuators B: Chem.* **2018**, *276*, 340.

[45] M. Tamaddondar, A. B. Foster, M. Carta, P. Gorgojo, N. B. McKeown, P. M. Budd, *ACS Appl. Mater. Interfaces* **2020**, *12*, 46756.

[46] J. M. Powers, R. M. Caddell, *Polymer Engineering & Sci* **1972**, *12*, 432.

[47] G. M. Neville, R. Jagpal, J. Paul-Taylor, M. Tian, A. D. Burrows, C. R. Bowen, T. J. Mays, *Mater. Adv.* **2022**, *3*, 8934.

[48] M. Torelli, F. Terenziani, A. Pedrini, F. Guagnini, I. Domenichelli, C. Massera, E. Dalcanale, *ChemistryOpen* **2020**, *9*, 261.

[49] J. N. Grima, K. E. Evans, *Chem. Commun.* **2000**, 1531.

[50] J. N. Grima, J. J. Williams, K. E. Evans, *Chem. Commun.* **2005**, 4065.

[51] N. Pour, L. Itzhaki, B. Hoz, E. Altus, H. Basch, S. Hoz, *Angew. Chem. Int. Ed.* **2006**, *45*, 5981.

[52] D. B. G. Williams, M. Lawton, *J. Org. Chem.* **2010**, *75*, 8351.

[53] W. J. Hehre, W. W. Huang, *Chemistry with Computation: An Introduction to SPARTAN*, Wavefunction, Irvine, **1995**.

[54] R. Tatti, L. Aversa, R. Verucchi, E. Cavaliere, G. Garberoglio, N. M. Pugno, G. Speranza, S. Taioli, *RSC Adv.* **2016**, *6*, 37982.

[55] Ncorr v1.2, open source 2D digital image correlation MATLAB program, http://www.ncorr.com/ (last access on 20th Oct. 2022).

[56] (a) SADABS Bruker AXS; Madison, Wisconsin, USA, 2004; SAINT, Software Users Guide, Version 6.0; Bruker Analytical X-ray Systems, Madison, WI, **1999**; (b) Sheldrick, G. M. SADABS v2.03: Area-Detector Absorption Correction. University of Göttingen, Germany, **1999**.

[57] G. M. Sheldrick, *Acta Crystallogr. A Found Adv.* **2015**, *71*, 3.

[58] G. M. Sheldrick, *Acta Crystallogr. A Found Crystallogr.* **2008**, *64*, 112.

[59] L. J. Farrugia, *J. Appl. Crystallogr.* **1999**, *32*, 837.

[60] L. M. Tunstad, J. A. Tucker, E. Dalcanale, J. Weiser, J. A. Bryant, J. C. Sherman, R. C. Helgeson, C. B. Knobler, D. J. Cram, *J. Org. Chem.* **1989**, *54*, 1305.

Chapter 3

Cavitand crosslinked liquid crystal elastomers as potential auxetic materials

3.1. Introduction

3.1.1. Liquid crystals (LCs)

Liquid crystal phases, categorizes as mesophases (from the Greek word "meso" meaning "in the middle"), were first discovered by Lehmann and Reinitzer in 1888, and named as a "fourth state of matter"[1] since they blend properties of both liquids and solids, demonstrating a notable degree of anisotropy while maintaining fluidity. Liquid crystals consist of molecules known as mesogens, which self-assemble in different mesophases, according to their relative positional order.[2] Examples of LC phases (**Figure 3.1**) are: the nematic phase (N), the least ordered and most fluid of the liquid crystal phases, in which molecules possess only long-range orientational order but not positional order, in other words the molecules are aligned parallel to one another, all pointing roughly in the same direction; smectic-A (SA) or smectic-C (SC) which present both orientational and one long range positional order, in which the molecules are arranged in parallel or tilted in planes. Other less common phases are the cholesteric or chiral nematic in which the chirality of the LC molecules induce a distinct rotation of mesogens resulting in a characteristic pitch.[3] Within a nematic phase, liquid crystal units exhibit an average orientation parallel to each other in a preferred direction, known as the director, denoted by the symbol "n". This preferred orientation is crucial in understanding and manipulating the properties of liquid

crystals, as changes in the director orientation can lead to variations in the optical, electrical, or mechanical characteristics of the material. Control over the director is fundamental in the design and operation of liquid crystal devices, such as liquid crystal displays (LCDs).[4,5] The critical temperature T_{NI} denotes the temperature at which a liquid crystal undergoes a phase transition from the nematic phase to the isotropic phase. This transition temperature is crucial in understanding the thermal behavior of liquid crystals, as it represents the temperature at which the long-range orientational order in the nematic phase is lost, and the material becomes isotropic. The T_{NI} can vary among different types of liquid crystals and is influenced by factors such as the molecular structure and the presence of additives.[6]

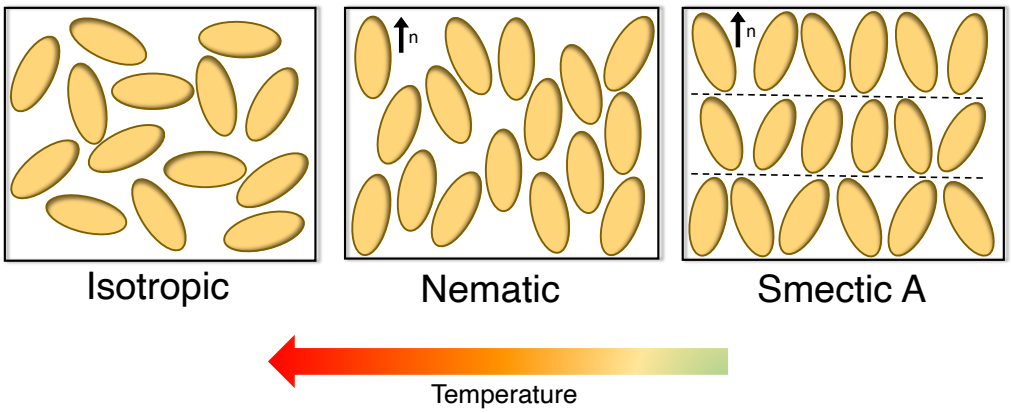

Figure 3.1. *Representation of different liquid crystals phases moving from the highly oriented Smectic A (right) to nematic (middle) and lastly to the isotropic state (left). By increasing the temperature, the isotropic state is favored.*

3.1.2. Liquid crystal elastomers (LCEs)

When mesogens are covalently linked within a polymer network, they are known as liquid crystal elastomers (LCEs), a class of materials which combine the orientational order and anisotropic properties of LCs with the rubber-like elasticity of conventional elastomers. Mesogenic units, weakly crosslinked within these networks, causes a preferential orientation in the average polymer conformation.[2] It is important to define how the mesogenic units are incorporated into the polymer backbone: if they

are within polymer chain, connected along their long axis, they are referred as main chain LCE. If, instead they are attached as lateral substituents, they are defined side chain LCE. Within this last classification, there are two subcategories: side-on side chain, when mesogens are connected horizontally to the polymer and end-on side chain when they are terminally attached to the backbone. Schematization of the different LCEs arrangement is shown in **Figure 3.2**.

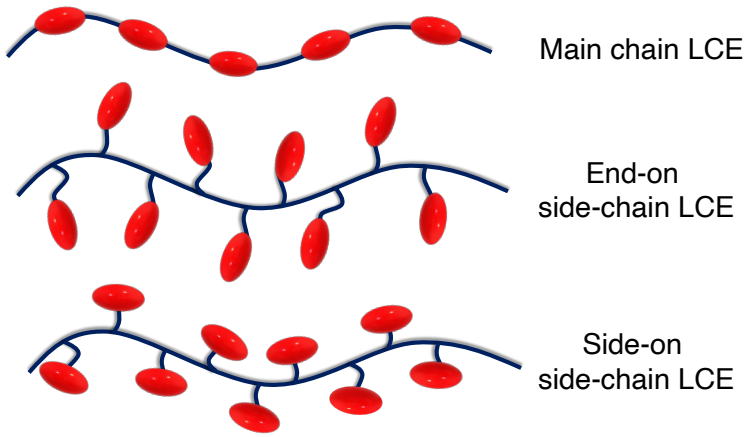

Figure 3.2. *Scheme of mesogens arrangement in liquid crystal elastomers.*

Unlike the typical spherical random-coil polymer conformation, a nematic LCE assumes an elongated conformation when crosslinked in an oriented state, facilitated by the energetically favorable rod-rod interaction among mesogens. Heating above T_{NI} lead to the prevail of isotropic random-coil conformation (**Figure 3.3a**) since the interactions present in the nematic phase are eliminated, resulting in macroscopic shape-change with relatively larger actuation strains. In the presence of crosslinking the shape memory effect is permanent.[7]

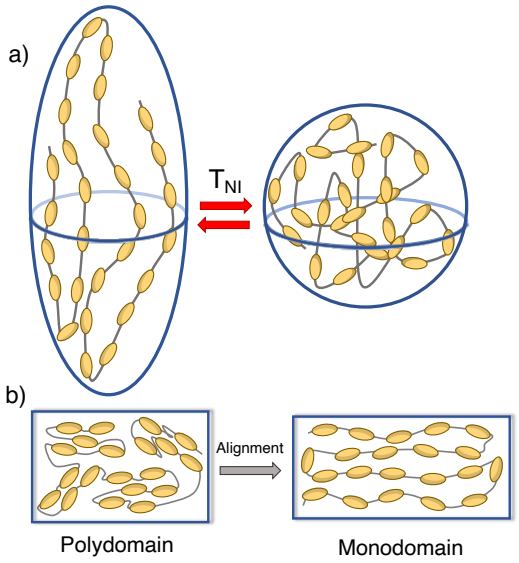

Figure 3.3. *a) Aligned main chain LCE main chain sample below T_{NI} and spherical polymer configuration above T_{NI}. b) Scheme of polydomain LCE, where mesogens possess local orientation, and monodomain obtained after alignment, where all LCs are oriented in the direction of the stress applied.*

Main chain LCE undergo more pronounced changes in shape compared to side chain LCE. This arises because mesogens, organized anisotropically, are strongly coupled to the polymeric backbone. However, shape change can still occur when pendant mesogenic unit display sufficient interaction coupling. The degree to which an elastomer sample will change shape on its nematic to isotropic transition is also dependent on the alignment of the sample. It is then significant to define polydomain and monodomain states. In a monodomain LCE, a single and uniform orientation of liquid crystal molecules prevails throughout the material. This results in a macroscopically anisotropic structure with consistent molecular alignment. The advantages of monodomain LCEs lie in their predictable and well-defined actuation response. Conversely, polydomain LCEs exhibit a more complex internal structure featuring multiple regions or domains with liquid crystal orientated in different direction (**Figure 3.3b**). The presence of these distinct domains introduces a level of intricacy to the actuation response. Polydomain LCEs may display a more versatile

deformation behavior due to different direction of actuation but predicting and controlling their response becomes a more challenging endeavor. In paragraph 3.1.4 the different approaches to obtain aligned LCE samples will be described.

3.1.3. Synthesis and preparation of LCEs

Numerous strategies have been used for the preparation of LCEs. Depending on the classes of LCE the fabrication methods are different.

Generally, the synthesis of LCEs requires two key processes: first, the synthesis of the liquid crystal monomer or its implementation into a polymeric backbone and secondly a crosslinking reaction to obtain a network. In **Figure 3.4** are schematize common chemistry reactions for the polymerization of mesogens. The synthesis of side chain LCE is classified into two main categories: radical polymerization and hydrosilylation reaction.[8] Free radical polymerization (**Figure 3.4a**) involves the use of a photo- or thermal initiator to trigger the formation of a radical which attacks a double bond C=C functionality. A variety of monomers can be synthetized with this method, even though the most common used are acrylates and methacrylates-based monomers. [9,10]

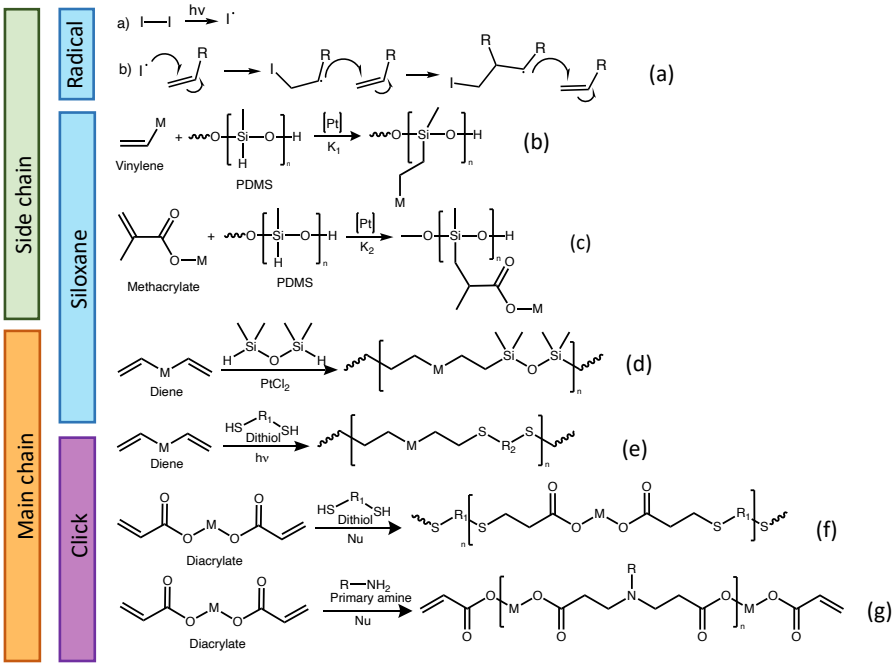

Figure 3.4. *Various reaction used to synthesize LCEs. a) free radical polymerization; b,c) Side chain hydrosilylation, d) Main chain hydrosilylation, e) Photo-initiated thiol-ene Michael addition click reaction, f) Thiol-acrylate Michael addition click reaction, g) Aza-Michael addition click reaction, shown here with excess acrylate.*

Hydrosilylation is the second method used to obtain side chain LCE, which involves the formation of a Si-C bond through a Si-H siloxane reaction with an unsaturated unit C=C (**Figure 3.4a**, **b**, **c**).[11] The resulting elastomers possess more chain anisotropy compared to those synthetized *via* radical polymerization, resulting in higher actuation and lower glass transition temperatures.[2] Both features are ascribable to the formation of the Si-O bonds in the polymeric backbone, which help to promote chain mobility and flexibility. Despite of this remarkable advantage, there are several drawbacks. The most relevant one arises from the necessity to use dry and deoxygenated environment to preserve the catalyst used for the polymerization, most commonly a Pt(0) complex.

Historically, the chemistry of main-chain LCEs has been limited to polycondensation or polyaddition reaction whose require high purity starting materials.[9] The first main chain LCE was synthetized using an hydrosilylation reaction in 1997.[12] It is

important to notice that the preparation of main chain LCEs lead to highly ordered mesophases, therefore a proper design of the molecule it is necessary to target the nematic phase.

Recently click reaction has been employed for its quantitative yield, the absence of strict conditions and limited side reaction obtained.[13] Examples are radical-initiated thiol-ene, between a thiol and a double bond initiated with a photo- or thermal initiator (**Figure 3.4d**) or Michael addition reaction with the use only of a catalyst (**Figure 3.4e**, **f**).[14,15] The reaction can be performed using both thiol-acrylate and amine-acrylate functional groups leading to C-S or C-N bond formed between monomers. This last approach has gained interest for the possibility to prepare bulk samples[16] and the advantage to have a library of commercially available monomers. Another promising strategy for the incorporation of mesogens is the preparation of the network using covalent adaptable networks (CANs) thanks to the peculiar characteristic to possess reversible and dynamic bonds.[17] By using this strategy manipulation of the mesogens can be performed post-polymerization with thermal and photo-chemical stimuli.[18] In literature, different works have demonstrated that CAN-LCEs enable both local and global monodomain programming. They also exhibit self-healing property as well as the ability to reset programming of monodomain.[19–21] One example of CANs applied to LCEs is a reversible addition fragmentation chain-transfer (RAFT) polymerization which involve the reaction between an allyl disulfide with a radical photo-initatior. In 2017, Bowman research group have incorporated RAFT reaction into LCE chemistry enabling control over alignment, domain structure and birefringence through photochemical stimulation.[21]

Another approach using reversible bonds is transterification, common reaction between a hydroxyl group and an ester group. Different researcher have demonstrated the possibility of surface welding and recyclability of transesterification-based LCEs.[22,23] Hanzon and co-workers welded together two transterification-based LCEs to create one single materials. The fused samples evidenced the ability to be strained more than 220% before the bond between two

LCEs broke. This results in a molecular bonding strength rather than solely adhesion on the surface. [22]

Exchangeable disulfide bond is another type of reversible bond that allow reprogramming and recycling of LCEs. The disulfide bond fragments and reforms upon UV irradiation within the network. Cai research group was the first one to incorporate this type of bonds in the elastomeric backbone of LCEs.[19] They demonstrated the possibility to program monodomains using two way actuation in LCEs. For the photochemical stimulus, strained samples were exposed to UV light for a certain amount of time. For the thermal stimulus, samples were heated at 180 °C and then strained. For both stimuli the pathway of actuation was identical, thus suggesting that both light and heat, used to trigger the disulfide bond, are effective in inducing a monodomain within the materials.

3.1.4. LCE alignment

Liquid crystal elastomers (LCEs) have emerged as a class of smart materials with versatile actuation capabilities, gaining considerable attention in academic community. The actuation of LCEs is primarily driven by the reorientation of liquid crystal domains within the elastomeric matrix, leading to macroscopic shape changes. This phenomenon has paved the way for the development of advanced soft actuators[24,25] and artificial muscles[26] that mimic natural motion. Researchers are exploring various mechanisms, to precisely control and manipulate the actuation behavior of LCEs.

The alignment is permanent in crosslinked LCEs. However, LCE actuation is only feasible if LCEs are crosslinked in an aligned state. Different methods were developed to program LCEs architectures.

The first one, named Finkelmann method or also known as mechanical alignment, was developed by Finkelmann in 1991.[27] Its consists in applying a stress to the LCEs in a temperature range within the mesophase, thus mesogens rearrange in a preferential orientation, in this case the one of the force applied.

Command surfaces, similar to those used in liquid crystal displays (LCDs)[28], have played a crucial role in programming 2D liquid crystal elastomer (LCE) films. Typically, they consist of rubbed polymer surfaces, such as polyimide or polyvinyl alcohol, rubbed with materials like velvet or felt.[29,30] The interaction of microgrooves and polymer within these surfaces sandwiches aligns mesogens thanks to their collective behavior. However, this method is limited to thin films due to surface-mesogen interactions.[31]

Magnetic fields have also been used to program director alignment by taking advantage of the anisotropic magnetic susceptibility of rigid mesogens.[13,30] This method is especially appropriate for side-on or end-on side chain LCEs. Microfabricated architectures, such as microplate arrays, honeycomb structures, and artificial irises, have been programmed with uniform or non-uniform fields to create complex shape-morphing LCEs.[32,33] Currently, magnetically aligned actuators are limited to micro-architected materials.

More recently, Lewis and co-workers synthesized LCE-based inks for 3D printing with light-triggerable dynamic bonds. During the printing process the director can be locally programmed and UV light is used to control network reconfiguration.[34]

In this chapter, a liquid crystal elastomer is implemented as matrix for the development of molecular auxetic polymer. In particular, to achieve NPR values, tetraquinoxaline cavitands are introduced as crosslinkers in highly aligned main chain LCE. In this design, being the polymer chains already oriented the applied mechanical stress is not dissipated in the disentanglement and conformational reorganization of the polymer chains but directly influences the opening of the cavitand, inducing a vase-to-kite switch and resulting in a subsequent volume increase (**Figure 3.5**). In other words, the material response to the conformational variation of the cavitand should be maximized thanks to the preorganization of the matrix.

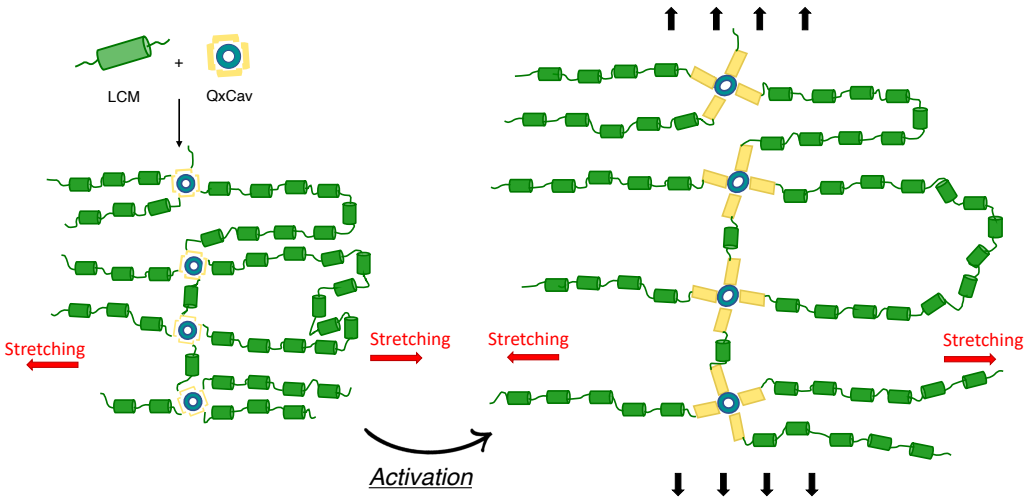

Figure 3.5. *Working principle of tetraquinoxaline cavitand-based LCE reported in this work.*

3.2. Results and discussion

3.2.1. Monomers synthesis

The first phase of the project focused on the synthesis of the liquid crystal monomer (LCM) depicted in **Scheme 3.1**. This first step involves the preparation of the aromatic core (rigid part of the monomer) through a condensation reaction starting from benzoic acid and hydroquinone.

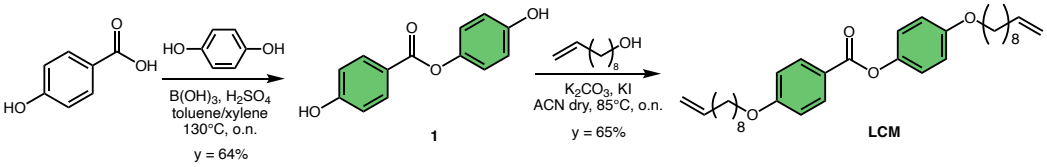

Scheme 3.1. *Synthesis of compound **1**.*

Subsequently, in the final step, product **1** was alkylated *via* a nucleophilic aromatic substitution using 10-bromodecene in presence of K_2CO_3 as base. The long aliphatic chain enhances the flexibility and mobility of the molecules and allows LCs to undergo more subtle conformational changes in response to stimuli. The purity of the monomer was confirmed via ^1H NMR (**Figure 3.A1**, Appendix Section) and GC-MS.

Moreover, IR spectrum (**Figure 3.6**) highlighted the relative stretching of the C=O (1722 cm^{-1}) and C=C (1606 cm^{-1}) functionalities.

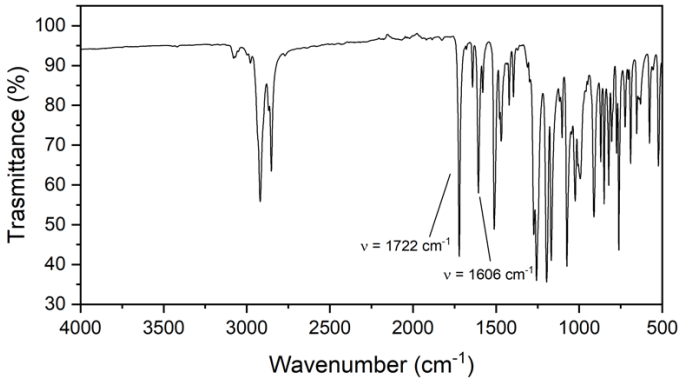

Figure 3.6. *IR spectrum of LCM.*

The LCM product was further characterized by differential scanning calorimetry (DSC) to determine its mesophase range. Nematic liquid crystals exhibit two primary transitions: the first one is related to the melting (T_M), which represent the transition from the crystalline state to the mesophase, and the second one is nematic to the isotropic transition (T_{NI}), indicating the transformation into the disordered state.

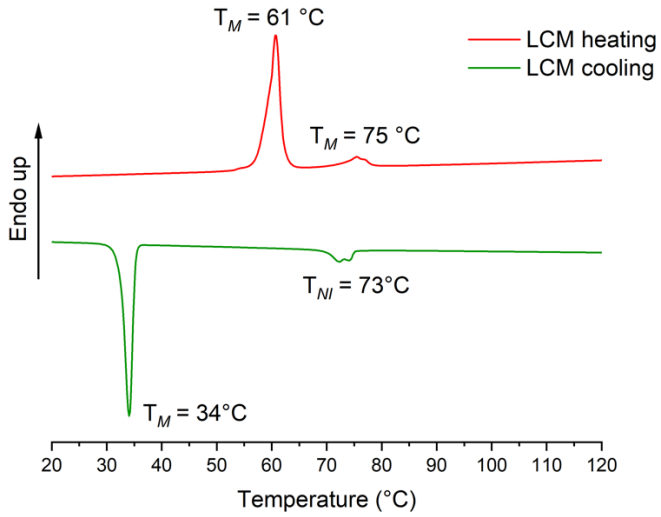

Figure 3.7. *DSC thermogram of* ***LCM****.*

The cooling curve (**Figure 3.7**, green line) shows the melting temperature at 40 °C while the isotropic transition temperature is 73 °C. The cooling curve does not coincide with the heating profile (red curve) due to the phenomenon known as overcooling, where rapid cooling prevents the proper rearrangements of mesogens, causing a shift in the transition peaks.

The DSC data were compared with the observation of LCM under polarized light microscope (POM) while heating the samples. The set-up of this instrument consists of a first entrance polarizer that polarizes the incident light on the sample and a second polarizer that interacts with the radiation departing the sample, which is perpendicular to the first. When an anisotropic material, such as the liquid crystal, is observed under polarized light microscopy, a phenomenon known as birefringence emerges. It occurs when a linearly polarized light ray travels through an anisotropic medium. As a result, there are two different exiting rays: an ordinary one that follows Snell's law and an extraordinary ray, which does not. This difference in the propagation velocities of light within the material results in distinct colors when observed under polarized light microscopy.[35]

The POM images presented in **Figure 3.8** depict the crystalline phase of LCM at room temperature, in the mesophase at 60 °C, and in the isotropic phase.

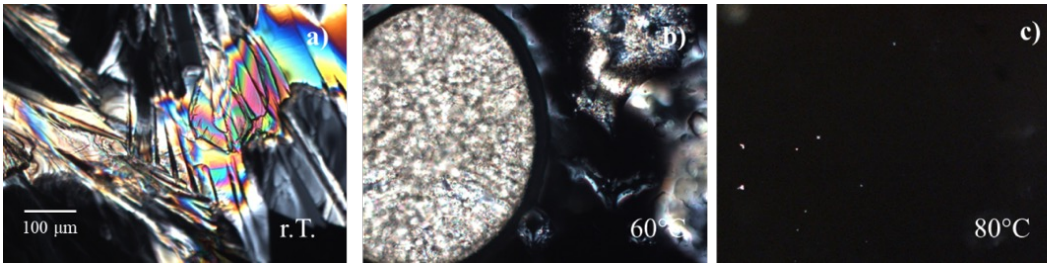

Figure 3.8. *POM images of LCM at room temperature (left) crystal phase, at 60°C (middle) nematic phase and 80°C (right) isotropic liquid.*

The molecules exhibit clear birefringence, also visible at room temperature due to the crystallinity of the samples. When is heated at 60°C, within the mesophase, a change in aspect and colors is visible. Beyond T_{NI}, at 80 °C, the material turns black

into a disordered isotropic liquid state that no longer exhibits birefringence. The observed T_M and T_{NI} temperatures are consistent with those measured using DSC.

With the aim of synthesizing NPR materials, tetraquinoxaline cavitands were then synthetized and used as crosslinker of liquid crystal elastomers. For this purpose, a tetraquinoxaline cavitand decorated with terminal alkenes on the four quinoxaline walls was prepared ($QxCav_u$). To provide an analogous crosslinker for control experiments, $QxCav_d$ bearing four double bonds at the lower rim was used. In this case, after the mechanical stress, quinoxaline walls remain in a vase conformation since they are not directly connected to the polymeric backbone.

The synthetic scheme of the two cavitands is reported in **Scheme 3.2**.

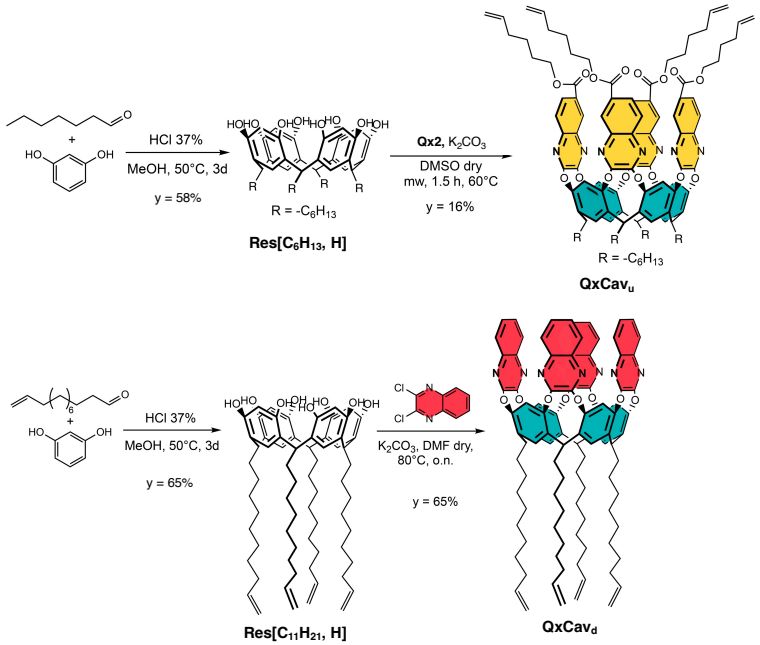

Scheme 3.2. *Synthetic pathways for the preparation of $QxCav_d$ and $QxCav_u$.*

Tetraquinoxaline cavitands were obtained through a bridging reaction with functionalized or non-functionalized quinoxalines. For the preparation of $QxCav_u$,[36] a proper decorated quinoxaline was first synthetized in two synthetical step (**Scheme 3.3**) starting from the commercial 3,4-diamino-benzoic acid and oxalic acid to obtain the heterocycle **Qx1** through a condensation reaction. The obtained intermediate was further chlorinated and directly employed for the nucleophilic acyl substitution with

ω-alkene alcohols to obtain **Qx2** which was characterized via GC-MS and ^{1}H NMR (see Appendix **Figure 3.A2**).

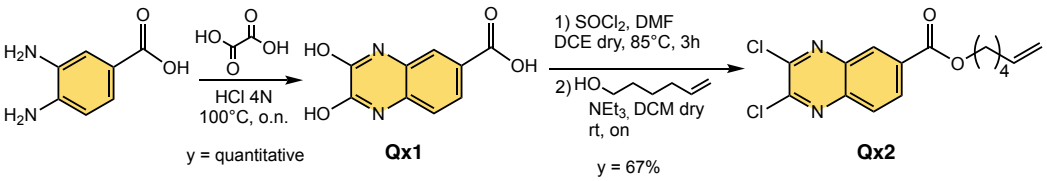

Scheme 3.3. *Synthetic scheme of Qx**2**.*

Tetraquinoxaline cavitand QxCav$_u$ was obtained *via* nucleophilic substitution of Qx2 directly on **Res[C$_6$H$_{13}$, H]**, according the recent procedure in literature.[36] The reaction was performed using microwave irradiation, allowing sensibly lower reaction time. The purification of the final product through column chromatography provided the cavitand in a low yield (16%). This is attributed to the formation of only one stereoisomer with C_{4v} symmetry (see **Scheme 3.2**) because of steric bias in the bridging reaction. After the initial statistical bridging, hindrance from the introduced aliphatic chains at the upper rim affects subsequent insertion, resulting in the sole isomer with functionalization in alternate position at expense of the overall yield. The pronounced symmetry is evident in sharp signals in the ^{1}H NMR spectrum and in the crystal structure of the cavitand[36] (**Figure 3.1A3** in the Appendix).

To provide an analogous crosslinker for control experiments, QxCav$_d$ bearing four double bonds at the lower rim was prepared. The bridging reaction in this case is between **Res[C$_{11}$H$_{21}$, H]**, previously prepared[36], and the commercial 2,3-dichloroquinoxaline, giving the final cavitand with 65% yield. ^{1}H NMR, reported in **Figure 3.A4**, confirm the purity of the product.

^{1}H NMR is also diagnostic to determine the cavitand conformation since the resonance of the methine groups of the macrocycle shift between *vase* (≈ 5.7 ppm) and *kite* (≈3.8 ppm) conformation.[37] Both QxCav$_d$ and QxCav$_u$ report the diagnostic triplet at 5.6 ppm, thus confirming the retention of *vase* conformation.

3.2.2. Polymer synthesis and materials preparation

Tetraquinoxaline cavitands presented in the previous paragraph were reacted with LCM to prepare LCEs materials (**Scheme 3.4**). Acyclic Diene Metathesis (ADMET) was selected as polymerization reaction exploiting the reactivity of the double bonds. It is a type of olefin metathesis commonly employed in in literature for the polymerization of terminal dienes.[38,39]

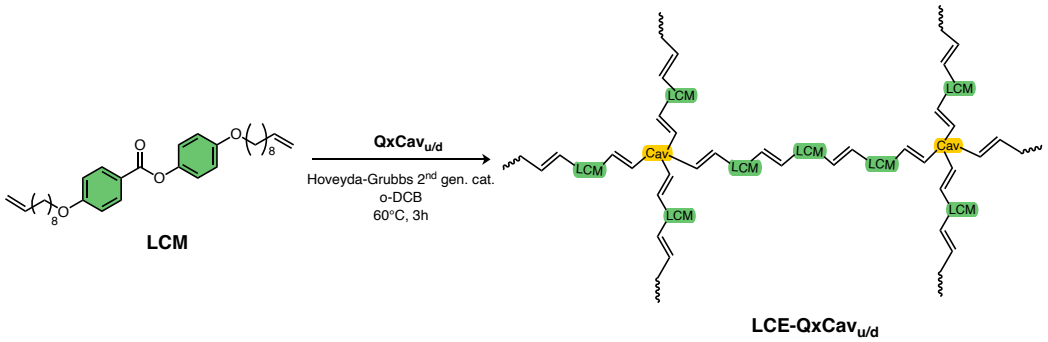

Scheme 3.4. *Schematic representation of the polymerization reaction for the preparation of LCEs using QxCavu or QxCavd.*

The mechanism (**Figure 3.9**) involves the use of a catalyst, typically a ruthenium-based carbene, that initiates the formation of a metallacyclobutane intermediate. This latter facilitates the insertion of additional dienes, either monomers or oligomers, followed by the release of a dimer or a polymer. The by-product of the reaction is ethylene, which, being gaseous, can be easily removed from the reaction environment, pushing the equilibrium toward polymer formation.

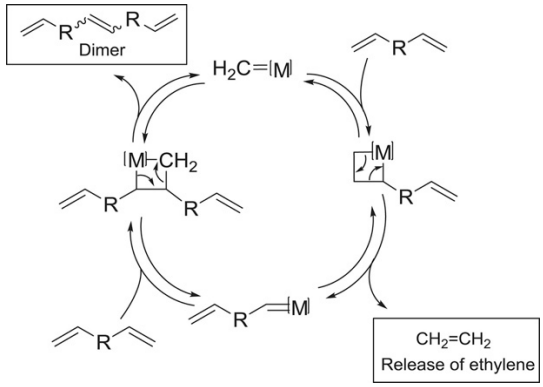

Figure 3.9. *Mechanism of ADMET polymerization reaction.[39]*

In this work, the Hoveyda-Grubbs catalyst 2nd generation was selected for the polymerization. After several failed trials with the conventional Grubbs catalyst, this catalyst was selected for the better efficiency in the reaction.[40] Diene insertion is easier because of the more labile ligand (ruthenium-phosphorous *vs* ruthenium-oxygen, **Figure 3.10**) attributable to an imperfect overlap between the oxygen and ruthenium orbitals. Both catalysts are sensitive to oxygen and moisture, and they must be handles under inert atmosphere.

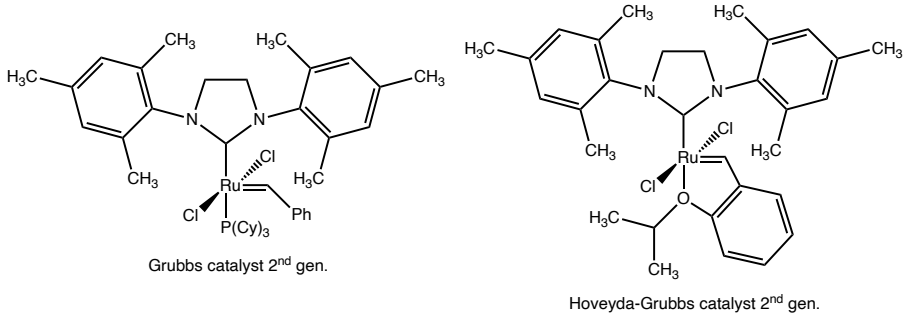

Figure 3.10. *Chemical structure comparison between Grubbs catalyst 2nd gen. (left) Hoveyda-Grubbs catalyst 2nd gen. (right).*

The selected molar crosslinking percentages for both active and reference polymer are 3% mol, 6% mol and 9% mol. Spcifically, a high crosslinking degree (9%) was selected to investigate whether liquid-crystalline properties were retained even at elevated levels of cavitand loading. Additionally, the lowest crosslinking degree (3%) was chosen to determine if the minimum amount of crosslinker sufficient to express

auxetic behavior. The network will be named as LCE-X%QxCav$_{u/d}$ where X is the molar percentage of QxCav$_{u/d}$.

The prepared networks were mechanically aligned to achieve a monodomain state. This is advantageous since it eliminates the necessity for disentanglement polymer chains during stretching, which minimizes energy dissipation. Additionally, uniform alignment maximizes the opening of cavitands, especially under mechanical stress. Preparation and alignment of LCEs have been performed following a protocol known in literature[41] and schematize in **Figure 3.11**.

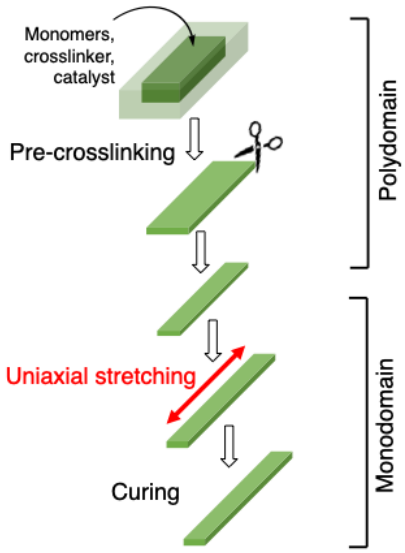

Figure 3.11. *Schematic alignment representation of LCEs.*

Experimentally, a mixture of LCM, QxCav$_{u/d}$ and the catalyst were dissolved in degassed o-DCB using a glove box to keep the inert atmosphere. To achieve the first partially crosslinking, the polymerization reaction was conducted for 3 h at 60 °C under constant nitrogen flow to remove ethylene. The obtained polydomain LCEs, after a specific amount of time for each sample (**Table 3.3** in the experimental section) were poured into a rectangular Teflon mold (13 cm x 1 cm), placed in an oven at 100 °C for 30 minutes to allow the material to diffuse in the mold (**Figure 3.12a**) and then cut into three stripes (4 cm x 1 cm). Each specimen was hung in the oven with a 40 g weight attached while maintaining a temperature within the

mesophase range (120 °C) for 10 minutes (**Figure 3.12b**). The resulting elongated films were than fixed on a glass support (**Figure 3.12c**) and placed in the oven at 100 °C to complete the curing of the network.

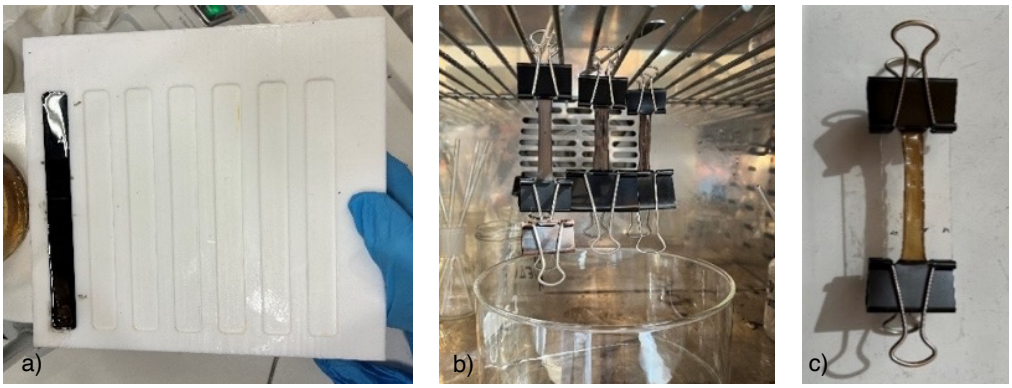

Figure 3.12. *a) LCEs casted in a Teflon, b) mechanical alignment of LCEs in the oven with a weight hanged, c) elongated samples fixed on a glass support.*

3.2.3. Non-active LCEs characterization (LCE-QxCavd)

The initial networks prepared were the non-active LCEs using QxCavd as crosslinker, easier to obtain compared to QxCavu, to verify the effective embedding in the liquid crystal network. FT-IR spectra of LCE-3%QxCavd, LCE-6%QxCavd and LCE-9%QxCavd are depicted in **Figure 3.13**.

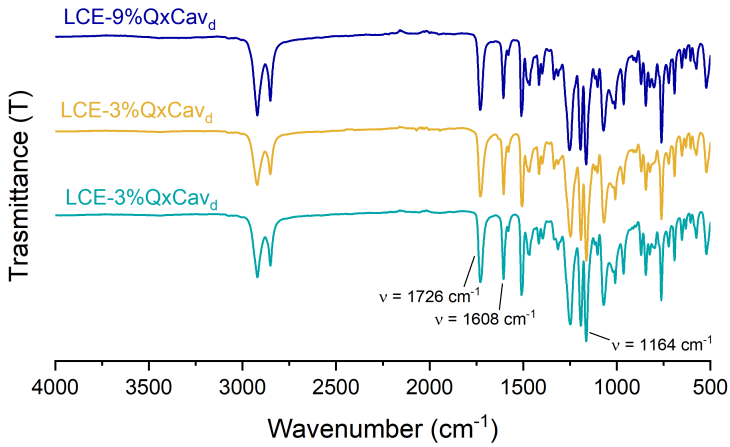

Figure 3.13. *IR spectra stacking of LCE-3%QxCavd (blue line), LCE-6%QxCavd (green line) and LCE-9%QxCavd (orange line).*

All the samples exhibit similar spectra. Looking for example to LCE-9%QxCav$_d$, C-H stretching are clearly visible at 2921 cm^{-1}, corresponding to sp$_2$ carbons, and at 2851 cm^{-1} for sp$_3$ carbons. The stretching of the ester linkage in the LCM core is present at 1726 cm^{-1}, while the peak at 1608 cm^{-1} is attributed to the stretching of the C=C double bonds. Lastly, at 1164 cm^{-1}, the stretching of C-N bonds is attributed to the quinoxaline rings.

The actual crosslinking was verified by estimating gel fraction of the polymers placing approximately 50 mg of samples in a vial in chloroform for two days. The results are 61%, 85% and 89% of gel content respectively for LCE-3%QxCav$_d$, LCE-6%QxCav$_d$ and LCE-9%QxCav$_d$. A discernible trend is evident, moving from the lowest LCE-3%QxCav$_d$ to the highest LCE-9%QxCav$_d$.

To assess the preservation of liquid crystal properties after crosslinking, DSC analyses were conducted to evaluate mesophase range (**Figure 3.14**).

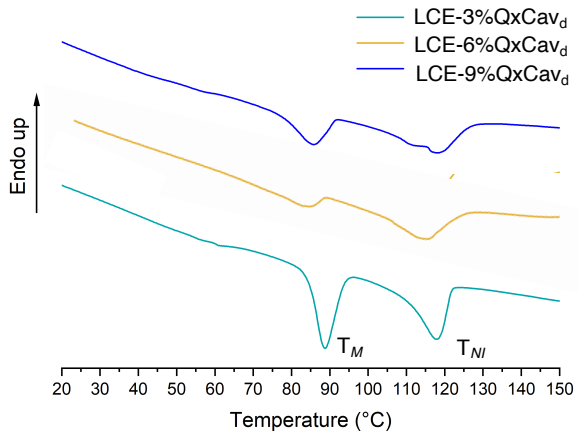

Figure 3.14. *DSC cooling curve of LCE-3%QxCav$_d$ (green line), LCE-6%QxCav$_d$ (orange line) and LCE-9%QxCav$_d$ (red line).*

It is noteworthy to emphasize that the two peaks delimiting the mesophase range are still present, although less pronounced compared to LCM, confirming the retention of liquid crystalline character. The peaks appear visibly broader and smaller compared to the monomer, ascribable to the reduced polymer mobility due to crosslinking. The mesophase range is comparable for all the samples analyzed

showing a mesophase starting around 85-88°C and a T_{NI} of about 117-119 °C. **Table 3.1** summarize the precise temperatures for each sample.

***Table 3.1**: T_M e T_{NI} values for the LCEs analysed.*

Network	T_M (°C)	T_{NI} (°C)
LCE-3%QxCav$_d$	88	119
LCE-6%QxCav$_d$	85	117
LCE-9%QxCav$_d$	86	117

Initially, the attention was directed towards LCE-6%QxCav$_d$. Specifically, a corresponding LCE with a non-aligned structure (LCE-6%QxCav$_d$-NA) was synthesized using the same procedure without the alignment procedure to investigate the distinction between the oriented pattern and the non-oriented one using POM images. The differences between the two surfaces are evident: the oriented sample displays a pattern of uniformly oriented lines (**Figure 3.15b** top), not observed in the non-oriented counterpart where a dotted pattern is present (**Figure 3.15a** top).

Another straightforward approach to unambiguously define the effective mesogens alignment is single crystal X-ray diffraction technique (XRD). LCEs display anisotropic behavior, therefore XRD can determine the degree and type of anisotropy. Notably, the non-oriented specimen exhibited a characteristic circular diffraction pattern typical of amorphous polymers (**Figure 3.15a** bottom) while a less homogeneity in the diffraction pattern is observed. Specifically, the diffraction spectrum obtained for the oriented LCE-6%QxCav$_d$ shows the characteristic pattern of nematic liquid crystals (**Figure 3.15b** bottom), demonstrating the nematic nature of the synthesized LCEs.[42]

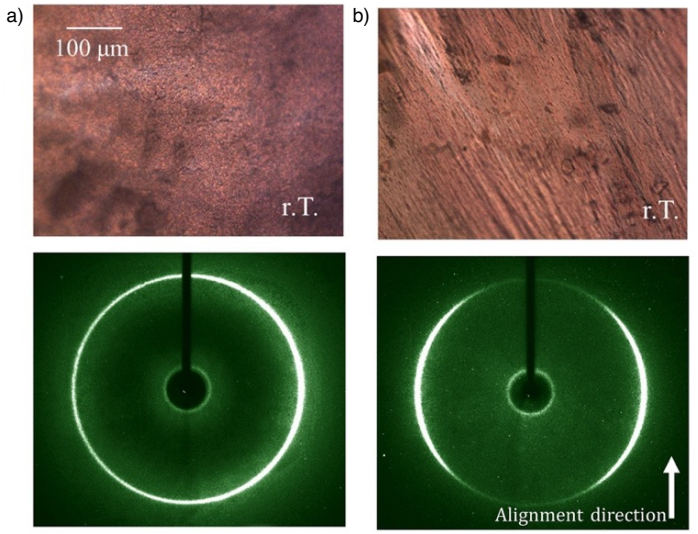

Figure 3.15. *POM images (top) of a) LCE-6%QxCav$_d$ and b) LCE-6%QxCav$_d$-NA and their diffraction pattern (bottom).*

Next, attention was focused exclusively on the oriented polymer observed under the polarized optical microscope at different temperatures. **Figure 3.16** groups all POM images at room temperature, within mesophase and above T_{NI} for of LCE-3%QxCav$_d$ (**Figure 3.16a**), LCE-6%QxCav$_d$ (**Figure 3.16b**), LCE-9%QxCav$_d$ (**Figure 3.16c**).

The phenomenon of birefringence, always observable for all specimens even at room temperature, confirms the retention of liquid crystal properties after crosslinking. Drastic color changes are noted when samples enter the mesophase, which was not observed anymore above T_{NI}, even though partial coloration is retained far above T_{NI} for LCE-6%QxCav$_d$ and LCE-9%QxCav$_d$ due to the fixed mesogens in the crosslinked materials.

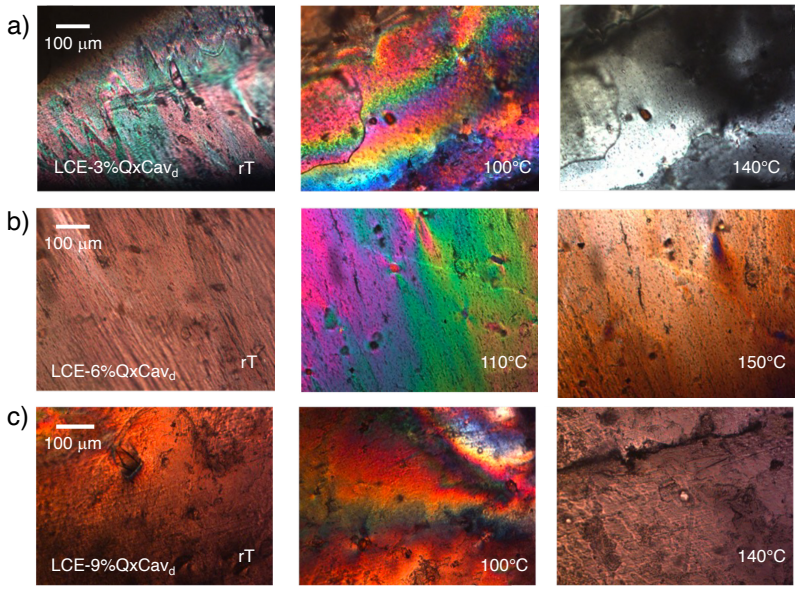

Figure 3.16. *POM images: a) LCE-3%QxCav$_d$ at rT (left), 100°C (middle), 140°C (right); b) LCE-6%QxCav$_d$ at rT (left), 110°C (middle), 150°C (right); c) LCE-9%QxCav$_d$ at rT (left), 120°C (middle), 140°C (right).*

3.2.4. Active LCEs characterization (LCE-QxCav$_u$)

Similarly, all active LCEs crosslinked with QxCav$_u$ were characterized. The infrared spectrum of the LCEs is identical for all the three networks. In **Figure 3.17** is reported the stacking spectra of LCM (green line), LCE-6%QxCav$_u$ (orange line) and **QxCav$_u$** (blue line).

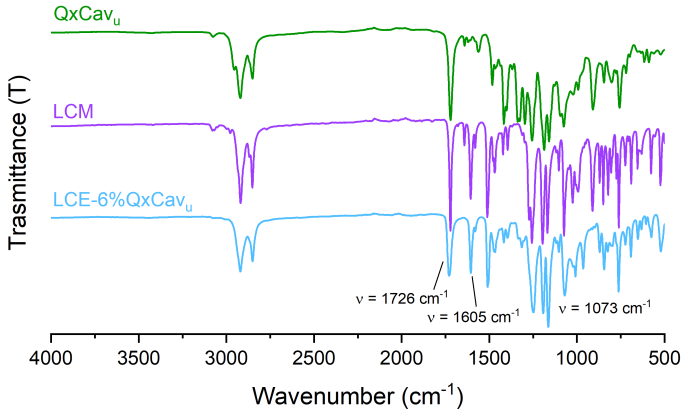

Figure 3.17. *IR spectra of LCE-6%QxCav$_u$, QxCav$_u$ and LCM.*

The stretching of C-H sp^2 and the C-H sp^3 are visible at 2918 cm^{-1} and 2846 cm^{-1} respectively. Additionally, peaks related to the carbonyl stretching at 1726 cm^{-1} and the C=C double bond stretching at 1605 cm^{-1} are visible. Finally, is present C-N bond stretching at 1160 cm^{-1} related to the quinoxaline moiety.

Analogous procedure for the estimation of gel fraction were performed leading to 55%, 70% and 84% of gel fraction for LCE-3%QxCav$_d$, LCE-6%QxCav$_d$ and LCE-9%QxCav$_d$ respectively.

Subsequently, DSC analyses (**Figure 3.18**) also demonstrated the liquid crystalline properties, as evidenced by the presence of both T_M and T_{NI} peaks.

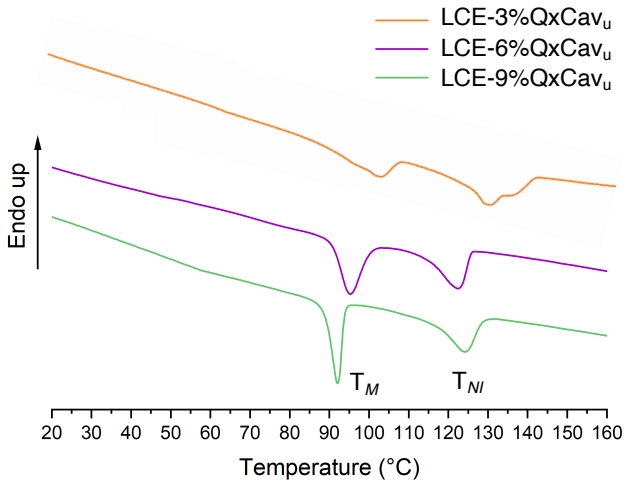

Figure 3.18. *DSC cooling thermogram of LCE-3%QxCav$_d$ (green line), LCE-6%QxCav$_d$ (orange line) and LCE-9%QxCav$_d$ (red line).*

The mesophase range is similar for all three polymers, as indicated in **Table 3.2**. However, a slightly shift of the temperature values is observed compared to the LCE-QxCav$_d$ materials, maintaining the same range of mesophases of around 30°C.

Table 3.2: T_M e T_{NI} values for the LCEs analysed.

Network	T_M (°C)	T_{NI} (°C)
LCE-3%QxCav$_u$	103	130
LCE-6%QxCav$_u$	97	123
LCE-9%QxCav$_u$	92	125

Finally, the liquid crystal elastomers (LCEs) were observed under a polarized light microscope while heating the samples.

Alignment of the mesogens was observed at room temperature for both LCE-6%QxCav$_u$ (**Figure 3.19b**) and LCE-9%QxCav$_u$ (**Figure 3.19c**), while only a partial alignment is visible for LCE-3%QxCav$_u$ (**Figure 3.19a**). Birefringence is also visible in all samples, although it is less evident than compared to the non-active specimens.

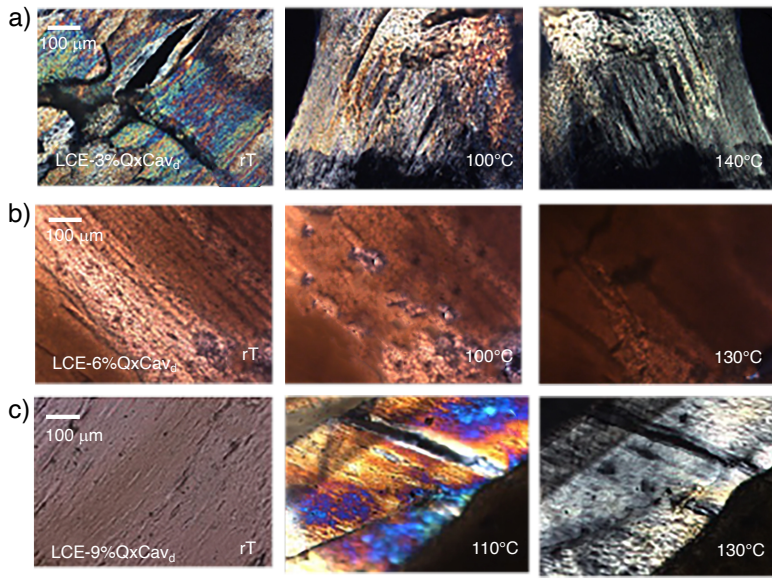

Figure 3.19. *POM images: a) LCE-3%QxCav$_{du}$ at rT (left), 100°C (middle), 140°C (right); b) LCE-6%QxCav$_u$ at rT (left), 100°C (middle), 130°C (right); c) LCE-9%QxCav$_u$ at rT (left), 100°C (middle), 130°C (right).*

To summarize, specimens containing QxCav$_u$ produce comparable results to those crosslinked with QxCav$_d$, exhibiting alignment at room temperature and strong birefringence in the mesophase range for all LCEs.

3.2.5. Mechanical characterization

LCE-9%Cav$_{u/d}$ were mechanically tested for the evaluation of Poisson's ratio using DIC technique. Theoretical expectations anticipate a positive Poisson's ratio for the non-active specimen crosslinked with QxCav$_d$, while a negative PR value is envisaged for the active specimen crosslinked with QxCav$_u$.

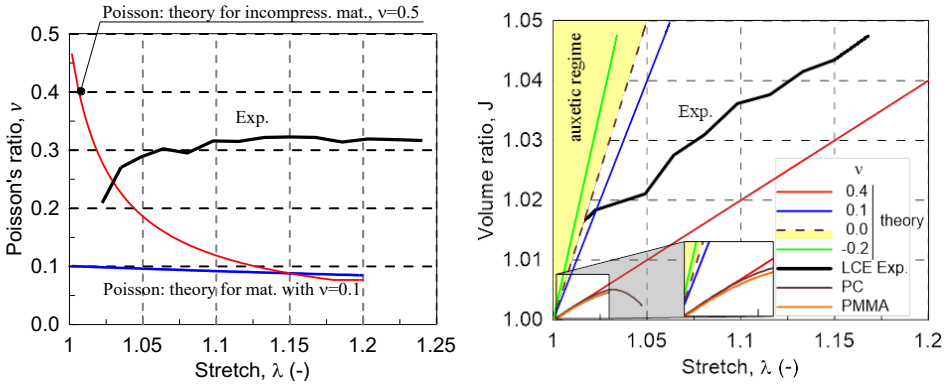

Figure 3.20. *Poisson's ratio (left) and average volume ratio (right) vs the applied stretch determined from DIC analyses for LCE-9%QxCav$_d$.*

LCE-9%QxCav$_d$ report ν = 0.3 (**Figure 3.20**), in the normal range of non-auxetic materials, as highlighted by comparison with polymethylmethacrylate (PMMA) and polycarbonates (PC).

On the contrary, the behavior of the active material LCE-9%QxCav$_u$ is anomalous (**Figure 3.21**). Due to significant experimental error, the curve within the red-shaded zone should be ignored as it pertains to minor deformations. Focusing instead on the green curve, which represents the behavior of the active network, a Poisson's ratio exceeding the maximum limiting value of ν = 0.5 is observed.

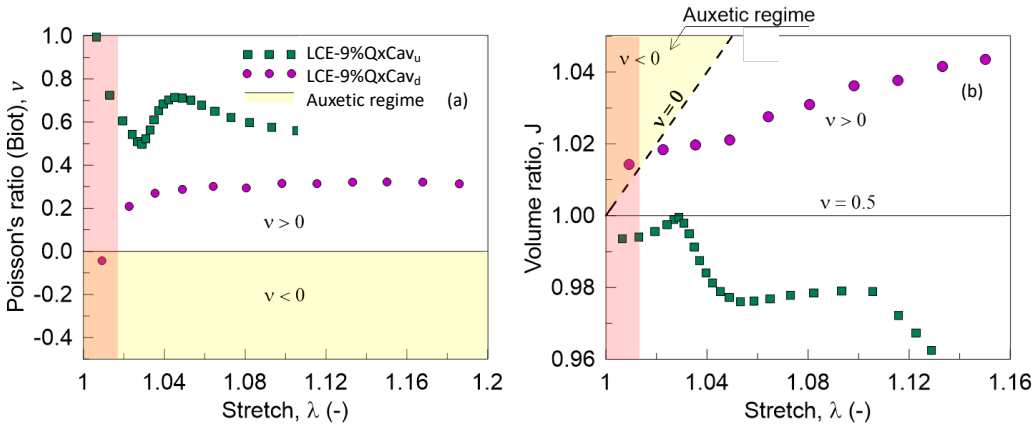

Figure 3.21. *Comparison of LCE-9%QxCav$_u$ and LCE-9%QxCav$_d$ PR value (a) and average volume ratio (b) vs the applied stretch determined from DIC analyses.*

The error may be due to the non-uniformity of the specimen used (**Figure 3.22**), which made it unsuitable for the analysis. Moreover, the necking of the specimen might suggest that during the alignment process, the stress applied partially opened the cavitand, minimizes a potential auxetic response. As final consideration, the measured anomalous positive PR value of LCE-9%QxCav$_u$, above the theoretical value, indicates that the LCE polymer presents an unusual behavior, which requires further studies.

Figure 3.22. *Appearance of LCE-9%QxCav$_u$ after alignment process.*

3.3. Conclusions

To achieve NPR behaviour upon unidirectional mechanical expansion, tetraquinoxaline cavitands are introduced as crosslinkers in highly oriented main chain liquid crystal elastomeric (LCE) networks. For this purpose, a proper mesogenic unit was synthetized, characterized and reacted with two different quinoxaline cavitands: $QxCav_u$, decorated at the upper rim with terminal alkenes and $QxCav_d$, bearing four double bonds functionalities at the lower rim, providing an analogous crosslinker for control experiment. The two cavitands were then separately reacted with the mesogens *via* metathesis in the presence of a Hoveyda-Grubbs 2nd generation catalyst. The selected molar crosslinking percentages for active and reference polymer vary from 3% mol (LCE-3%$QxCav_{u/d}$) to 9%mol (LCE-9%$QxCav_{u/d}$) to investigate whether liquid-crystalline properties were retained and the minimum amount necessary to observe auxetic response. Monodomain LCE are achieved by mechanical alignment, and then characterized via DSC and polarized optical microscopy. POM analyses highlighted birefringence of LCEs and the alignment of them as show from the homogeneous pattern reported, while DSC curves confirm the retaining of the liquid crystalline properties after the crosslinking reaction by showing a mesophase range from ≈85 °C to ≈125 °C for all LCEs analyzed. LCEs samples were tested with Digital Imaging Correlation (DIC) analysis to evaluate Poisson's ratio. However, the inhomogeneity of the samples hampered the observation of auxetic behavior.

Acknowledgements

Thanks to Prof. Roberto Brighenti and Matteo Montanari for the mechanical and DIC characterization.

3.4. Experimental section

Materials and methods

All reagents and solvent were purchased from certified commercial sources and used as received, without further purification.

^{1}H NMR spectra were recorded on Bruker 400MHz AVANCE or Jeol 600MHz using DMSO- d_6 and $CDCl_3$ as solvents. All chemical shifts (δ) were reported in parts for million (ppm) relative to proton resonances resulting from incomplete deuteration of NMR solvents. The abbreviations: s, d, t, m and sb indicated the spectrum peaks referred to: singlet, doublet, triplet, multiplet and broad singlet, respectively. The coupling constant (J) are expressed in Hz.

ATR-IR spectroscopy: Infrared absorption spectroscopy analyses were performed with a Perkin Elmer FT-IR Spectrum Two instrument using powder samples. The background was subtracted from every spectrum recorded.

Differential scanning calorimetry (DSC) analyses were performed with a Perking Elmer instrument, model DSC6000 with a heating rate of 10°C/min in air.

Polarized optical microscope images were recorded using an optical microscope Zeiss. Samples were placed on a glass support and heated from rT to 180°C.

Single-crystal X-ray diffraction (SCXRD): Intensity data and cell parameters were recorded at 200(2) K on a Bruker D8 Venture PhotonII diffractometer (CuKa radiation l = 1.54178 Å).

Tensile tests: Mechanical testing has been performed by using a universal testing machine Galdabini® Quasar 2.5 on rectangular specimens having the size 50x10x0.2 mm. A tensile stretch has been applied to the specimens at a constant deformation rate equal to $\dot{\lambda_x} = 5 \cdot 10^{-4}\ s^{-1}$ until the maximum deformation was reached. The specimens have been prepared for the mechanical testing by spray-painting a pattern of small irregular dots (size roughly between 0.1 and 0.5 mm) whose position is tracked, and the displacements quantified by the subsequent DIC analyses. Single or double cycle tensile mechanical tests have been conducted by recording the force and displacement with a frequency of 10 Hz, while pictures of the specimen (to be used in the digital image correlation (DIC) analyses) have been acquired by a Basler®

acA5472-17uc USB 3.0 camera with a resolution of about 3000x1000 pixels at a frequency of 1 Hz.

DIC measurements: The DIC analyses have been conducted by using the Ncorr[55] software by setting the region of interest (ROI, with size equal to about 30x7 mm). The deformations along the $x-$ and the $y-$ directions have been determined through the Ncorr post processing software. The average deformations required to determine the Poisson's ratio have been obtained by considering the values of the deformations evaluated through 6 virtual extensometers placed in x direction for determining the average deformation λ_x and 12 virtual extensometers placed in y direction for determining the average deformation λ_y.

4-hydroxyphenil 4-hydroxybenzoate (1)

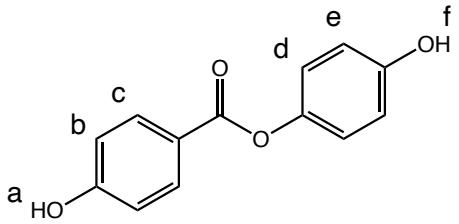

In a 100 mL flask were introduced 3 g (27 mmol) of hydroquinone and 2.9 g (21 mmol) of 4-hydroxybenzoic acid. Subsequently, 0.1 g (1.7 mmol) of H_3BO_3 was added, followed by the slow addition of 0.15 mL of H_2SO_4. The reaction was conducted at 130°C for 16 hours. The red precipitate present in the reaction mixture was then filtered under vacuum and thoroughly washed with a 1:1 mixture of H_2O/EtOH at 60°C until decolorization of the filtered solid. The resulting powder was dried under vacuum, resulting in 3.08 g (13.4 mmol) of product 1 with a 64% yield.

^{1}H NMR (DMSO-d_6, 400 MHz) δ (ppm): 10,46 (s, 1H, **H$_a$**), 9,43 (s, 1H, **H$_f$**), 7,95 (d, 2H, **H$_c$**, J = 8,8 Hz), 7,01 (d, 2H, **H$_b$**, J = 8,9 HZ), 6,91 (d, 2H, **H$_d$**, J = 8,8), 6,79 (d, 2H, **H$_e$**, J = 8,8 Hz)

ESI-MS (m/z): 231 $[M+H]^+$

4-(dec-9-en-1-yloxy)phenyl 4-(dec-9-en-1-yloxy)benzoate (LCM)

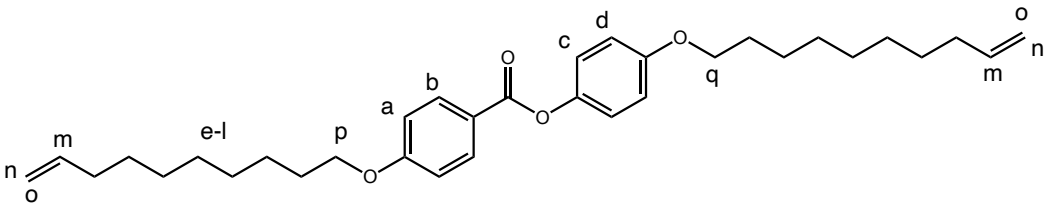

In a two-necked flask equipped with a condensator, under dry condition, compound **1** was dissolved in 28 mL of acetonitrile. Then 4.5 g (33 mmol) of K_2CO_3 and 2.1 g (14 mmol) of 1-bromodecane were added. The reaction was stirred at 85°C for 16 hours. Upon cooling, the precipitate was filtered on a Büchner and washed with acetone. The gray solid was dissolved in DCM and extracted three times with water. The resulting solid was then purified by column chromatography on silica (hexane → hexane/EtOAc 9:1). 2.17 g (4.34 mmol) of product **LCM** was obtained as a pale-yellow solid with a 65% yield.

^{1}H NMR ($CDCl_3$, 600 MHz) δ (ppm): 8,11 (d, 2H, **H_b**, J = 8,9Hz), 7,08 (d, 2H, **H_a**, J = 8,9 Hz), 6,94 (d, 2H, **H_c**, J = 9,1 Hz), 5,80 (m, 1H, **H_m**), 5,0 (dd, 1H, **H_o**, J_{trans} = 17,8 Hz, J_{gem} = 2,0 Hz) , 4,92 (dd, 1H, **H_n**, J_{cis} = 10,2 Hz, J_{gem} = 1,0 Hz), 4,03 (t, 2H, **H_p**, J = 6,5 Hz), 3,94 (t, 2H, **H_q**, J = 6,5 Hz), 2,5-1,12 (m, 28H, **H_{e-l}**)

IR: $\tilde{\nu}$ (cm^{-1}) = 2918 (C-H sp^2, str), 2851 (C-H sp^2, str), 1722 (C=O, str), 1606 (C=C alchene, str)

DSC: T_M= 40°C, T_{NI}=73°C

2,3-dihydroxyquinoxaline-6-carboxylate (Qx1)

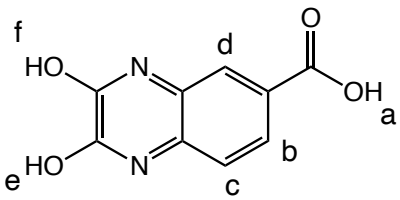

In two different beakers, 3.00 g (19.7 mmol) of 3,4-diaminobenzoic acid in 25 mL of 4M HCl and 1.97 g (21.9 mmol) of oxalic acid in 20 mL of 4M HCl were dispersed, respectively. The two suspensions were transferred to a 100 mL round bottom flask, resulting in a violet mixture. The flask was refluxed at 100°C for 16 hours. After cooling to room temperature, the obtained solid was filtered through *via* Büchner filtration and washed several times of water. A purple solid was obtained and dried under vacuum. Product 3 (3.9 g, 18.9 mmol) was obtained with a quantitative yield.

^{1}H NMR (DMSO-d_6, 400 MHz) δ (ppm): 12,88 (s, 1H, **H$_a$**), 12,15 (s, 1H, **H$_f$**), 12,03 (s, 1H, **H$_e$**), 7,74 (s, 1H, **H$_d$**), 7,69 (d, 1H, **H$_b$**, J = 8,4 Hz), 7,19 (d, 1H, **H$_c$**, J = 8,4 Hz)

ESI-MS (m/z): 207 $[M+H]^+$

Hex-5-en-1-yl 2,3-dihydroxyquinoxaline-6-carboxylate (Qx2)

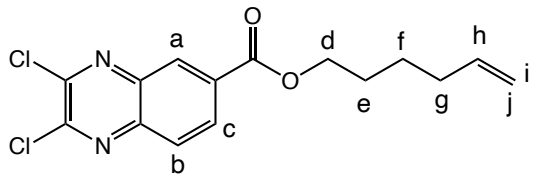

In a two-necked flask previously dried (3 cycles Ar/vacuum), 1.5 g (7.3 mmol) of compound **Qx1** was dissolved in 50 mL of dry DCE. Subsequently, 2.6 mL (36 mmol) of $SOCl_2$ and 30 drops of DMF were added. After refluxing for 3 hours, the solvent was removed under vacuum and the residue was dissolved in 50 mL of dry DCM. To this solution, 1.1 mL (8 mmol) of NEt_3 and 0.94 mL (8 mmol) of 1-undecene were added. The reaction mixture was stirred at room temperature for 16 hours under inert atmosphere. The mixture was then extracted with acidic water (HCl 1M), basic water (NaOH 1M), and finally with water. The organic phase was then dehydrated with $MgSO_4$, filtered, and dried yielding to a yellow-ochre oil. The crude reaction mixture was further purified by column chromatography on silica using DCM as the eluent. 1.56 g (4.8 mmol) of pure **Qx2** was obtained with a yield of 67%.

^{1}H NMR ($CDCl_3$, 400 MHz) δ (ppm): 8,75 (d, 1H, **H$_a$**, J = 1,8 Hz), 8,43 (dd, 1H, **H$_b$**, J_o = 7,0 Hz, J_p = 1,8 Hz), 8,11 (d, 1H, **H$_c$**, J = 8,2 Hz), 5,85 (m, 1H, **H$_h$**), 5,07 (dq, 1H, **H$_j$**, J_t = 15,2 Hz, J_g = 1,9 Hz), 5,02 (dq, 1H, **H$_i$**, J_c = 5,6 Hz, J_g = 2,1 Hz), 4,44 (t, 2H, **H$_d$**, J = 6,6 Hz), 2,18 (q, 2H, **H$_g$**, J = 7,9 Hz, J = 21,5 Hz) , 1,87 (m, 2H, **H$_e$**), 1.62 (m, 2H, **H$_f$**)

GC-MS (m/z): 226 ($M-O(CH_2)_4CH=CH_2$), 308,05 (M)

Tetra-ω-alkene ester functionalized quinoxaline cavitand (QxCav$_u$)

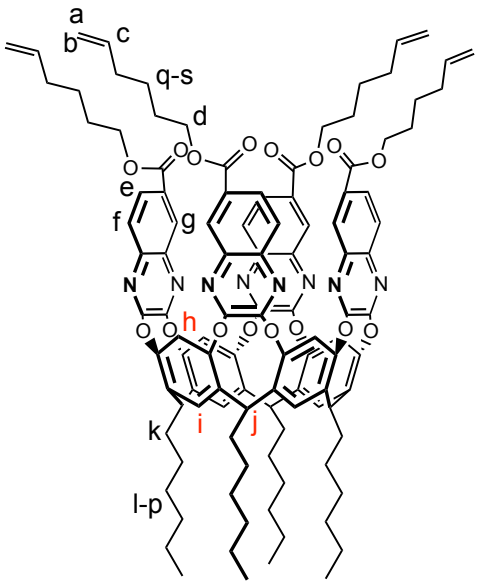

In a microwave reactor, under argon atmosphere, 0.153 g (0.185 mmol) of **Res[C$_6$H$_{13}$,H]** were dissolved in 6 mL di DMSO dry. Afterwards, 0.154 g (1.11 mmol) of K_2CO_3 was added. After 10 minutes, 0.280 g (0.816 mmol) of **Qx2** was added to the mixture. The reaction was then conducted in the microwave for 1 hour at 60°C (200 W). The reaction mixture was precipitated in water resulting in a beige precipitate, filtered *via* Büchner filtration and washed with water. The crude was further purified through silica gel column chromatography with a gradient elution (DCM → DCM/EtOAc 98/2). 56,7 mg (31 µmol) of white solid was obtained with a 17% yield.

^{1}H NMR ($CDCl_3$, 400 MHz) δ (ppm): 8,61 (d, 4H, **H$_g$**, J_{meta} = 1,9 Hz), 8,26 (s, 4H, **H$_h$**), 8,03 (dd, 4H, **H$_e$**, J_{meta} = 1,9 Hz, J_{orto} = 8,7 Hz), 7,86 (d, 4H, **H$_f$**, J_{orto} = 8,7 Hz), 7,24 (s, 4H, **H$_i$**), 5,85 (m, 4H, **H$_c$**), 5,57 (t, 4H, **H$_J$**, J = 7,7 Hz), 5,05 (dd, 4H, **H$_b$**, J_{trans} = 17,1 Hz, J_{gem} = 1,9 Hz), 4,98 (dd, 4H, **H$_a$**, J_{cis} = 10,2 Hz, J_{gem} = 1,1 Hz), 4,48 (t, 8H, **H$_d$**, J = 6,7 Hz), 1,91 (q, 8H, **H$_k$**, J = 8,5 Hz) 2,32-0,93 (m, 76H, **H$_{q-s}$**, **H$_{l-p}$**)

Tetra-alkene functionalized tetraquinoxaline cavitand lower rim (QxCav$_d$)

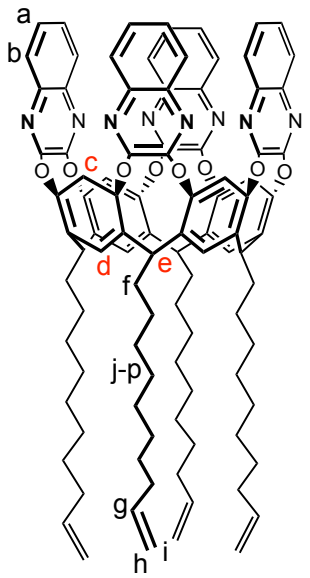

In a flask, after three cycles of vacuum/Ar, 1.5 g (1.44 mmol) of **Res[C$_{11}$H$_{21}$,H]** and 1.19 g (8.64 mmol) of K_2CO_3 were added to 30 mL of dry DMF. The mixture was allowed to react for 10 minutes, and then 1.26 g (6.34 mmol) of 2,3-dichloroquinoxaline were added. The reaction was left overnight at 80°C. The resulting brown suspension was precipitated in water and filtered under vacuum. The product was purified *via* column chromatography on silica (elution hexane/EtOAc 8:2). The final product appears as a white solid and was obtained with a yield of 65% (1.44 g, 0.93 mmol).

^{1}H NMR ($CDCl_3$, 400 MHz) δ(ppm): 8,17 (s, 4H, **Hc**), 7,82 (m, 8H, **Hb**), 7,49 (m, 8H, **Ha**), 7,23 (s, 4H, **Hd**), 5,85 (m, 4H, **Hg**), 5,58 (t, 4H, **He,** J = 7,9 Hz), 5,04 (dd, 4H, **Hi**, Jtrans = 17,1 Hz, Jgem = 1,7 Hz), 4,97 (dd, 4H, **Hh**, Jcis = 10,2 Hz, Jgem = 1,0 Hz), 2,28 (q, 8H, **Hf**, J = 6,9 Hz), 1,43 (m, 56H,**HJ-P**)

General procedures for the preparation of LCEs

In a glove box, a flask was equipped with a nitrogen valve and a rubber septum, previously dried with 3 cycles of vacuum/argon. **QxCav$_{u/d}$** and **LCM** were then dissolved in 1.9 mL of o-DCB, previously degassed by purging argon into the solvent. Finally, a catalytic amount of Hoveyda-Grubbs catalyst 2nd gen. was added. The green-colored reaction mixture was placed in an oil bath at 58°C under a constant flow of

nitrogen to remove the ethylene formed during the reaction. After approximately 2/3 hours, an increase in the viscosity of the reaction mixture was observed.
The dense mass was poured into a Teflon mold (13 cm x 1 cm) under nitrogen atmosphere. The mold was then placed in an oven at 100°C for 30 minutes. Once the polymer was removed from the mold, it was cut into strips of approximately 4 cm and each strip was stretched with weights of about 40 g in an oven at 120°C for 10 minutes. After removing the weights, each sample was fixed to a glass support with clamps and left at 100°C for two days to complete the curing process.

Table 3.3: Quantity of LCM and cavitands and reaction time necessary for the preparation of LCEs.

Entry	Cavitand mass (mg)	mmol cavitand	LCM mass (mg)	mmol LCM	Reaction time
LCE-9%QxCav$_u$	32,0	0,018	90	0,180	2h30’
LCE-6%QxCav$_u$	31	0,016	134	0,260	1h30’
LCE-3%QxCav$_u$	2	0,001	18	0,036	2h
LCE-9%QxCav$_d$	60,3	0,039	200	0,395	2h30’
LCE-6%QxCav$_d$	39,0	0,025	200	0,395	2h40’
LCE-3%QxCav$_d$	18,9	0,012	200	0,395	3h15’

LCE-3%QxCav$_d$

IR: $\tilde{\nu}$ (cm^{-1}) = 2923 (C-H sp^2, str), 2851 (C-H sp^2, str), 1726 (C=O, str), 1605 (C=C alchene, str), 1163 (C-N, str)
DSC: T_M= 88°C, T_{NI}= 117°C

LCE-6%QxCav$_d$

IR: $\tilde{\nu}$ (cm^{-1}) = 2923 (C-H sp^2, str), 2850 (C-H sp^2, str), 1726 (C=O, str), 1605 (C=C alchene, str), 1161 (C-N, str)
DSC: T_M= 85°C, T_{NI}= 117°C

LCE-9%QxCav$_d$

IR: $\tilde{\nu}$ (cm^{-1}) = 2921 (C-H sp^2, str), 2851 (C-H sp^2, str), 1726 (C=O, str), 1608 (C=C alchene, str), 1164 (C-N, str)
DSC: T_M= 86°C, T_{NI}= 119°C

LCE-3%QxCav$_u$

IR: $\tilde{\nu}$ (cm^{-1}) = 2922 (C-H sp^2, str), 2850 (C-H sp^2, str), 1727 (C=O, str), 1607 (C=C alchene, str), 1164 (C-N, str)
DSC: T_M= 103°C, T_{NI}=132°C

LCE-6%QxCav$_u$

IR: $\tilde{\nu}$ (cm^{-1}) = 2918 (C-H sp^2, str), 2846 (C-H sp^2, str), 1726 (C=O, str), 1605 (C=C alchene, str), 1160 (C-N, str)
DSC: T_M= 97°C, T_{NI}=123°C

LCE-9%QxCav$_u$

IR: $\tilde{\nu}$ (cm^{-1}) = 2919 (C-H sp^2, str), 2850 (C-H sp^2, str), 1719 (C=O, str), 1604 (C=C alchene, str), 1163(C-N, str)
DSC: T_M= 92°C, T_{NI}= 125°C

Appendix Chapter 3

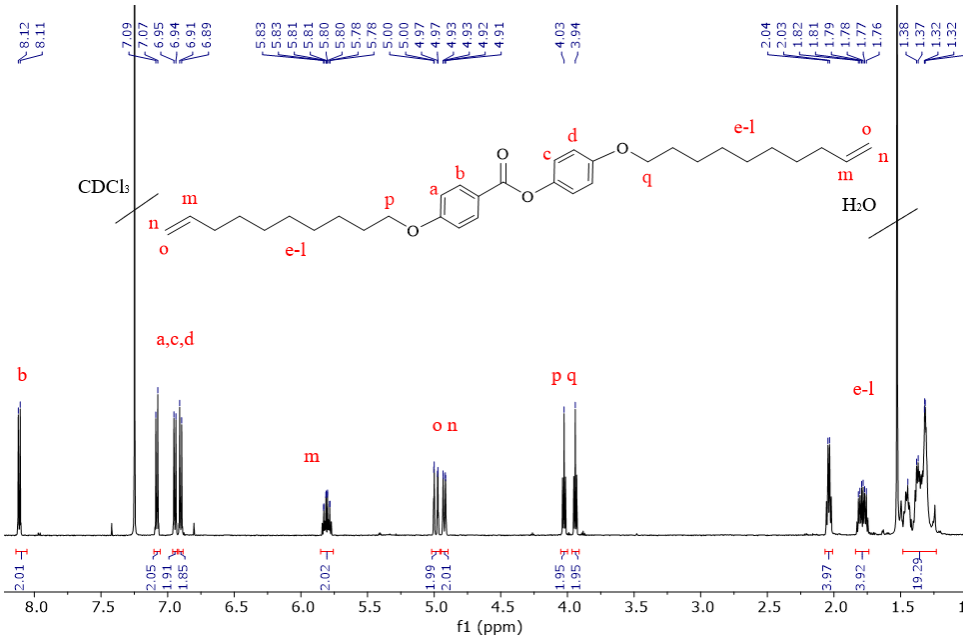

***Figure 3.A1**. ^1H NMR ($CDCl_3$, 400 MHz) of LCM.*

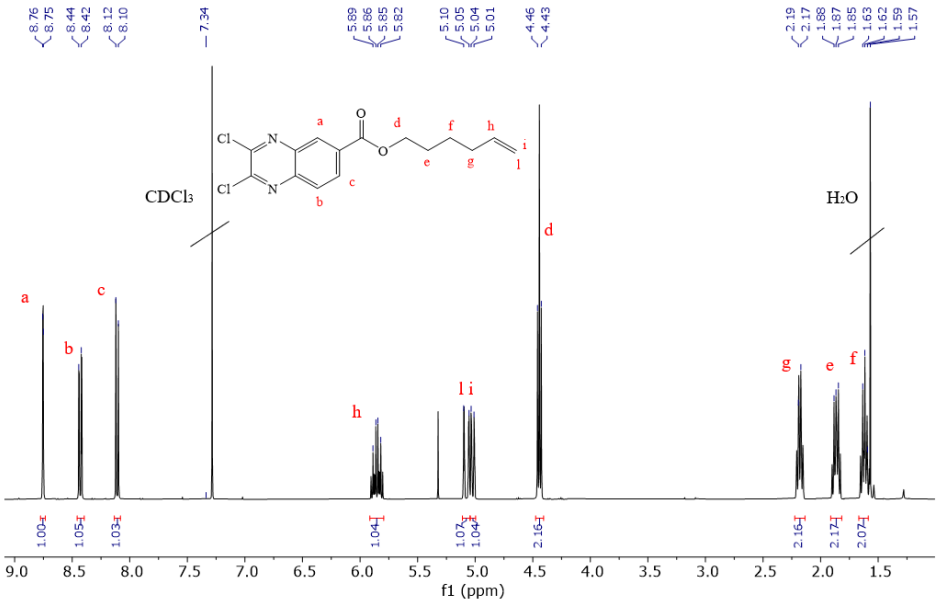

Figure 3.A2. *^{1}H NMR (CDCl$_3$, 400 MHz) of Qx2.*

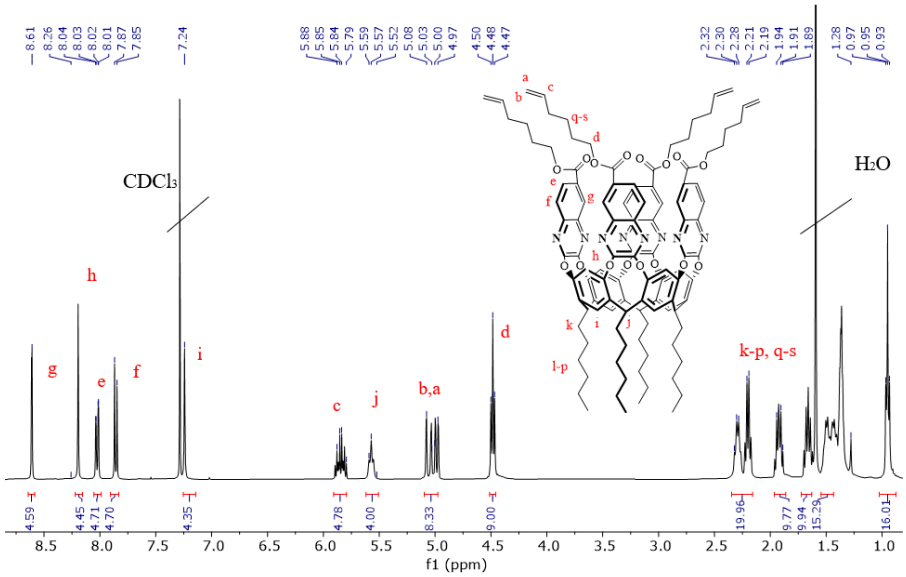

Figure 3.A3. *^{1}H NMR (CDCl$_3$, 400 MHz) of QxCav$_u$.*

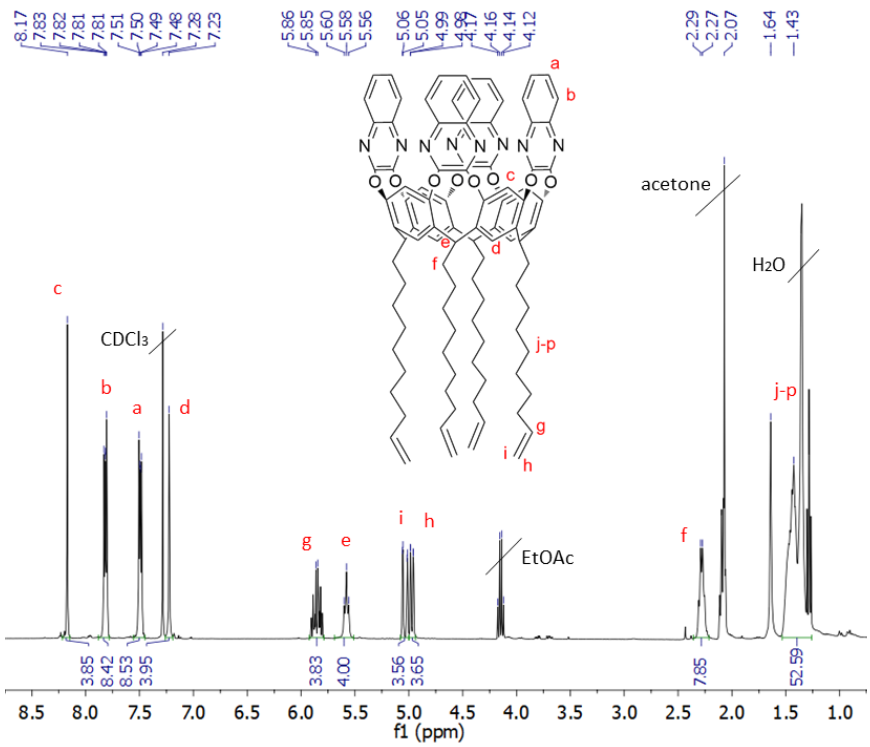

Figure 3.A4. *^{1}H NMR ($CDCl_3$, 400 MHz) of $QxCav_d$.*

References

[1] J. Hoogboom, J. A. A. W. Elemans, A. E. Rowan, T. H. M. Rasing, R. J. M. Nolte, *Phil. Trans. R. Soc. A.* **2007**, *365*, 1553.

[2] M. Warner, E. Terentjev, *Liquid Crystal Elastomers*, Clarendon Press, Oxford, **2007**.

[3] P.-G. de Gennes, J. Prost, *The Physics of Liquid Crystals*, Clarendon Press, Oxford, **2013**.

[4] P. Yeh, C. Gu, *Optics of Liquid Crystal Displays*, Wiley, Hoboken, N.J, 2010.

[5] P. J. Collings, M. Hird, *Introduction to Liquid Crystals Chemistry and Physics*, CRC Press, **2017**.

[6] M. Barnes, S. Cetinkaya, A. Ajnsztajn, R. Verduzco, *Soft Matter* 2022, *18*, 5074.

[7] T. J. White, D. J. Broer, *Nat. Mater.* **2015**, *14*, 1087.

[8] S. W. Ula, N. A. Traugutt, R. H. Volpe, R. R. Patel, K. Yu, C. M. Yakacki, *Liq. Cryst. Rev.* **2018**, *6*, 78.

[9] F. Brömmel, D. Kramer, H. Finkelmann, in *Liquid Crystal Elastomers: Materials and Applications* (Ed.: W. H. De Jeu), Springer Berlin Heidelberg, Berlin, Heidelberg, **2012**, pp. 1–48.

[10] C. Ohm, M. Brehmer, R. Zentel, *Adv. Mater.* **2010**, *22*, 3366.

[11] H. Finkelmann, G. Rehage, *Makromol. Chem., Rapid Commun.* **1980**, *1*, 31.

[12] G. H. F. Bergmann, H. Finkelmann, V. Percec, M. Zhao, *Macromol. Rapid Commun.* **1997**, *18*, 353.

[13] H. C. Kolb, M. G. Finn, K. B. Sharpless, *Angew. Chem. Int. Ed.* **2001**, *40*, 2004.

[14] H. Yang, A. Buguin, J.-M. Taulemesse, K. Kaneko, S. Méry, A. Bergeret, P. Keller, *J. Am. Chem. Soc.* **2009**, *131*, 15000.

[15] J. Lub, D. J. Broer, N. Van Den Broek, *Liebigs Ann./Recl.* 1997, ***1997***, 2281.

[16] C. M. Yakacki, M. Saed, D. P. Nair, T. Gong, S. M. Reed, C. N. Bowman, *RSC Adv.* **2015**, *5*, 18997.

[17] C. N. Bowman, C. J. Kloxin, *Angew. Chem. Int. Ed.* **2012**, *51*, 4272.

[18] C. J. Kloxin, T. F. Scott, B. J. Adzima, C. N. Bowman, *Macromolecules **2010***, *43*, 2643.

[19] Z. Wang, H. Tian, Q. He, S. Cai, *ACS Appl. Mater. Interfaces* **2017**, *9*, 33119.

[20] T. Ube, K. Kawasaki, T. Ikeda, *Adv. Mater.* **2016**, *28*, 8212.

[21] M. K. McBride, M. Hendrikx, D. Liu, B. T. Worrell, D. J. Broer, C. N. Bowman, *Adv. Mater.* **2017**, *29*, 1606509.

[22] D. W. Hanzon, N. A. Traugutt, M. K. McBride, C. N. Bowman, C. M. Yakacki, K. Yu, *Soft Matter* **2018**, *14*, 951.

[23] Y. Yang, Z. Pei, Z. Li, Y. Wei, Y. Ji, *J. Am. Chem. Soc.* **2016**, *138*, 2118.

[24] Y. Yu, T. Ikeda, *Angew. Chem. Int. Ed.* **2006**, *45*, 5416.

[25] J. Sun, C. Wang, Y. Liu, X. Liang, Z. Wang, *Int. J. Smart Nano Mater.* **2023**, *14*, 440.
[26] Y. Chen, C. Chen, H. U. Rehman, X. Zheng, H. Li, H. Liu, M. S. Hedenqvist, *Molecules* **2020**, *25*, 4246.
[27] J. Küpfer, H. Finkelmann, *Makromol. Chem., Rapid Commun.* **1991**, *12*, 717.
[28] H.-W. Chen, J.-H. Lee, B.-Y. Lin, S. Chen, S.-T. Wu, *Light Sci. Appl.* **2017**, *7*, 17168.
[29] T. H. Ware, M. E. McConney, J. J. Wie, V. P. Tondiglia, T. J. White, *Science* **2015**, *347*, 982.
[30] T. H. Ware, T. J. White, *Polym. Chem.* **2015**, *6*, 4835.
[31] H. Aharoni, Y. Xia, X. Zhang, R. D. Kamien, S. Yang, *Proc. Natl. Acad. Sci. U.S.A.* **2018**, *115*, 7206.
[32] S. Schuhladen, F. Preller, R. Rix, S. Petsch, R. Zentel, H. Zappe, *Adv. Mater.* **2014**, *26*, 7247.
[33] Y. Yao, J. T. Waters, A. V. Shneidman, J. Cui, X. Wang, N. K. Mandsberg, S. Li, A. C. Balazs, J. Aizenberg, *Proc. Natl. Acad. Sci. U.S.A.* **2018**, *115*, 12950.
[34] A. Kotikian, R. L. Truby, J. W. Boley, T. J. White, J. A. Lewis, *Adv. Mater.* **2018**, *30*, 1706164.
[35] R. Oldenbourg, *Cold Spring Harb. Protoc.* ***2013***, 078600.
[36] M. Torelli, F. Terenziani, A. Pedrini, F. Guagnini, I. Domenichelli, C. Massera, E. Dalcanale, *ChemistryOpen* **2020**, *9*, 261.
[37] J. R. Moran, J. L. Ericson, E. Dalcanale, J. A. Bryant, C. B. Knobler, D. J. Cram, *J. Am. Chem. Soc.* **1991**, *113*, 5707.
[38] L. Caire Da Silva, G. Rojas, M. D. Schulz, K. B. Wagener, *Prog. Polym. Sci.* **2017**, *69*, 79.
[39] H. Li, L. Caire Da Silva, M. D. Schulz, G. Rojas, K. B. Wagener, *Polym. Int.* **2017**, *66*, 7.
[40] L. Liu, M. Wang, L.-X. Guo, Y. Sun, X.-Q. Zhang, B.-P. Lin, H. Yang, *Macromolecules* **2018**, *51*, 4516.
[41] L. Liu, M.-H. Liu, L.-L. Deng, B.-P. Lin, H. Yang, *J. Am. Chem. Soc.* **2017**, *139*, 11333.
[42] F. Zhang, P. A. Heiney, A. Srinivasan, J. Naciri, B. Ratna, *Phys. Rev. E* **2006**, *73*, 021701.

Chapter 4

Introduction on covalent adaptable networks

4.1. Thermoplastic vs thermoset

Nowadays, it is impossible to overlook the use of plastic, undeniably linked to our technological advancements for its variety of application in short and long term such as packaging, biocompatible tools, construction. Polymers are not only fundamental for scientific progresses but represent a severe challenge for our society as plastic waste and pollution have quickly become environmental issues.[3] In general polymer materials can be divided in two main classes depending on their thermal behavior: thermoplastics and thermosets. Thermoplastics, which are composed of long linear chains entangled and kept together by physical interaction, can be melted upon heating. The viscosity drops at high temperatures and the ability to flow allow these polymers to be easily processed. For this purpose, thermoplastics are part of our daily life in many consumer products such as plastic bottles (PET), packaging (PE, polypropylene), medical consumables.[3] Their recyclability is limited by the incompatibility of many polymers (i.e. multilayered material), thus requiring a long process of sorting, separating and cleaning. Furthermore, thermoplastics are prone to creep and so not suitable for applications requiring high thermal stability and high mechanical performances.

The second group of materials are thermosets. In these polymers, chains are crosslinked with covalent bonds, forming a 3D network and therefore they offer robustness and resistance against chemicals and mechanical stress. Upon heating they decompose rather than flow. The excellent thermal stability and resistance to creep render them the materials of choice in composite materials, as part of airplanes, cars, windmill blades, etc. However, given the high degree of connectivity among chains,

they cannot undergo to any modification of their chemical structure, thus making them not reprocessable.

The incorporation of dynamic bonds into polymers, blending the robust mechanical features of thermosets with the recyclability of thermoplastics, holds significant interest in the field of polymer chemistry.

One way to introduce dynamic crosslinks is through the incorporation of non-covalent interactions, that lead to a physical crosslinking of the chains.

To cite a few examples, non-covalent interactions may arise from hydrogen bonding,[4] π-π stacking,[5] ion pairing,[6] metal-ligand coordination,[7] etc… The thermoreversible nature of the physical cross-links enables the formation of polymer materials with enhanced mechanical properties without compromising their reprocessability. Upon heating, the interactions are disrupted, and the material will behave as a viscoelastic liquid, thereby facilitating the reprocessing.

An alternative approach for the development of dynamic materials is the use of exchangeable covalent bonds. The introduction of covalent dynamic crosslinked materials was reported for the first time in 2010 by Bowman's research group, whose developed the concept of Covalent Adaptable Networks (CANs).[8] Those crosslinked polymers contain covalent reversible bonds that create a polymer with potentially malleability when exposed to external stimuli, such as heat or light.[9] They can undergo bonds cleavage or exchange without decomposition.

4.2. Covalent adaptable networks (CANs)

As mentioned in the previous paragraph, the term CAN refers to a class of materials that are designed to have dynamic and adaptable covalent bonds within their structures. Unlike traditional covalent materials where bonds are typically strong and permanent, CANs contain covalent bonds that can break and reform reversibly under certain conditions, allowing the material to adapt to external stimuli. CANs can be classified in two categories depending on the network rearrangement mechanism: associative CANs and dissociative CANs.

In associative CANs, a new bond is formed before a crosslink is broken, thus resulting in a decrease of viscosity while maintaining network integrity even under external stimulus and at high temperature. In dissociative CANs, dynamic bonds are broken before a new one is formed (***Figure 4.1***).[10] There is a thermodynamic and kinetic distinction that must be taken into account.

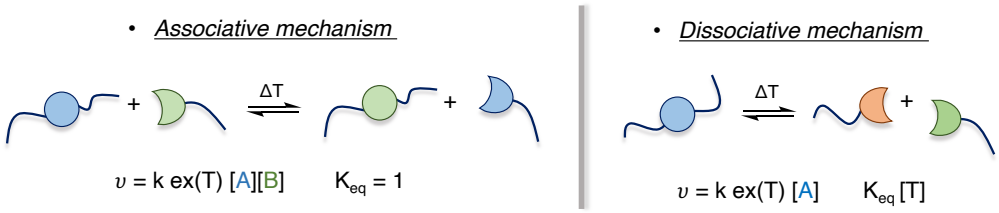

Figure 4.1. *Overview of the associative (left) and dissociative (right) rearrangements mechanism. (adapted from reference 11)*

In associative CANs the reaction kinetics is defined by the availability of two distinct species: a reactive crosslink (A) and a chain end (B), which represent the site of the new crosslink. Increasing the reactive free chain, the exchange reaction speeds up. In principle, during association, the connectivity of the network temporarily increases in the intermediate state. However, due to the short life of the intermediate, crosslinking density is assumed constant ($K_{eq} = 1$). The network does not undergo depolymerization, although it flows when heated and shows high resistance to solvent dissolution. Looking at the unique behavior of these materials, Liebler in 2011 named them "vitrimers" (extensive discussion in the next paragraph). In dissociative CANs, the presence of free chain ends is less important since crosslinks are the only species that control the equilibrium. Polymer segments dissociation lead to a formation of free end chains, entropically favored. This process can be more extensive by increasing the temperature of the system ($K_{eq}[T]$). As a result, the network will lose its integrity, thus making its complete dissolution possible in principle.

4.3. Dissociative CANs

Dissociative Covalent Adaptable Networks are a class of dynamic polymer networks where the formation of new covalent crosslinks occurs after the initial breaking of

other bonds within the network. In simpler terms, the polymer chains fragment first and then they reassociate in a different configuration.

The properties of dissociative CANs are significantly influenced by the equilibrium of the exchange reaction. The viscosity profiles during these exchange reactions can vary considerably, depending on how easily the equilibrium shift from associate to non-dissociate state. This process is indeed regulated by thermodynamic factors, including reaction enthalpy and entropy following Van't Hoff equation (1).

$$R \ln K = \frac{-\Delta H^{\circ}}{T} + \Delta S \quad (1)$$

The enthalpic factor (ΔH) favors the associate state whereas the entropic contribution (ΔS) is higher in the dissociation process. Consequently, as the temperature rises, the impact of enthalpic factor is reduced and the equilibrium tends to favor the entropically driven dissociation of the dynamic bonds. When sufficient dissociation takes place due to a significant shift in the bonding equilibrium, it leads to a depolymerization reaction, which reduces the density of crosslinks and the overall viscosity of the material. Upon cooling, the thermodynamic equilibrium shifts back to association, resulting in a recovery of material properties. Slightly changes in enthalpy or entropy may significantly affect network connectivity at a given temperature.

However, a gel-sol transition accompanied with a decrease of viscosity is not always feasible in dissociative CAN.

In ***Figure 4.2*** two examples of dissociative networks with same activation energy for the debonding but different reaction energy for rebonding are schematized: in one case fast formation of bond between chain ends while in the other slower reformation of the dynamic moiety. This aspect has implication in the viscosity profile of the networks, resulting in a different macroscopic property even if the exchange mechanism is the same. If the contribution of the enthalpic factor is large (***Figure 4.2a***), the association is favored over dissociation, therefore high temperature would be necessary to overcome the driving force towards associate state. In this case network integrity will be maintained, since association is preferred, and the viscosity profile will be similar to the one of vitrimers. A clear example is reported by Rowan and coworkers[12] in their work about thermally delayed dissociation of sterically hindered urea (***Figure 4.2a*** bottom).

Depending on the bulkiness of the amine used, the urea bond dissociates into its corresponding isocyanate and amine. The more hindered is the urea the more the equilibrium is shifted toward dissociation, resulting in ΔH values that can shift from 110 to 80 kJ·mol^{-1} corresponding in a shift of 50 °C of the temperature at which the dissociation initiate.

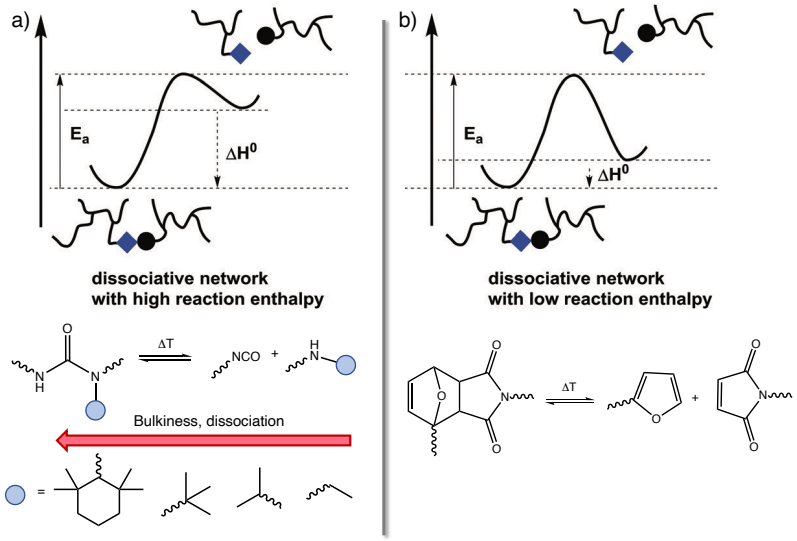

Figure 4.2. *Examples of dissociative CANs with same E_a but different reaction enthalpy: a) high reaction enthalpy and hindered urea as an example (bottom), b) low reaction enthalpy and Diels Alder reaction (bottom). Image adapted from reference [10].*

On the contrary, with a low reaction enthalpy (***Figure 4.2b***), dissociation is faster than association, less energy is needed to favor the entropically dissociated state, and a temperature increase would significantly affect the equilibrium constant. In this scenario, the network will lose its integrity, since the dissociate state is favored, resulting in a viscosity drop. One example is given by Diels-Alder (DA) chemistry (***Figure 4.2b bottom***), first described between furans and maleimides in 1969.[13] The reaction occurs at room temperature, or at 60 °C to fastening the reaction rate. However, upon temperature threshold (around 100 °C) the retro DA is favored, and the equilibrium is shifted toward the dissociate state.

Several dissociative mechanisms are already reported in literature, a more comprehensive list of dissociative CANs is showed in ***Table 4.1***.

Table 4.1. *Overview of dissociative covalent adaptable network platforms.*

Dynamic chemistry	***Reaction scheme***
Isocyanate reversion (urea (X = N)[14], urethane (X = O)[15]	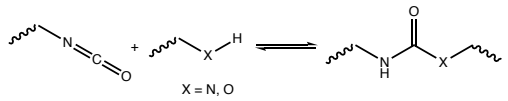
Transesterification of phthalate monoester[16]	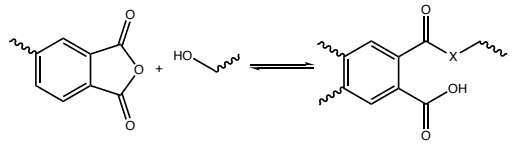
Amide-imide exchange[17]	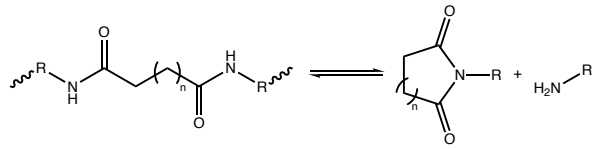
Aza (X = NH_2)[18]/Thia (X = SH)[19]-*Michael addition*	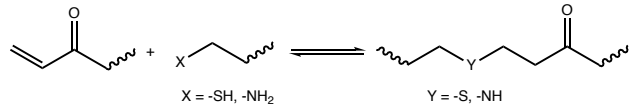
Diels-Alder cycloaddition[20]	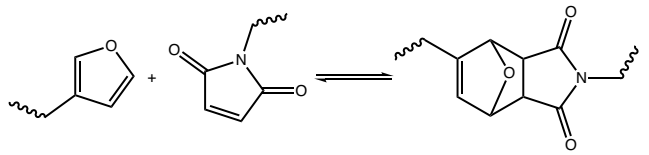
Alder-ene reaction Indole-triazolinedione (TAD)[21]	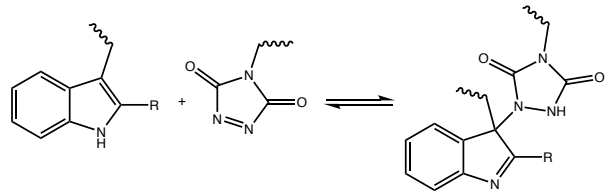

4.4. Associative CANs: vitrimers

Associative CANs mechanism consists of two simultaneous steps: a new covalent bond is formed replacing an identical one. As a result, the crosslinking density remain constant over time and the viscosity decreases gradually under heating allowing the networks to change their topology and thus to be processed in a viscous liquid state while maintaining the network integrity. The preservation of the network connectivity

makes these materials more resistant to dissolution, even at high temperatures, or solvent stress cracking.

The first example of associative CAN was reported by Bowman and coworkers based on photo-induced free radical addition-fragmentation chain transfer reaction of allyl sulfide moieties (***Figure 4.3***).[22]

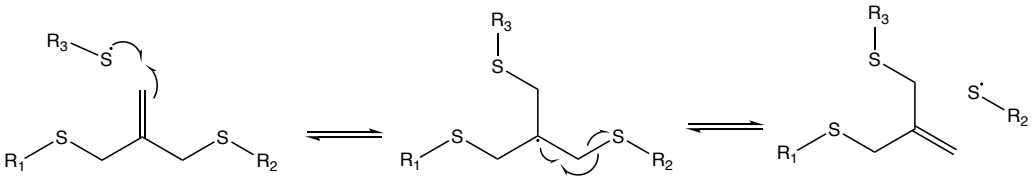

Figure 4.3. *Mechanism of radical addition-fragmentation of allyl sulphides reaction used by Bowman in 2005.*[22]

Later, associative CANs were developed on a similar exchange mechanism using trithiocarbonates.[23] In presence of a photo-radical initiator, these networks exhibit a photo-induced stress relaxation. However, despite the interesting properties, the lifetime of the materials was limited due to radical recombination and disappearance of radical photo-initiator. In 2011, Leibler and co-workers reported an example of associative CAN based on transesterification reactions of epoxy acid polyester based network.[24] The Authors coined these materials as "vitrimers" in relation to the unique viscosity behavior: a gradually decrease upon heating like vitreous silica.

The viscoelastic behavior of vitrimers can be described by two different temperatures. The first one is the classical glass transition temperature, T_g, linked to chains mobility. The second temperature is called topology freezing transition temperature (T_v) and describe the transition from viscoelastic solid to viscoelastic liquid. Above this temperature dynamic covalent exchange become relevant, allowing the materials to change their topology. These materials can be then easily reshaped, healed, or reprocessed. By cooling the network, the bonds exchange became significantly slower, thus the molecular network retains its configuration. By Liebler's definition, T_v was firstly described as the temperature at which the melt viscosity of the materials reach 10^{12} Pa·s.[24] However, this does not imply that no exchange reactions take place below this temperature. The relative arrangement of the T_v and T_g has important

implication on the mechanical behavior. Comparing the scenario where topology freezing transition temperature is above or below T_g provides insights into how these two critical temperatures affect the properties and behavior of the materials. Moreover, viscosity is a crucial property to consider in vitrimers since is directly related to their dynamic nature. The most common case is the one in which T_v is above T_g (***Figure 4.4a***). Once reached the T_v, the materials macroscopically flow following an Arrhenius-type temperature dependence since the exchange mechanism is predominant. In the other case ($T_g > T_v$, ***Figure 4.4b***), the exchange dynamics are not fast enough due to the frozen polymeric chains. The viscosity profile follows Williams-Landel-Ferry (WLF) profile in the first stage since the limiting factor is still chains mobility. Upon further heating, Arrhenius-type dependency is obtained as the exchange reactions are not frozen anymore. This behavior was observed and described by Guan and coworkers in 2018.[25]

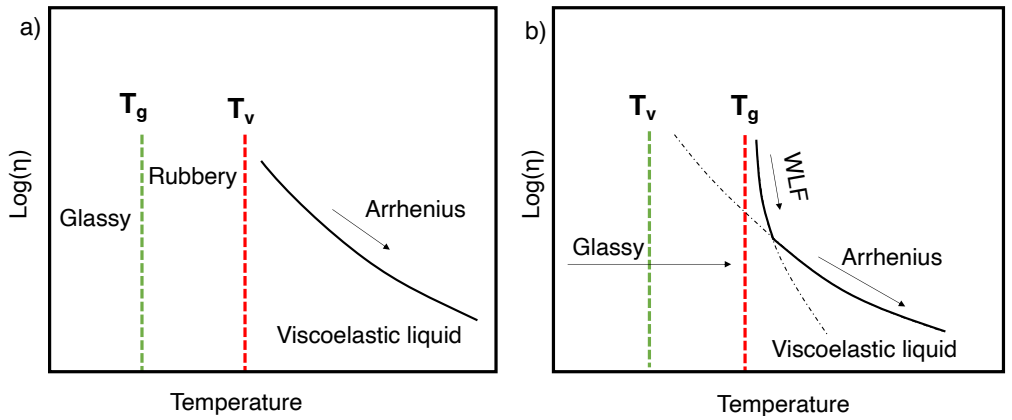

Figure 4.4. *Viscoelastic behavior of vitrimers. a) Case with T_g lower than T_v: the viscosity follows Arrhenius-type temperature dependency. B) Scenario in which T_v is lower than T_v. In this case the flow became significant only above T_g resulting in a WLF + Arrhenian viscosity profile.*

There most common methods reported in literature to estimate the T_v are dilatometry and stress relaxation experiment.[18] In the first one, when the materials starts to flow, and thus reach the T_v, a higher thermal expansion coefficient is expected. In stress relaxation measurements, either performed *via* rheology or DMTA, T_v value is extrapolated trough experimental data using relaxation time (2) (τ*, the time required

to the stress-relaxation modulus to reach 37% or 1/e of its initial value) and viscosity, linking via Maxwell equation (3).

$$\tau^* = \tau_0 \cdot e^{\frac{E_a}{RT}} \quad (2)$$

$$\eta = G' \cdot \tau^* \quad (3)$$

The above described T_v evaluations are related to an application of external forces and to experiments performed at a temperature far above T_v. For these reasons, discrepancies were reported when comparing T_v values obtained from the two methods. A recent method, in static state, is reported by Ji et al. by doping aggregation-induced-emission (AIE) luminogens in vitrimers and following the fluorescence change as a function of temperature.[28] Elongational creep measurements[29] and creep compliance experiments[30] are also diffusely used to evaluate topology freezing transition temperature. Nevertheless, it is important to remind that T_v is a conventionally chosen and calculated temperature and not an exact temperature at which exchange reactions became active. In vitrimers, the connectivity remains constant as the temperature reaches the T_v and the network remain insoluble at all temperatures as the number of bonds remain constant.

A selection of associative covalent adaptable networks is schematized in ***Table 4.2***.

Table 4.2. List of different associative CANs.

Dynamic chemistry	*Reaction scheme*
Boronic ester exchange[31]	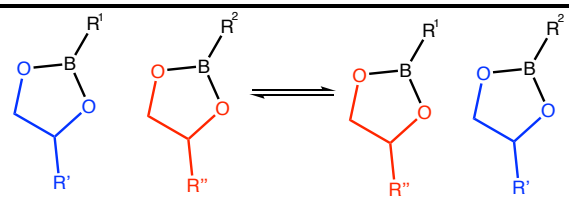
Silyl ether exchange [25]	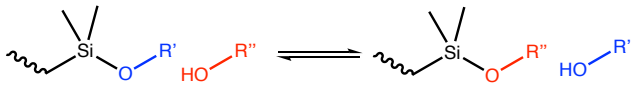
Transesterification [24]	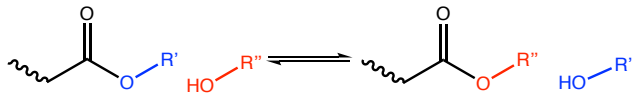
Transthioesterification[32]	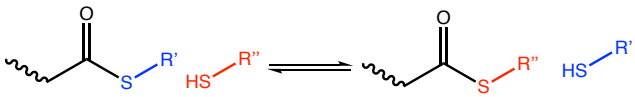
Vinylogous urethane (C), urea (N)[33]	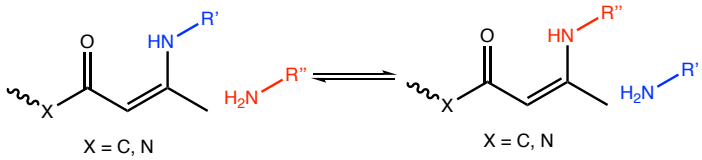
Disulfide exchange[34]	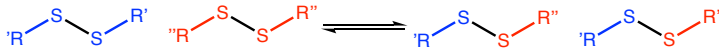

Among the several dynamic chemistries, one of the first example of catalyst-free vitrimers was introduced in Du Prez research group by Denissen et al. in 2015 and based on transamination of vinylogous urethane (VU).[26] A vinylogous urethane is a specific vinylogous acyl moiety that can be amides, urethane or urea depending on the chemical nature of the X atom next to the carbonyl functionality (C, N, O).

The synthesis of such networks starts with the transformation of an alcohol into an acetoacetate group through an acetoacetylation reaction. Further addition of primary amine reacts *via* a polycondensation reaction to form vinylogous urethane (***Figure 4.5a***). Vinylogous urethanes have the ability to form intramolecular H-bonds, that readily undergoes through exchange via transamination mechanism. The mechanism was hypothesized to occur via two pathways schematized in ***Figure 4.5b***: protic-

iminium type or aprotic-Michael type pathway depending on the matrix and temperature range of the materials.[35] The associative nature of the exchange mechanism determines that an excess of primary amines[26,36] (for example 5% mol excess as a reactive chain ends) is necessary to initiate the exchange mechanism.

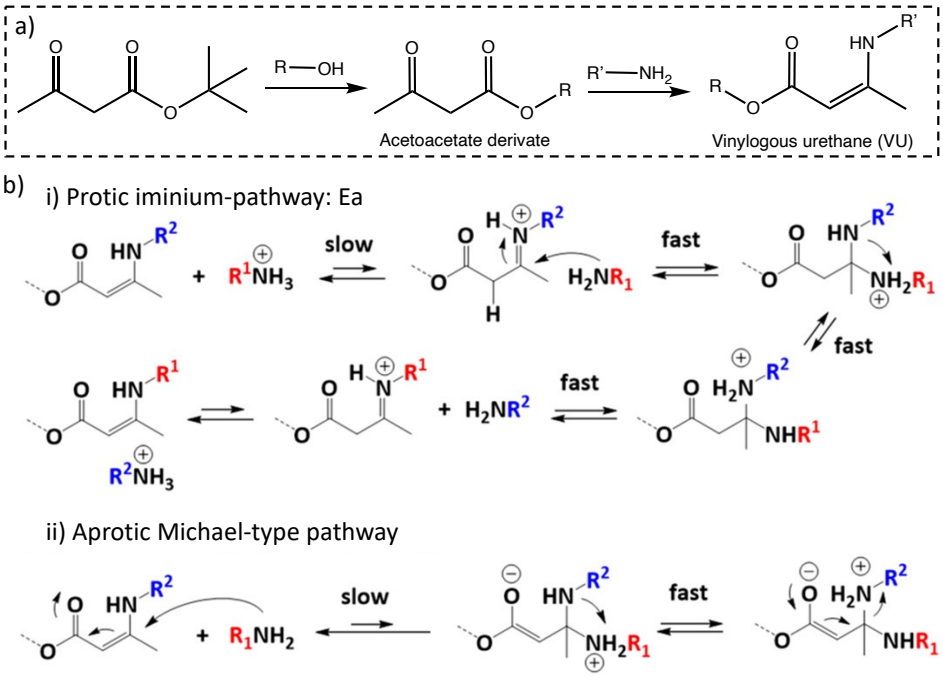

Figure 4.5. *a) Generic scheme of VU synthesis starting from acetoacetylation reaction and condensation with a primary amine, b) mechanism of VU dynamic chemistry: iminium-type or aprotic Michael-type mechanism.[35]*

It was also demonstrated that adding a small amount of TBD, pTsOH or DBTL gave remarkable effects on the resulting viscoelastic properties giving different activation energy.[37]

4.5. Application of CANs

Vitrimers have only been reported from 2011 and because of their unique properties, they are subject of interest for several industrial application.

One of the most relevant applications is the use of these materials as replacement of conventional thermoset with the ability to be reprocessed and reshaped after complete curing them. The simplest experiment is to characterize the mechanical properties of a material, cut it into small pieces, reprocess it in a mold via compression molding and retest again its mechanical properties that should not be sensibly varied.

The ability of covalent adaptable networks to rearrange their molecular structure allows them to heal and restore their mechanical properties after damage. From this aspect derive the ability to weld object together by exploiting the self-healing properties. In 2017, Nicolay, Liebler and coworkers demonstrated the possibility to weld together dioxaborolane-based vitrimers of polyethylene and polymethylmethacrylate.[31]

Another interesting and appealed application of such innovative materials is in the manufacturing of composites. So far, many thermosets are used for this purpose in different categories: fiber-reinforced, fiber of glass or cellules and carbon-fiber. Contrarily to conventional epoxy materials, vitrimers composite form strong weld that can be reformed multiple time. In a work published in 2016 by Yu et al.[38], they were able to recycle a vitrimers-based carbon fiber-reinforced composite through the use of a reactive solvent (ethylene glycol) capable to exchange with the network. After that the carbon-fiber and the monomeric component can be reused to create new composite with the same properties as the original one. Circular economy and closed-loop recycling of plastic is also reported in a recent work of Ma et al.[39], presenting a VU network synthetized from bis-polyethylene glycol acetoacetates and a tris-amine that can be degraded by water at 60°C with almost quantitative recovery of the acetoacetate monomer (~98%).

In the following two chapters will be discussed an example of a new dissociative exchange chemistry performed in the laboratory of prof. Du Prez (Chapter 5) and a potential application in Chapter 6.

References

[1] I. Vollmer, M. J. F. Jenks, M. C. P. Roelands, R. J. White, T. Harmelen, P. Wild, G. P. Laan, F. Meirer, J. T. F. Keurentjes, B. M. Weckhuysen, *Angew. Chem. Int. Ed.* **2020**, *59*, 15402.

[2] J. F. Patrick, M. J. Robb, N. R. Sottos, J. S. Moore, S. R. White, *Nature* **2016**, *540*, 363.

[3] R. Geyer, J. R. Jambeck, K. L. Law, *Sci. Adv.* **2017**, *3*, e1700782.

[4] P. Cordier, F. Tournilhac, C. Soulié-Ziakovic, L. Leibler, *Nature* **2008**, *451*, 977.

[5] S. Burattini, B. W. Greenland, D. H. Merino, W. Weng, J. Seppala, H. M. Colquhoun, W. Hayes, M. E. Mackay, I. W. Hamley, S. J. Rowan, *J. Am. Chem. Soc.* **2010**, *132*, 12051.

[6] S. D'Auria, A. M. Pourrahimi, A. Favero, P. Neuteboom, X. Xu, S. Haraguchi, M. Bek, R. Kádár, E. Dalcanale, R. Pinalli, C. Müller, J. Vachon, *Adv. Funct. Mater.* **2023**, *33*, 2301878.

[7] S. C. Grindy, R. Learsch, D. Mozhdehi, J. Cheng, D. G. Barrett, Z. Guan, P. B. Messersmith, N. Holten-Andersen, *Nat. Mater.* **2015**, *14*, 1210.

[8] C. J. Kloxin, T. F. Scott, B. J. Adzima, C. N. Bowman, *Macromolecules* **2010**, *43*, 2643.

[9] Z. Zhao, X. Mu, N. Sowan, Y. Pei, C. N. Bowman, H. Jerry Qi, D. Fang, *Soft Matter* **2015**, *11*, 6134.

[10] J. M. Winne, L. Leibler, F. E. Du Prez, *Polym. Chem.* **2019**, *10*, 6091.

[11] F. Van Lijsebetten, T. Debsharma, J. M. Winne, F. E. Du Prez, *Angew. Chem.* **2022**, *134*, e202210405.

[12] L. Zhang, S. J. Rowan, *Macromolecules* **2017**, *50*, 5051.

[13] J. M. Craven, US Pat. *2,435,003, 1969***.**

[14] H. Ying, Y. Zhang, J. Cheng, *Nat. Commun.* **2014**, *5*, 3218.

[15] D. J. Fortman, J. P. Brutman, C. J. Cramer, M. A. Hillmyer, W. R. Dichtel, *J. Am. Chem. Soc.* **2015**, *137*, 14019.

[16] M. Delahaye, J. M. Winne, F. E. Du Prez, *J. Am. Chem. Soc.* **2019**, *141*, 15277.

[17] F. Van Lijsebetten, Y. Spiesschaert, J. M. Winne, F. E. Du Prez, *J. Am. Chem. Soc.* **2021**, *143*, 15834.

[18] C. Taplan, M. Guerre, F. E. Du Prez, *J. Am. Chem. Soc.* **2021**, *143*, 9140.

[19] B. Zhang, Z. A. Digby, J. A. Flum, P. Chakma, J. M. Saul, J. L. Sparks, D. Konkolewicz, *Macromolecules* **2016**, *49*, 6871.

[20] X. Chen, M. A. Dam, K. Ono, A. Mal, H. Shen, S. R. Nutt, K. Sheran, F. Wudl, *Science* **2002**, *295*, 1698.

[21] S. Billiet, K. De Bruycker, F. Driessen, H. Goossens, V. Van Speybroeck, J. M. Winne, F. E. Du Prez, *Nat. Chem.* **2014**, *6*, 815.

[22] T. F. Scott, A. D. Schneider, W. D. Cook, C. N. Bowman, *Science* **2005**, *308*, 1615.

[23] R. Nicolaÿ, J. Kamada, A. Van Wassen, K. Matyjaszewski, *Macromolecules* **2010**, *43*, 4355.

[24] D. Montarnal, M. Capelot, F. Tournilhac, L. Leibler, *Science* **2011**, *334*, 965.

[25] Y. Nishimura, J. Chung, H. Muradyan, Z. Guan, *J. Am. Chem. Soc.* **2017**, *139*, 14881.

[26] W. Denissen, G. Rivero, R. Nicolaÿ, L. Leibler, J. M. Winne, F. E. Du Prez, *Adv. Funct. Mater.* **2015**, *25*, 2451.

[27] M. Capelot, M. M. Unterlass, F. Tournilhac, L. Leibler, *ACS Macro Lett.* **2012**, *1*, 789.
[28] Y. Yang, S. Zhang, X. Zhang, L. Gao, Y. Wei, Y. Ji, *Nat. Commun.* **2019**, *10*, 3165.
[29] S. Kaiser, P. Novak, M. Giebler, M. Gschwandl, P. Novak, G. Pilz, M. Morak, S. Schlögl, *Polymer* **2020**, *204*, 122804.
[30] R. H. Pritchard, A.-L. Redmann, Z. Pei, Y. Ji, E. M. Terentjev, *Polymer* **2016**, *95*, 45.
[31] M. Röttger, T. Domenech, R. Van Der Weegen, A. Breuillac, R. Nicolaÿ, L. Leibler, *Science* **2017**, *356*, 62.
[32] C. Wang, S. Mavila, B. T. Worrell, W. Xi, T. M. Goldman, C. N. Bowman, *ACS Macro Lett.* **2018**, *7*, 1312.
[33] W. Denissen, I. De Baere, W. Van Paepegem, L. Leibler, J. Winne, F. E. Du Prez, *Macromolecules* **2018**, *51*, 2054.
[34] A. Rekondo, R. Martin, A. Ruiz De Luzuriaga, G. Cabañero, H. J. Grande, I. Odriozola, *Mater. Horiz.* **2014**, *1*, 237.
[35] Y. Spiesschaert, C. Taplan, L. Stricker, M. Guerre, J. M. Winne, F. E. Du Prez, *Polym. Chem.* **2020**, *11*, 5377.
[36] M. Guerre, C. Taplan, R. Nicolaÿ, J. M. Winne, F. E. Du Prez, *J. Am. Chem. Soc.* **2018**, *140*, 13272.
[37] W. Denissen, M. Droesbeke, R. Nicolaÿ, L. Leibler, J. M. Winne, F. E. Du Prez, *Nat. Commun.* **2017**, *8*, 14857.
[38] K. Yu, Q. Shi, M. L. Dunn, T. Wang, H. J. Qi, *Adv. Funct. Mater.* **2016**, *26*, 6098.
[39] Y. Ma, X. Jiang, Z. Shi, J. A. Berrocal, C. Weder, *Angew. Chem. Int. Ed.* **2023**, *62*, e202306188.

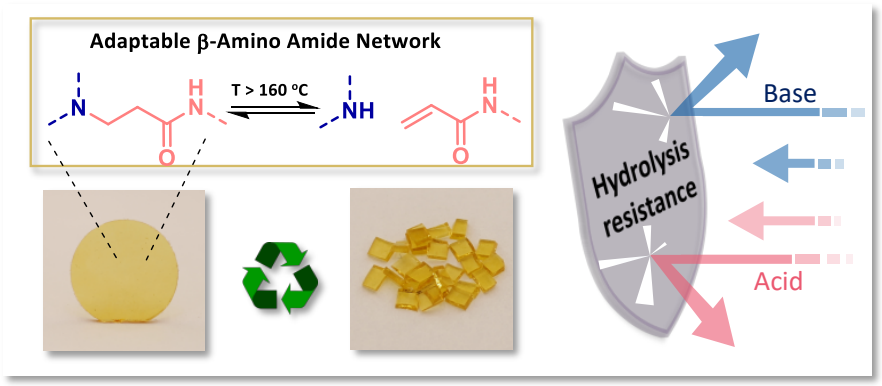

Abstract: Herein, we report a scalable synthesis of catalyst-free, covalent adaptable networks (CANs) based on β-amino amides as dynamic linkages. Rheological analysis of their dynamic behaviour shows a remarkably high activation energy of around 300 kJ mol^{-1}. Hence, the obtained elastomers can be (re-)processed at elevated temperatures while possessing high creep resistance in a wide temperature window. Finally, in comparison with the much-studied β-amino ester-based networks, this new generation of CANs incorporating amino amide motifs possess superior hydrolytic resistance under both acidic and basic conditions.

Adapted from: L. T. Nguyen T. L., F. Portone, F.E. Du Prez, *Polym. Chem*. **2024**, 15, 11.

The work of this chapter was done in the group of Prof. Du Prez at Ghent University.

Chapter 5

β-Amino Amide Based Covalent Adaptable Networks with High Dimensional Stability

5.1. *Introduction*

The dramatic increase of plastic pollution has become one of the greatest environmental challenges.[1-3] While thermoplastic materials are intrinsically (re-)processable at elevated temperatures, repurposing or recycling the more dimensionally stable thermoset materials, in which polymer chains are covalently crosslinked, is far more cumbersome. Therefore, thermosets typically end up as permanent waste after single use.[4-6] Covalent adaptable networks (CANs) combine the high performance of thermosets and (re)processability of thermoplastics in one single material.[7-9] Although CANs are also crosslinked by covalent bonds, the dynamic nature of such bonds provides such materials with the ability to flow with the application of specific stimuli.[10-14] On the other hand, the reversible linkages within CANs often reduce their dimensional stability and creep is thus observed due to the unfavoured premature exchange at use conditions.[15-16] Suppressing this unwanted deformation at use temperatures therefore remains one of the important challenges to merge academic research on CANs and industrial applications.[17-23] Among the different approaches that have been introduced recently to limit undesired exchange (e.g., protected catalysts, modifying reactive functional groups, etc.), the use of highly endothermic retro-chemistry is one of the strategies showing the greatest potential.[24-30] Indeed, by introducing dynamic covalent chemistries that are characterized by a highly endothermic dissociation, the exchange activation energy increases, thereby shifting the exchange away from the application conditions. Hence, an appropriate balance between (re)processability and dimensional stability should be aimed for.[15-16, 31]

Recently, Du Prez research group introduced β-amino ester chemistry in the context of dynamic networks.[32] In this pioneering study, CANs were prepared from a large range of acrylate and amine building blocks via aza-Michael addition, in which bonds can exchange without adding an external catalyst, i.e. following an associative or/and a dissociative pathway *via* transesterification in the presence of hydroxyl groups and retro-Michael reactions, respectively (**Figure 5.1**).

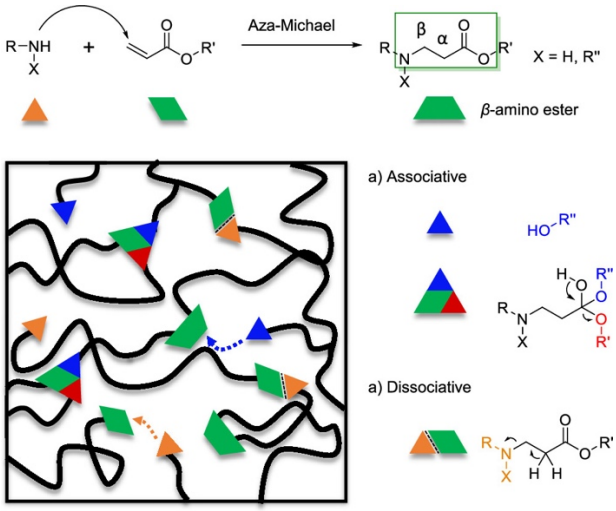

Figure 5.1. *Scheme of β-amino ester synthesis (top) and representation of the reversible aza-Michael addition either associative or dissociative covalent dynamic network.*

Subsequently, numerous studies focusing on applying this promising dynamic chemistry platform have been conducted very recently in an effort to fasten the exchange process and thus reduce the stress relaxation time, for example by modifying substituents or employing other neighbouring groups.[33-38] On the other hand, polymeric materials including β-amino esters are containing hydrolysable esters and have therefore often been investigated for their degradability.[39-42]

While previous research focused on β-amino esters,[32-33, 35, 37] this study will focus on β-amino amides as dynamic moiety in CANs. (**Scheme 5.1**).

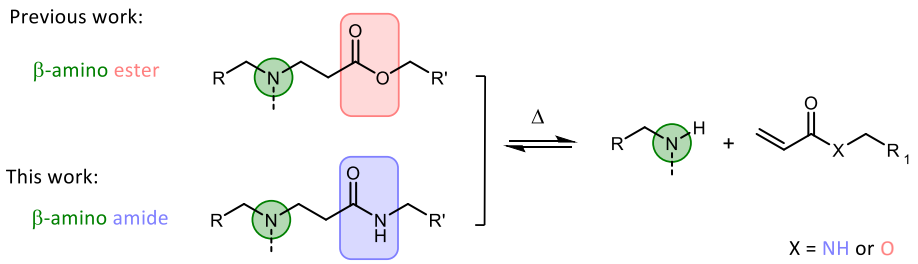

Scheme 5.1. Scheme of the previously reported β-amino ester and β-amino amide treated in this chapter.

It can therefore be expected that the hydrolytic resistance of the corresponding CANs will be limited to specific matrices and conditions. Therefore, the aim in this study is to replace the ester groups by much more stable amides and thus to develop and investigate β-amino amide-based CANs. Herein, such CANs were hypothesized to possess a substantial higher activation energy resulting in both a very high creep resistance and hydrolytic stability while still being (re)processable, in turn bringing them close to real-life applications.

5.2. *Results and discussion*

To investigate the reversibility of a β-amino amide moiety, a model compound was first prepared *via* the aza-Michael addition between readily available *N*-isopropylacrylamide and *N*-methyl butylamine with the formation of the desired *β*-amino amide compound **1,** characterized via ^{1}H NMR (see Figure 6.A1 in the appendix). This was dissolved in different NMR tubes in DMSO-d_6 and placed in separate oil baths heated at 180 °C, 160 °C, 140 °C and 120 °C. ^{1}H NMR spectra were collected before and after heating for 16 h in order to determine the thermal activated dissociation of such dynamic β-amino amide (**Figure 5.2**).

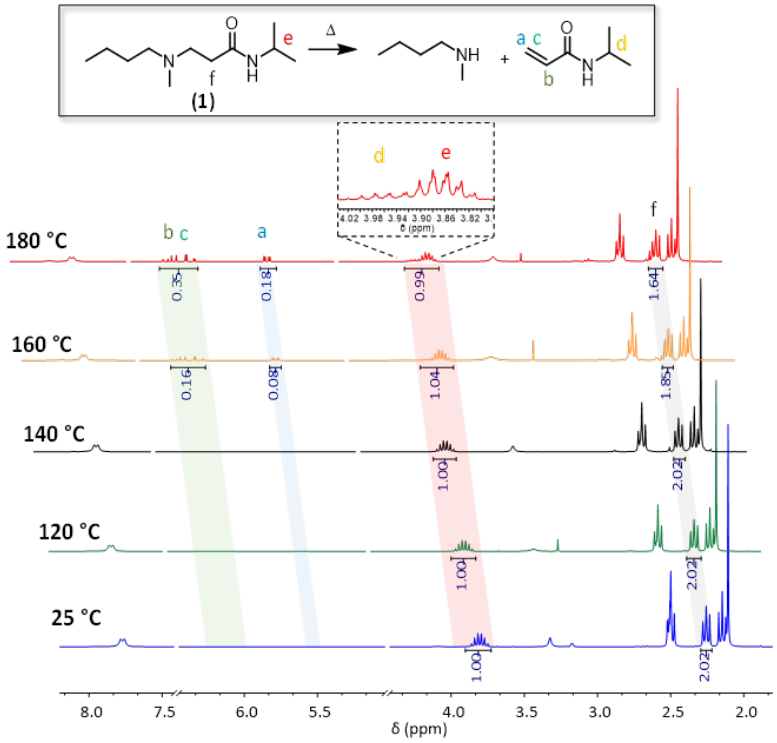

Figure 5.2. *^{1}H NMR stacking spectra of model compound **1** in DMSO-d_6 at 25 °C, 120 °C, 140 °C, 160 °C and 180 °C for 16 h.*

Up to temperatures of 140 °C, there was no significant variation compared to the NMR analysis of the pure model compound **1**. In contrast, at 160 °C, an 8% enhancement of the proton signals in the area between 6.24 ppm and 5.51 ppm is clearly visible, indicating the formation of the acrylamide double bonds via the retro-aza-Michael reaction. In addition, the decreasing intensity of proton f relative to Michael adduct **1,** as well as the appearance of proton d at 3.98 ppm, confirmed the dissociation. Finally, the increase of the double bond integral value at 180 °C (signals a to c) indicates a faster dissociation at higher temperature. All these observations confirm the reversibility of the aza-Michael reaction on β-amino amides at temperatures beyond 160 °C.

Generally, when investigating suitable chemistry for CANs, the scalability of the synthesis pathways should also be considered as a function of the envisaged bulk scale application areas. Due to the lack of cheap, large-scale available multifunctional acrylamide cross-linkers and the tedious synthesis of acrylamides in general, which

typically requires chromatographical purification,[43-44] the direct synthesis of *β*-amino amide networks *via* aza-Michael addition is not suitable for large-scale synthesis. Therefore, we focused on an earlier reported procedure[45] in which similar crosslinked materials were made in two steps, i.e. the preparation of amino-ester crosslinkers, and then the subsequent amidation reaction with various available amine-containing building blocks (*vide infra*). Hence, to comprehensively investigate the temperature-dependent nature of the aza-Michael addition and the subsequent amidation reaction, model β-amino-amide compound **2** was prepared by a one-pot reaction between the bulk chemicals methyl acrylate and 2-ethyl hexylamine (**Scheme 5.2**).

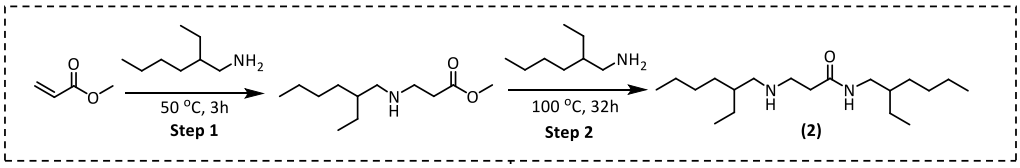

Scheme 5.2 *Synthesis of model compound **2**.*

The reaction was monitored by performing online attenuated total reflection Fourier transform infrared (ATR-FTIR) experiment at two temperatures: firstly at 50 °C for the aza-Michael addition and then at 100 °C for the amidation step. In the first step, the progressive disappearance of the C=C stretching at 986 cm^{-1} and the analogue increasing of the C-N stretching band at 1125 cm^{-1} were observed (**Figure 5.3a** top), indicating that the reaction completed after 2 h (**Figure 5.3a** bottom).

The Michael-adduct structure was confirmed by ^{1}H NMR (see **Figure 5.A2**), which showed complete consumption of the methyl acrylate. Next, the amidation step was evaluated using the same technique but increasing the temperature to 100 °C. In this stage, the focus shifted to the stretching band at 1740 cm^{-1} related to the ester carbonyl moiety, which decreased over time, and to the steady increase of the corresponding carbonyl of the amide bond at 1666 cm^{-1}. At the same time, the bending related to the amide N-H bond at 1540 cm^{-1} also supported the conversion of esters to amides (**Figure 5.3b** top). The observed FTIR signals reached a plateau after 30 h as depicted in **Figure 5.3b** (bottom), indicating the full conversion of the amino ester to the amino amide functionality.

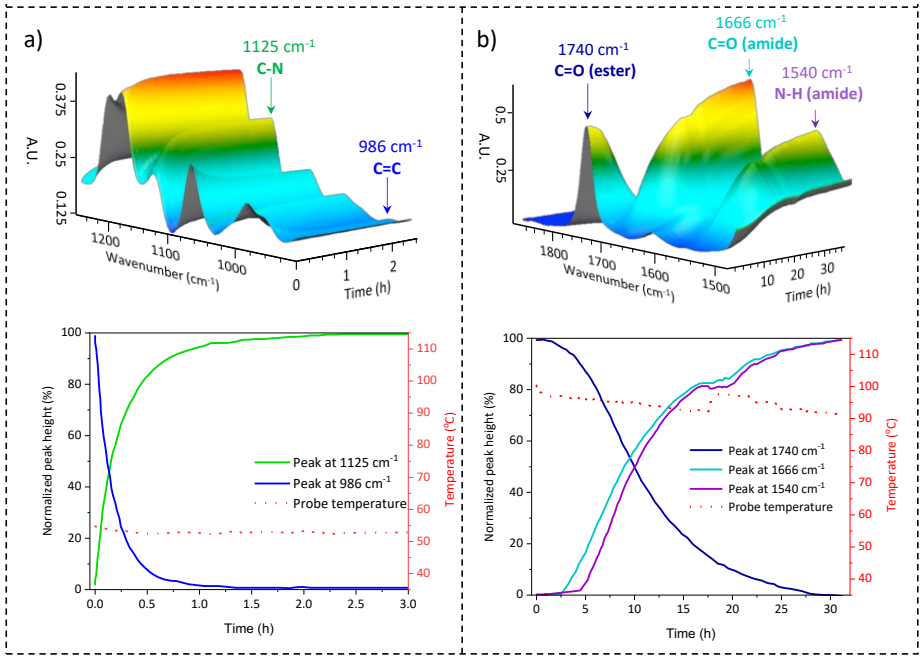

Figure 5.3. *a) top: three-dimensional plot of time resolved ATR-FTIR in the region of 1200 cm-1 to 900 cm-1 for the aza-Michael addition step, bottom: plot of the intensity related to the followed peaks versus time. b) top: three-dimensional plot of time resolved ATR-FTIR in the region of 1800 cm-1 to 1300 cm-1 for the amidation reaction, bottom: plot of the intensity related to the followed peak versus time.*

This conclusion was further confirmed by ^{1}H NMR as depicted in **Figure 5.A3** (see appendix). Based on these initial results, as well as those previously reported in the literature,[45] we concluded that in the reaction at 50 °C between an acrylate ester and the amino derivate, the aza-Michael addition is the only reaction observed resulting in β-amino esters, which subsequently undergo amidation at 100 °C with the formation of β-amino amides.

In view of scalability, several covalent adaptable β-amino amide networks (BAA) were prepared by reacting a tetrafunctional cross-linker with β-amino ester moieties, obtained through a straightforward aza-Michael addition and characterized via ^{1}H NMR (**Figure 5.A4**), and subsequently crosslinked with a series of readily available amino-containing building blocks (**Scheme 5.3**). The reference network was prepared with Pripol 2033 diacrylate, previously synthetized starting from the

corresponding alcohol with acryloyl chloride and characterized via ^{1}H NMR (**Figure 5.A5**).

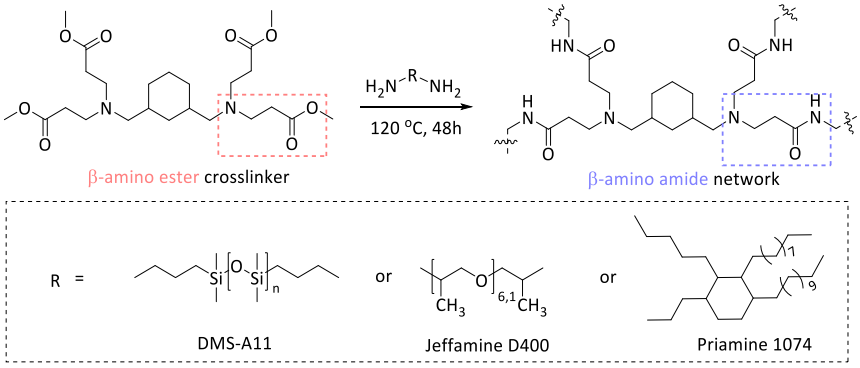

Scheme 5.3. *Preparation of β-amino amide containing CANs from a tetrafunctional crosslinker and Priamine 1074 (BAA-P), Jeffamine D400 (BAA-J) or DMS-A11 (BAA-S).*

The cross-linking process was followed by ATR-FTIR, in which the disappearance of absorption bands of the ester-carbonyl groups (at 1720 cm^{-1}) was simultaneously observed with the increase of the amide-carbonyl absorbance band at 1665 cm^{-1}, indicating the amidation of the ester to form the targeted amide bonds (**Figure 5.4**).

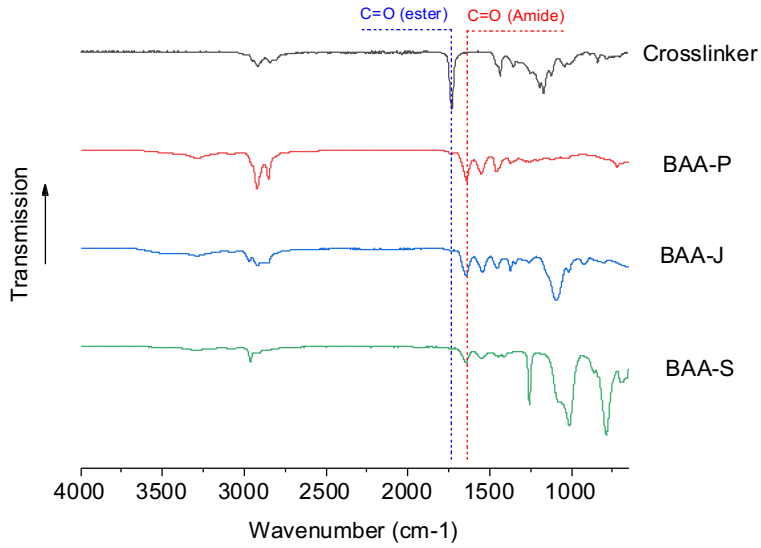

Figure 5.4. *ATR-FTIR of amino ester crosslinker (I) and resulting amino amide networks.*

The overall properties of the obtained materials have been summarized in **Table 5.1**. Although BAA-J and BAA-S showed soluble fractions above 10%, associated with a very high swelling ratio (> 580%), BAA-P showed a low soluble fraction (6.3%) with a swelling ratio of 350% in THF. Moreover, a wide range of glass transition temperatures (T_g) from -107 to -15 °C were obtained when using different amine building blocks, which affect both the backbone mobility and cross-link density. In addition, thermogravimetric analysis (TGA) displayed a high degradation onset temperature ($T_{d5\%}$) ranging between 298 and 325 °C with no significant mass loss (< 3.5%) after a period of 2 h at 200 °C under air atmosphere, revealing sufficient stability for the thermal (re-)processing.

***Table 5.1**. Overall properties of the synthesized β-amino amide CANs with a range of amines.*

Network	Amine	Swelling ratio (%)[a]	Soluble fraction (%)[a]	T_{gDSC} (°C)[b]	$T_{d5\%}$ (°C)[c]	$m_{iso\ 200\text{-}2h}$ (%)[d]	G′[e] (MPa)
BAA-P	Priamine	350 ± 23	6.3 ± 0.7	-15	325	3.0	2.29
BAA-J	Jeffamine	590 ± 26	17.3 ± 3.2	-25	298	3.5	0.43
BAA-S	PDMS A11	582 ± 17	13.8 ± 1.5	-107	320	3.0	0.33
BAA-P R3	Priamine	292 ± 19	3.3 ± 1.1	-7	326	-	-
BAE-P (Ref)	-	340 ± 16	4.8 ± 2.2	-43	336	1.5	-

[a] Swelling ratio and soluble fraction obtained from a four-sample measurement in THF at RT for 24 h. [b] Determined during the second heating run by DSC with a heating and cooling rate of 10 K·min^{-1}. [c] Determined as onset temperature for 5% mass loss observed by TGA using a heating rate of 10 K·min^{-1}. [d] Determined mass loss observed by TGA isothermal mode at 200 °C for 2 h. [e] Apparent plateau storage modulus determined from frequency sweep measurements at 100 °C and 1 rad·s^{-1}.

The dynamicity of the selected BAA-P was further examined by rheology with stress relaxation experiments in a temperature range between 200 and 170 °C. A drop in the material's shear storage modulus (G') upon increasing the temperature was clearly observed in non-normalized stress relaxation curves (**Figure 5.5**), which revealed the decrease in crosslink density.

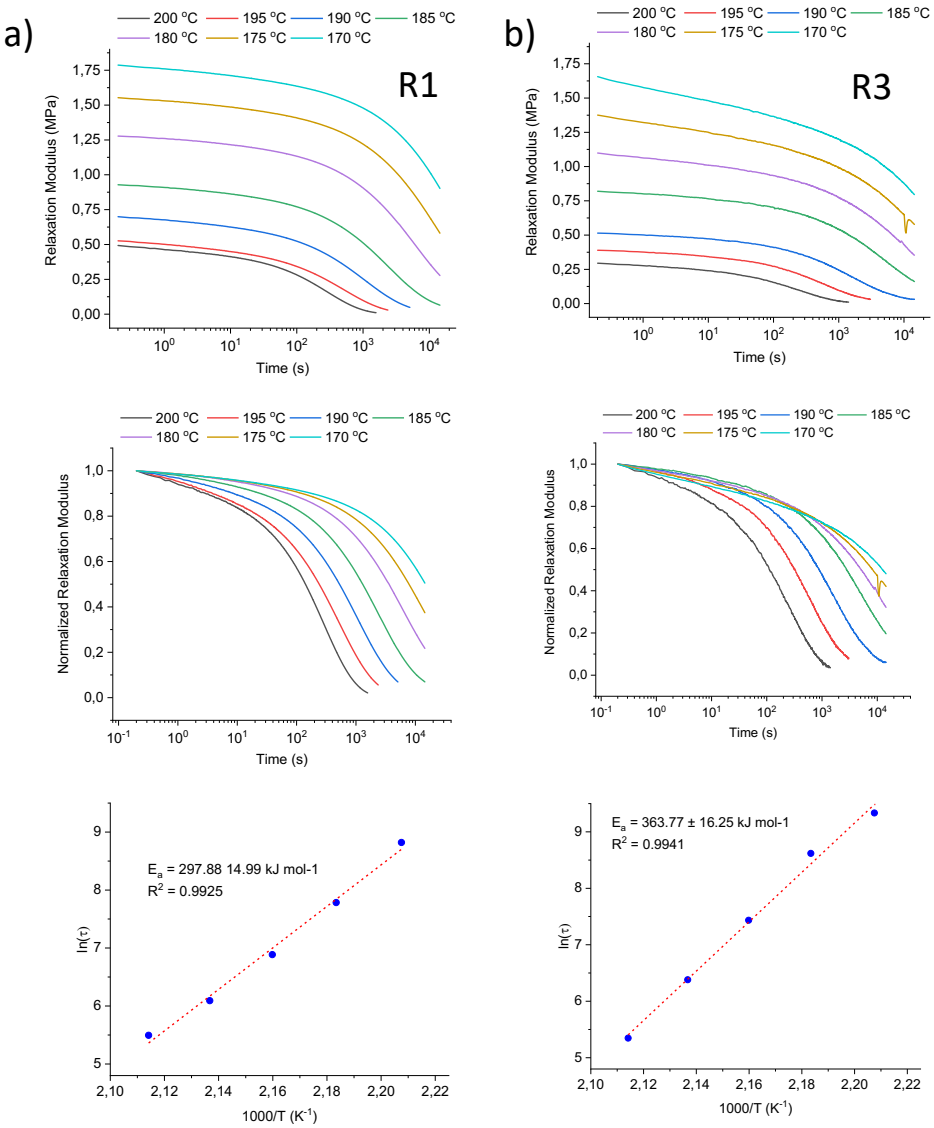

Figure 5.5. *From top to bottom are non-normalized, normalized stress relaxation cures and derived Arrhenius plots of BAA-P after the first (a) and the third (b) reprocessing cycle.*

Indeed, a frequency sweep experiment confirmed the partial de-crosslinking by showing a drop in G' with higher temperatures, which is another indication for a dissociative exchange of the dynamic amino-amide via reversible (retro) aza-Michael reaction (**Figure 5.6**).

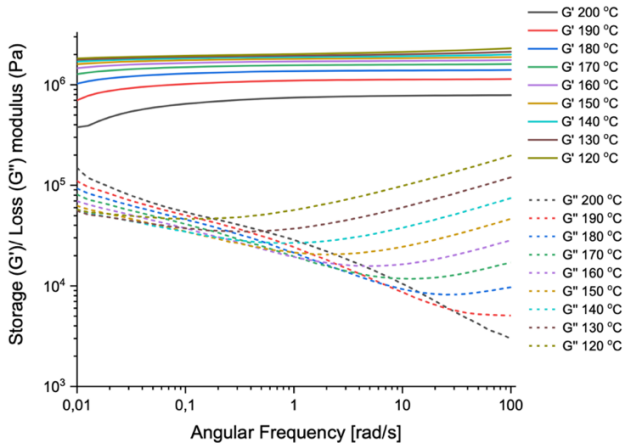

Figure 5.6. *Frequency sweep measurements of BAA-P from 200 to 120 °C, indicating a decrease in elastic plateau modulus with temperature.*

In addition, the elastic plateau modulus in frequency sweep experiments remained almost unchanged for temperatures below 150 °C, yet significantly dropped beyond 160 ˚C revealing the contribution of the dynamic Michael adduct dissociation beyond that temperature. In **Figure 5.7a**, the normalized stress relaxation curves of BAA-P (solid line) are reported in comparison to the corresponding β-amino ester network BAE-P (dashed line).

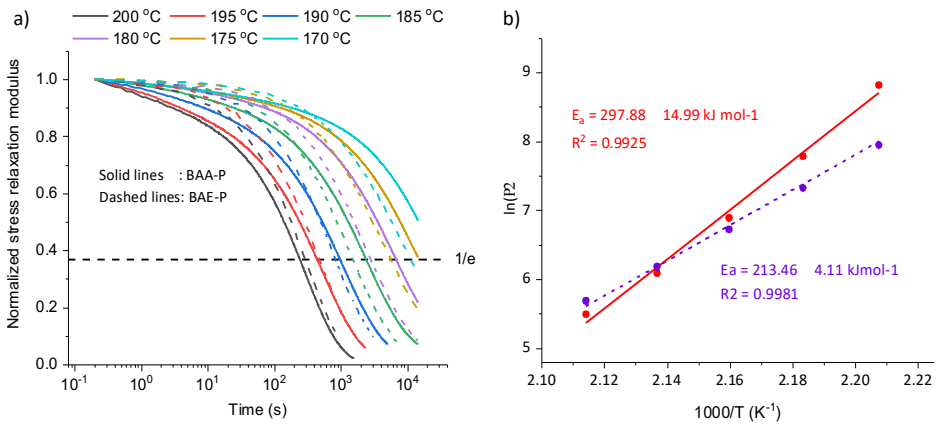

Figure 5.7. *Normalized stress relaxation curves (a) and corresponding Arrhenius plots (b) of BAA-P (red) and BAE-P (violet) networks.*

A high-temperature dependent dynamic behaviour was observed in which the applied stress could be relaxed completely at elevated temperatures, favouring the (re)processability with relaxation times around 4 min at 200 °C. In addition, an

Arrhenius plot extracted from the characteristic stress relaxation time (τ) was used to derive a high activation energy of 298 kJ mol^{-1}, compared to the value of 213 kJ mol^{-1} found for BAE-P (**Figure 5.7b**).

Although TGA revealed a degradation onset temperature ($T_{d5\%}$) of 325°C, time sweep experiments at different temperatures showed a slight increase in storage modulus at temperature above 200 °C (200-260 °C), which could be ascribed to the introduction of permanent cross-links as a result of a photopolymerization of the acrylamide groups created at dissociation stage (**Figure 5.8**).

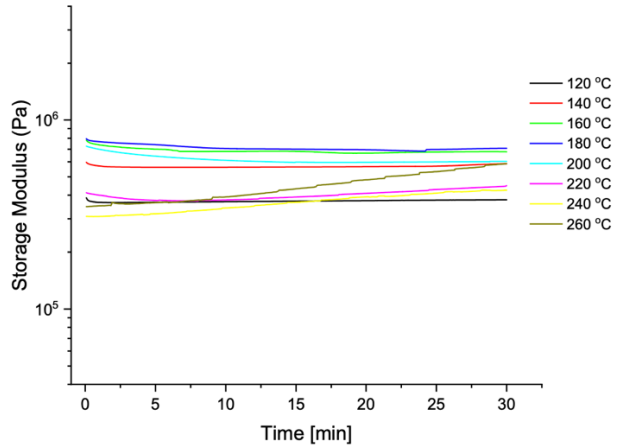

Figure 5.8. *Time sweep experiments of BAA-P results indicating the increase in storage modulus beyond 200 °C.*

For that reason, (re)processing experiments have all been conducted at 180 °C. To demonstrate the (re)processability, BAA-P was cut into small pieces and pressed multiple times by compression moulding at 180 °C under 3 tons for 60 min.

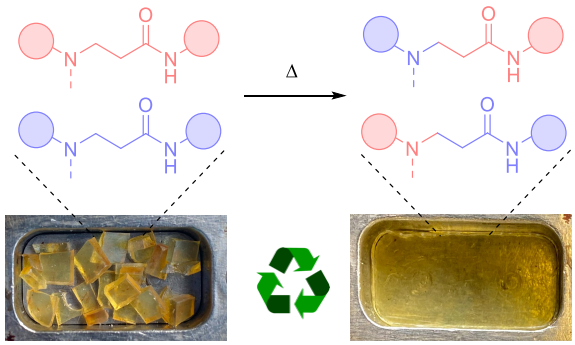

Figure 5.9. *(Re)processing demonstration of BAA-P.*

The reprocessing ability of materials with dynamic amino-amide linkages was demonstrated by executing 3 cycles without observing significant change in appearance or thermal properties (**Figure 5.9**, **Table 5.1** entry BAA-P R3).

Although the stress relaxation of the third recycled sample slightly slowed down (**Figure 5.5** bottom), the chemical structure observed by FTIR remained unchanged during the recycling processes (**Figure 5.10**).

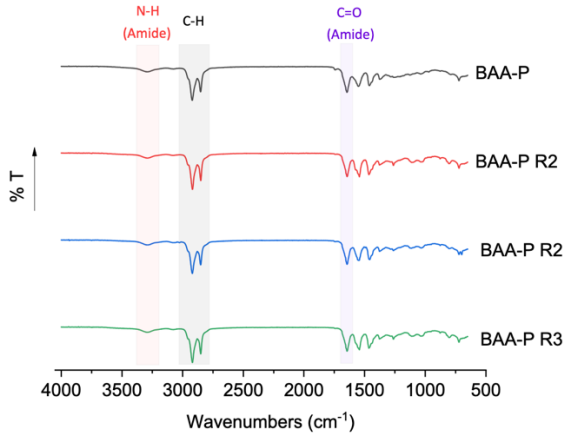

Figure 5.10. *IR spectrum of the initial BAA-P network and after 1 to 3 cycles of (re)compression molding (top to bottom).*

In addition, tensile test results revealed no significant change in mechanical properties after 3 cycles of remolding (**Figure 5.11**).

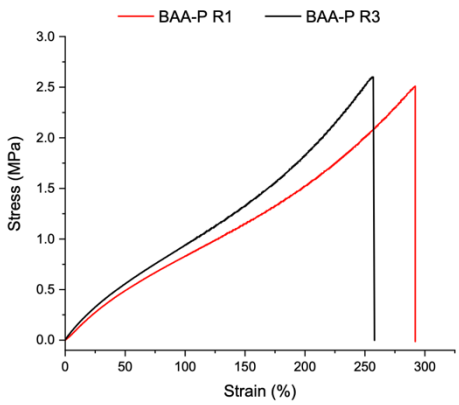

Sample	Ultimate stress (MPa)	Total elongation (%)	Modulus (MPa)
BAA-P R1	2.40 ± 0.45	279 ± 27	1.19 ± 0.16
BAA-P R3	2.62 ± 0.42	261 ± 21	1.41 ± 0.13

Figure 5.11. *Stress-strain curves (graph) and corresponding tensile test results (table) of BAA-P network after the first (BAA-P R1, red) and the third (BAA-P R3, black) remolding cycle.*

Finally, in order to investigate the dimensional stability, a creep recovery experiment was carried out on BAA-P by applying 2 kPa shear stress for 5000 s, followed by a recovery period of 3600 s at temperatures ranging from 50 to 110 °C (**Figure 5.12**).

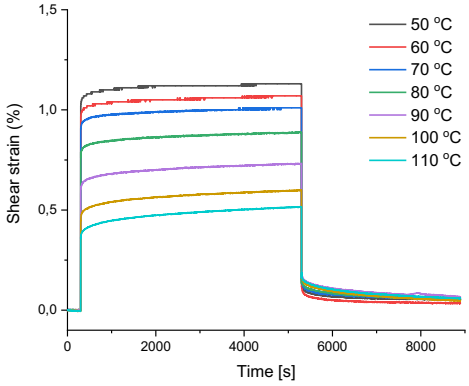

Temperature (°C)	Creep rate ε (%.s)	Remaining strain (%)
50	7,88E-19	0,05
60	1,08 x 10^{-6}	0,03
70	1,66 x 10^{-6}	0,05
80	4,90 x 10^{-6}	0,05
90	6,14 x 10^{-6}	0,06
100	8,52 x 10^{-6}	0,05
110	9,57 x 10^{-6}	0,06

Figure 5.12. *Creep recovery (graph), corresponding creep rates and remaining strain after recovery (table) of BAA-P.*

Despite the low T_g of BAA-P (-15 °C), high creep resistance was observed and the creep rates were below 10^{-5} % s^{-1} up to 100 °C with remaining strains less than 0.05% after one hour recovery. Also, as mentioned earlier, the use of amides instead of esters was expected to improve the chemical stability of the obtained materials. Therefore, hydrolysis tests of BAA-P were carried out up to 12 days in 4 different

conditions: deionized water, HCl 1M, NaOH 1M at room temperature and in deionized water at 100 °C. All results depicted in **Table 5.2** indicate soluble fractions of less than 1% while the network maintained its structural integrity (**Figure 5.13a** and **Figure 5.13b**).

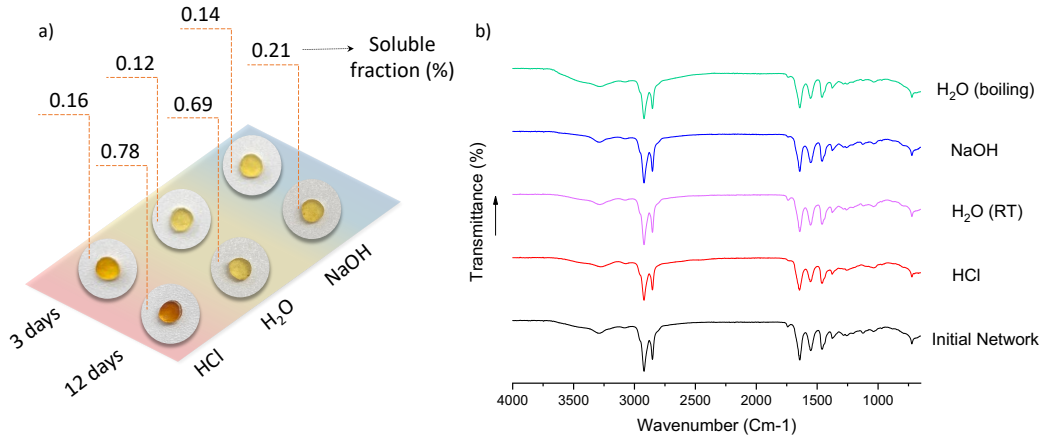

Figure 5.13. *a) Appearances and corresponding soluble fractions of BAA-P samples after the hydrolysis tests in different conditions (HCl 1 M, deionized water, NaOH 1 M). b) ATR-IR spectra of initial BAAP-P network and after hydrolysis tests in 1 M HCl, deionized water (room temperature), 1 M NaOH and boiling water (bottom to top, respectively).*

In comparison to the β-amino ester network (Table 1-BAE-P), an overall high hydrolytic resistance was observed for the β-amino amide network.

Indeed, BAA-P remained almost unchanged after two days in boiling water whereas BAE-P lost its structural appearance in comparable conditions (**Figure 5.14**).

Table 5.2*. Overview of hydrolysis tests of BAA-P under different conditions.*

Condition	**Time (days)**	***Swelling ratio***	***Soluble Fraction***
Water (RT)	3	4.5 ± 1.9	0.69 ± 0.12
	12	9.2 ± 3.64	0.12 ± 0.07
HCl 1M	3	25.7 ± 2.8	0.06 ± 0.01
	12	22.9 ± 5.7	0.78 ± 0.70
NaOH 1M	3	3.8 ± 1.83	0.21 ± 1.29
	12	6.2 ± 0.82	0.14 ± 0.15
Water (100 °C)	2	-	0.26 ± 0.16

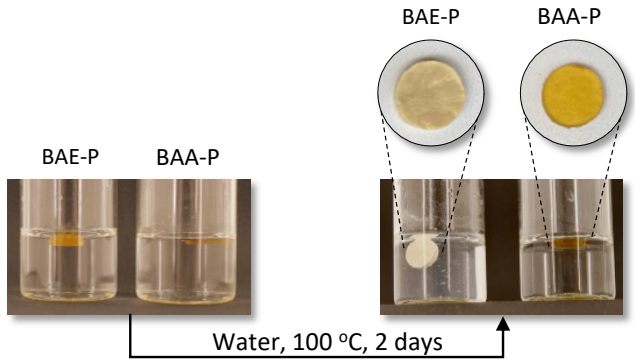

Figure 5.14. *Appearances of amino ester network (BAE-P) and amino amide network (BAA-P) before (left) and after (right) hydrolysis test in boiling water for 2 days, illustrating the structural loss of BAE-P and the almost unchanged structure of BAA-P.*

These results indicate the potential dimensional resistance of such covalent adaptable amino-amide networks in harsh conditions (e.g., marine applications).

5.3. *Conclusions*

In this study, the temperature-dependent reaction between acrylates and amines was first investigated by model studies, in which the aza-Michael addition was exclusively observed at 50 °C, whereas the subsequent amidation (converting esters into amides) efficiently proceeded at 100 °C. Additionally, the dissociation of the resulting dynamic β-amino amide bonds was found to occur at temperatures beyond 160 °C. By exploiting this knowledge, a scalable synthesis of covalent adaptable amino-amide networks using a multifunctional amino-ester cross-linker and various bifunctional amine-containing building blocks was performed. The obtained amino-amide networks showed high thermal stability while rheological measurements revealed a temperature-dependent stress relaxation with high activation energy of around 300 kJ mol^{-1}, as well as the ability of the networks to be (re)processed multiple times without significant changes in properties. Moreover, the presented materials showed an excellent dimensional stability with less than 0.05% of the remaining strain as observed in creep measurements at 100 °C. Finally, in comparison to the corresponding β-amino ester-based material, the CANs also presented exceptional hydrolytic stability in acidic, basic and neutral conditions for at least 12 days.

Acknowledgements

Special thanks to Prof. Filip Du Prez and all his group, in particular Loc Tan Nguyen and Bernhard De Meyer from University of Ghent.

5.4. *Experimental section*

Materials and methods

All materials i.e. *N*-Methylbutylamine (98%, Sigma-Aldrich), *N*-isopropylacrylamide (>99%, TCI Chemicals Europe), 2-ethyl-1-hexylamine (98%, Sigma-Aldrich), 1,3-cyclohexanebis(methylamine) (98%, Sigma-Aldrich), 2-ethyl-1-hexylamine (98%, Sigma-Aldrich), methyl acrylate (>99%, TCI Chemicals Europe), acryloyl chloride (96%, stabilized with phenothiazine, ABCR), triethylamine (>99%, Sigma-Aldrich), aminopropyl-terminated polydimethylsiloxanes, DMS A11 (Gelest Inc), methanol (MeOH, >99.8%, Fisher Chemical), tetrahydrofuran (THF, >99.8%, Acros Organics), Jeffamine D400 kindly provided by Huntsman, Priamine 1074 and Pripol 1033, kindly provided by Croda, were used without further purification unless stated otherwise.

Nuclear magnetic resonance (NMR) spectra were recorded on a Bruker Advance Ultrashield 300 MHz spectrometer. Deuterated chloroform (CDCl3) or deuterated DMSO-d6 was used as solvent. Chemical shifts are given in parts per million (ppm).

Online infrared (IR) spectroscopy. Were recorded using a MettlerToledo ReactIR 702L with TE MCT detector (Thermoelectrically Cooled Mercury Cadmium Telluride detector). The probe interface was an AgX 6 mm × 1.5 m Fiber (Silver Halide) with a DiComp (Diamond) probe tip. The recorded wavelength range was between 4500 cm−1 to 600 cm−1.

Attenuated total reflection Fourier transform infrared spectroscopy (ATR-FTIR) spectra were measured using a Perkin-Elmer Spectrum1000 FTIR infrared spectrometer with a diamond ATR probe.

Thermogravimetric analyses (TGA) were performed with a Mettler Toledo TGA/SDTA851e instrument under air atmosphere at a heating rate of 10 K·min−1 from 25 to 800 °C for the dynamic mode or at 200 °C for 2 h for the isothermal measurement.

Differential scanning calorimetry (DSC) analyses were performed with a Mettler Toledo instrument 1/700 under air atmosphere at a heating rate of 10 K·min−1 from −100 to 100 °C.

Rheology experiments were performed on an Anton Paar MCR 302. The experiments were performed in parallel plate geometry using 8 mm sample disks. Amplitude

sweep experiments were performed using a frequency of 1 Hz, a constant force of 1 N, and a variable shear strain that was ramped up logarithmically from 0.01% to 10% to observe the linear viscoelastic region. Stress-relaxation experiments were performed at different temperatures (200 - 170 °C, with intervals of 10 °C) using a constant shear strain within the linear viscoelastic region of the samples, and a constant force of 1 N. The obtained characteristic relaxation time (τ*) was used to calculate the activation energy.

Creep experiments at different temperatures (50 - 110 °C, with intervals of 10 °C) were performed using a constant force of 1 N. Additionally, in the first 300 s, no shear stress was applied. Subsequently, a 2000 Pa shear stress was applied for 5000 s followed by a recovery period for 3600 s in which the shear strain was monitored. Creep measurements were preceded by a time sweep measurement at 90 °C and a fixed frequency of 1 Hz for 1 h to remove possible thermal history.

Time sweep experiment was performed in parallel plate geometry using 8 mm sample disk with an applied strain of 1% and a frequency of 1 Hz for a duration of 30 min at different temperatures. Storage modulus (G') and loss modulus (G") were recorded over time.

(Re)processability was investigated by cutting the crosslinked material into pieces of about 1 cm, which were then placed into a rectangular mold for compression molding. This assembly was placed in a preheated compression press (180 °C) for 1 min under 0.5 metric tons of pressure. Then the pressure was increased to 3 tons and kept constant for an additional 60 min. After 60 min of pressing, the sample was carefully removed from the mold.

Solubility tests were carried out in vials with samples of 2 mm in diameter, 2 mm in thickness, and a weight of around 15-20 mg, to which 40 mL of THF was added. Those tests were performed for 24 h at 25 °C in THF. The solvent was then removed, and the samples were dried under vacuum overnight at 60 °C. The soluble fraction and swelling ratio were calculated using equation 1 and equation 2, respectively.

$$\text{soluble fraction (\%)} = \frac{m_i - m_d}{m_i} \qquad \text{(eq. 1)}$$

$$\text{swelling ratio (\%)} = \frac{m_s - m_i}{m_i} \qquad \text{(eq. 2)}$$

with m_i, m_s, and m_d representing the mass of initial, swollen, and dry samples, respectively.

Hydrolysis tests were conducted by introducing samples of around 20 mg into 20 mL of demineralized water or 1 M HCl or 1 M NaOH solution. A hydrolysis test at elevated temperatures was performed by placing a piece of sample (approximately 70 mg) in a glass vial with 10 mL of demineralized water, which was closed with a silicone septum. Thereafter, the vial was placed in a heated oil bath at 110 °C for the hydrolysis test in boiling water. For all the above-mentioned tests, solvent was removed after the experiment and the samples were dried under vacuum for 24 h at 100 °C until complete dryness. The soluble fraction and swelling ratio were calculated as using equation 1 and equation 2, respectively.

Model compound 3-(butyl(methyl)amino)-N-isopropylpropanamide (1)

N-isoproprylacrylamide (1 eq.) and N-methyl butylamine (1.2 eq.) were mixed and heated at 75 °C for 24 h. The residual N-methyl butylamine was removed under vacuum resulting in a transparent oil (~ quantitative yield).

^{1}H-NMR (300 MHz, DMSO-d_6) δ ppm 7.77 (d, 1H), 3.81 (m, 1H), 2.50 (m, 2H), 2.26 (t, J = 6 Hz, 2H), 2.15 (t, J = 6 Hz, 2H), 2.11 (s, 3H), 1.45 – 1.17 (m, 4H), 1.03 (d, J =6.6 Hz, 2H), 0.87 (t, J = 7.2 Hz, 3H).

Model compound *N*-(2-ethylhexyl)-3-((2-ethylhexyl)amino) propanamide (2)

Methyl acrylate (1g, 1 eq.) and 2-ethyl hexylamine (4.5 g, 3 eq.) were mixed in a three necked round bottom flask equipped with a probe for online ATR-IR. The reaction was carried out at 50 °C until total consumption of methyl acrylate was observed by intensity decreasing of the relative C=C stretching band at 989 cm^{-1} (^{1}H NMR is reported in **Figure 6.A2**). The temperature was then increased to 100 °C for 32 h for the amidation reaction. β-amino amide formation was assessed by following the diminishing of the ester carbonyl C=O stretching at 1740 cm^{-1} against the increase of the amide carbonyl C=O band at 1666 cm^{-1}. The formation of amino amide **2** was also confirmed by ^{1}H NMR (**Figure 6.A3**).

Tetra amino-ester crosslinker (I)

1,3-Cyclohexanebis(methylamine) (5g, 1 eq.) was dissolved in 20 ml methanol. The solution was then cooled down in an ice batch followed by the dropwise addition of methyl acrylate (5 eq.). The reaction mixture was stirred for 1 h at room temperature, and then for 24 h at 65 °C. The solvent and residual methyl acrylate were removed under reduced pressure resulting in a pale-yellow oil (yield = 95%).

^{1}H-NMR (300 MHz, $CDCl_3$) δ ppm 3.66 (s, 12H), 2.83-2.66 (m, 8H), 2.52 – 2.37 (m, 8H), 2.21 (d, 7.6 Hz, 4H), 1.84 – 1.11 (m, 8H), 0.75 – 0.24 (m, 2H).

Synthesis of covalent adaptable amino-amide network (BAA)

1 Eq. of tetra amino-ester crosslinker (I) and 2 eq. of commercially available diamine compounds were weighted and mixed in a glass vial using a magnetic stirrer. Subsequently, the amino-amide network formation via amidation was conducted at 100 °C for 24 h. Post-curing happened at 120 °C for 24 h under vacuum.

Synthesis of Pripol 2033 diacrylate (II)

Pripol 2033 (1 eq.) and TEA (2.4 eq.) were dissolved in DCM (40 mL) and cooled to 0 °C in an ice bath. To this solution, 2.4 eq. of acryloyl chloride in 10mL DCM was added sequentially. The solution was stirred for 1h at 0 °C and then at room temperature overnight. HCl 1M (20 mL) was added to quench the remaining acryloyl chloride, and the layers were separated. The organic layer was washed with aq. HCl (1 M, 2 × 50 mL), aq. $NaHCO_3$ (3 × 50 mL), and brine (50 mL), and dried over MgSO4. Removal of the solvent under vacuum resulted in a yellowish transparent oil (yield = 85%).

^{1}H-NMR (300 MHz, CDCl3) δ ppm 6.40 (dd, J = 17.3, 1.5 Hz, 2H), 6.12 (dd, J = 17.3, 10.4 Hz, 2H), 5.81 (dd, J = 10.4, 1.5 Hz, 2H), 4.14 (t, J = 6.7 Hz, 4H), 1.70-1.63 (m, 4H), 1.41 – 1.17 (m, 44H), 0.95 – 0.78 (m, 8H).

Synthesis of reference amino-ester network prepared with Pripol 2033 (BAE-P)

1 Eq. of 1,3- cyclohexanebis(methylamine) and 2 eq. of Pripol 2033 diacrylate (II) were weighted and mixed in a polypropylene cup using a DAC 150.1 FVZ speed mixer (mixing condition: 2 min at 2500 rpm). Then, the cup was placed in an oven at 100 °C for 48 h to complete network formation.

Appendix Chapter 6

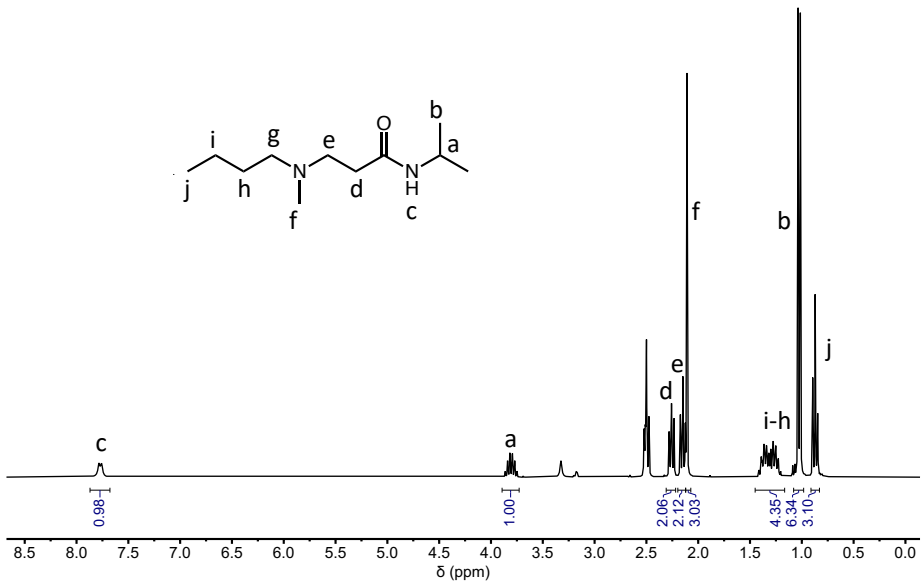

Figure 5.A1. *^{1}H-NMR spectrum in DMSO-d_6 of model compound* ***1****.*

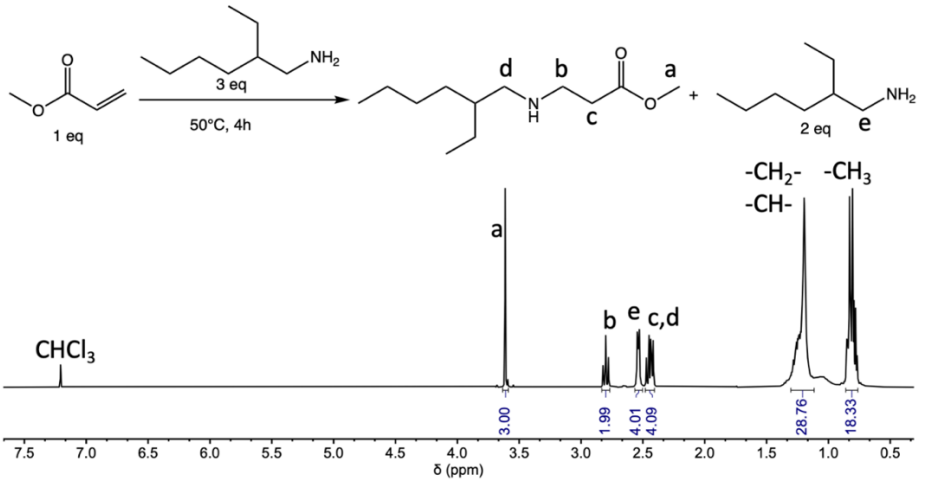

Figure 5.A2. *^{1}H-NMR spectrum in $CDCl_3$ of model study mixture after step 1 at 50 °C for 4 h which includes methyl 3-((2-ethylhexyl)amino)propanoate as Michael adduct and residual 2-ethyl-1-hexylamine (2 eq, confirmed by integral value of proton* ***e****).*

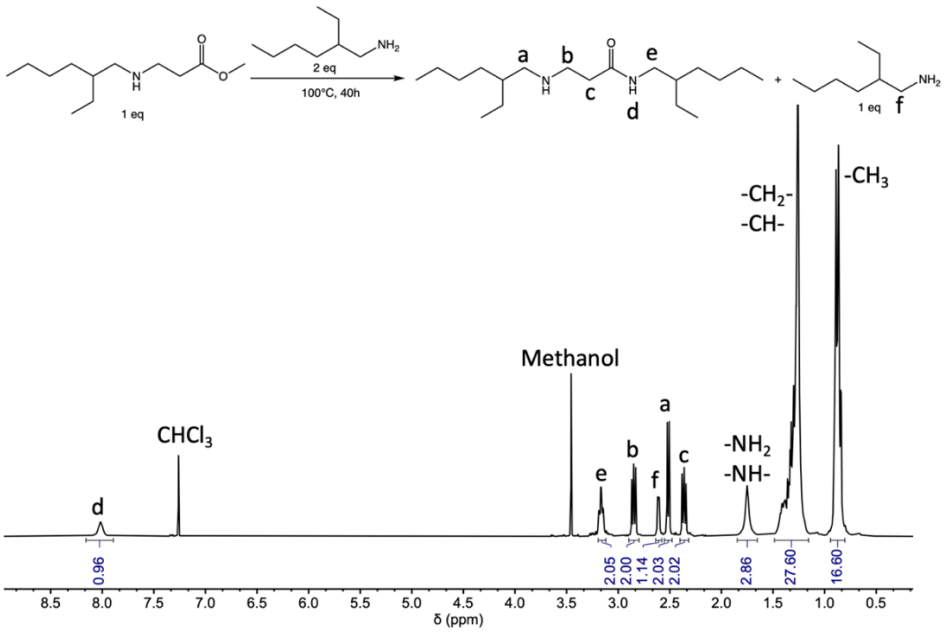

Figure 5.A3. *^{1}H-NMR spectrum in $CDCl_3$ of model compound 2 after amidation step at 100 °C for 40 h, showing also 1 eq residual of 2-ethyl-1-hexylamine (see integral of proton f).*

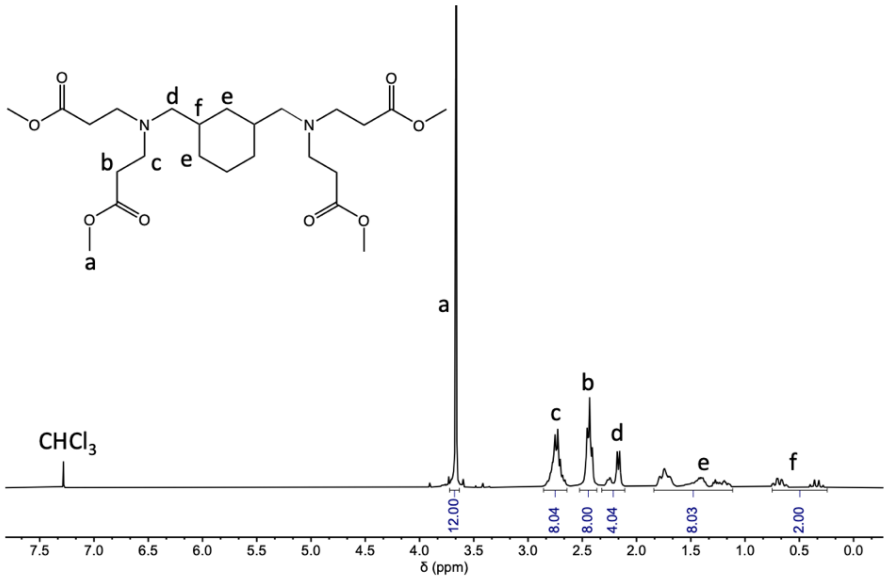

Figure 5.A4. *^{1}H-NMR spectrum in $CDCl_3$ of 1,3-bis(aminomethyl)cyclohexane tetra(amino-ester) crosslinker.*

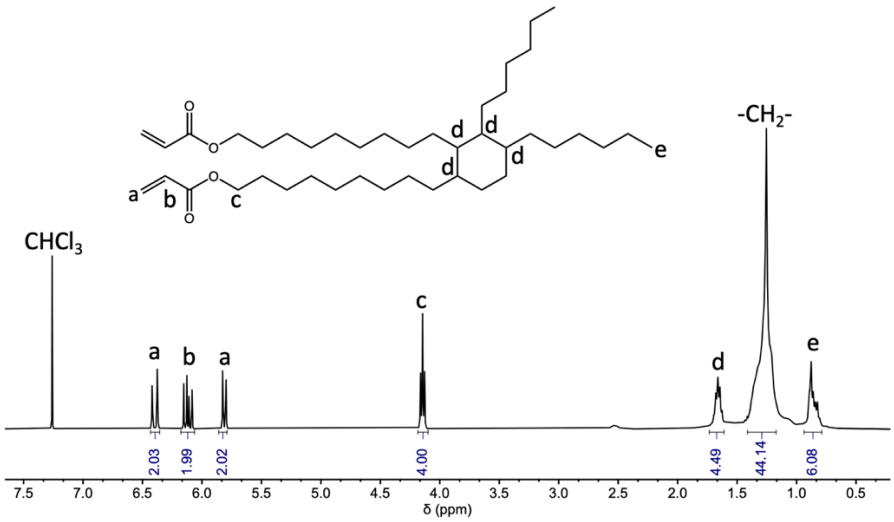

Figure 5.A5. *^{1}H-NMR spectrum in $CDCl_3$ of Pripol 2033-diacrylate.*

References

1 Lange, J.-P., *ACS Sustainable Chem. Eng.* **2021**, 9, 15722-15738.
2 Nikiema, J. and Z. Asiedu, *Environ. Sci. Pollut. Res.* **2022**, 29, 24547-24573.
3 Engelen, S., A.A. Wróblewska, K. De Bruycker, R. Aksakal, V. Ladmiral, S. Caillol, and F.E. Du Prez, *Polym. Chem.* **2022**, 13, 2665-2673.
4 Seay, J. and M.E. Ternes, *Clean Technol. Environ. Policy.* **2022**, 24, 731-738.
5 Chen, H., R. Qin, C.L. Chow, and D. Lau, *Cem. Concr. Compos.* **2023**, 137, 104922.
6 Liu, Z., Z. Fang, N. Zheng, K. Yang, Z. Sun, S. Li, W. Li, J. Wu, and T. Xie, *Nat. Chem.* **2023**, 1-7.
7 Denissen, W., J.M. Winne, and F.E. Du Prez, *Chem. Sci.* **2016**, 7, 30-38.
8 Scheutz, G.M., J.J. Lessard, M.B. Sims, and B.S. Sumerlin, *J. Am. Chem. Soc.* **2019**, 141, 16181-16196.
9 Chakma, P. and D. Konkolewicz, Angew. Chem. Int. Ed., **2019**, 58, 9682-9695.
10 Maes, S., F. Van Lijsebetten, J.M. Winne, and F.E. Du Prez, *Macromolecules* **2023**, 56, 1934-1944.
11 Winne, J.M., L. Leibler, and F.E. Du Prez, *Polym. Chem.* **2019**, 10, 6091-6108.
12 Van Lijsebetten, F., J.O. Holloway, J.M. Winne, and F.E. Du Prez, *Chem. Soc. Rev.* **2020**, 49, 8425-8438.
13 Chemical ScienceVan Lijsebetten, F., K. De Bruycker, E. Van Ruymbeke, J.M. Winne, and F.E. Du Prez, *Chem. Sci.* **2022**, 13, 12865-12875.
14 Zhang, V., B. Kang, J.V. Accardo, and J.A. Kalow, *J. Am. Chem. Soc.* **2022,** 144, 22358-22377.
15 Van Lijsebetten, F., T. Debsharma, J.M. Winne, and F.E. Du Prez, *Angew. Chem. Int. Ed.* **2022**, 61, e202210405.
16 Liu, Y., Z. Tang, D. Wang, S. Wu, and B. Guo, *J. Mater. Chem. A.* **2019**, 7, 26867-26876.
17 You, Y., M. Fu, M. Rong, and M. Zhang, *Materials Today Chemistry* **2022**, 23, 100687.
18 Ma, Y., H.-Q. Wang, P.-C. Zhao, F.-Z. Wang, and C.-H. Li, *J. Mater. Chem. A.* **2022**, 10, 20804-20812.
19 Rusayyis, M.A.B., L.M. Fenimore, N.S. Purwanto, and J.M. Torkelson, *Polym. Chem.* **2023**, 14, 3519-3534.
20 Cui, C., X. Chen, L. Ma, Q. Zhong, Z. Li, A. Mariappan, Q. Zhang, Y. Cheng, G. He, and X. Chen, *ACS Appl. Mater. Interfaces.* **2020**, 12, 47975-47983.
21 Schoustra, S.K. and M.M. Smulders, *Macromol. Rapid Commun.* **2023**, 44, 2200790.
22 Zhang, L., Z. Liu, L. Sun, L. Xiao, Q. Guan, and Z. You, *Macromolecules* **2021**, 54, 4081-4088.
23 Wang, S., N. Wang, D. Kai, B. Li, J. Wu, J.C.C. Yeo, X. Xu, J. Zhu, X.J. Loh, and N. Hadjichristidis, *Nat. Commun.* **2023**, 14, 1182.

24 Van Lijsebetten, F., K. De Bruycker, Y. Spiesschaert, J.M. Winne, and F.E. Du Prez, *Angew. Chem. Int. Ed.* **2022**, 61, e202113872.

25 Van Lijsebetten, F., Y. Spiesschaert, J.M. Winne, and F.E. Du Prez, *J. Am. Chem. Soc.* **2021**, 143, 15834-15844.

26 Park, J., H.Y. Song, S. Choi, S.-k. Ahn, K. Hyun, and C.B. Kim, *J. Mater. Chem. A.* **2022**, 10, 6475-6480.

27 Worrell, B.T., M.K. McBride, G.B. Lyon, L.M. Cox, C. Wang, S. Mavila, C.-H. Lim, H.M. Coley, C.B. Musgrave, and Y. Ding, *Nat. Commun.* **2018**, 9, 2804.

28 Obadia, M.M., A. Jourdain, P. Cassagnau, D. Montarnal, and E. Drockenmuller, *Adv. Funct. Mater.* **2017**, 27, 1703258.

29 Van Lijsebetten, F., K. De Bruycker, J.M. Winne, and F.E. Du Prez, *ACS Macro Lett.* **2022**, 11, 919-924.

30 Engelen, S., F. Van Lijsebetten, R. Aksakal, J.M. Winne, and F.E. Du Prez, *Macromolecules* **2023**, 56, 7055-7064.

31 Rusayyis, M.A.B. and J.M. Torkelson, *Polym. Chem.* **2021**, 12, 2760-2771.

32 Taplan, C., M. Guerre, and F.E. Du Prez, *J. Am. Chem. Soc.* **2021**, 143, 9140-9150.

33 Lee, G., H.Y. Song, S. Choi, C.B. Kim, K. Hyun, and S.-k. Ahn, *Macromolecules* **2022**, 55, 10366-10376.

34 Li, G., J. Huang, H.S. Soo, Y. Zhao, T. Li, Y. Wang, S. Wang, and W. Dong, *Eur. Polym. J.* **2023**, 194, 112165.

35 Stricker, L., C. Taplan, and F.E. Du Prez, *ACS Sustainable Chem. Eng.* **2022**, 10, 14045-14052.

36 Jeon, D., Y. Yoon, D. Kim, G. Lee, S.-k. Ahn, D. Choi, and C.B. Kim, *Macromolecules* **2023**, 56, 697-706.

37 Berne, D., G. Coste, R. Morales-Cerrada, M. Boursier, J. Pinaud, V. Ladmiral, and S. Caillol, *Polym. Chem.* **2022**, 13, 3806-3814.

38 Berne, D., B. Quienne, S. Caillol, E. Leclerc, and V. Ladmiral, *J. Mater. Chem. A.* **2022**, 10, 25085-25097.

39 Al Thaher, Y., S. Latanza, S. Perni, and P. Prokopovich, *J. Colloid Interface Sci.* **2018,** 526, 35-42.

40 Muralidharan, A., R.R. McLeod, and S.J. Bryant, *Adv. Funct. Mater.* **2022**, 32, 2106509.

41 Liu, X., Z. Zhao, F. Wu, Y. Chen, and L. Yin, *Adv. Mater.* **2022**, 34, 2108116.

42 De Geest, B.G., W. Van Camp, F.E. Du Prez, S.C. De Smedt, J. Demeester, and W.E. Hennink, Macromol. *Rapid Commun.* **2008**, 29, 1111-1118.

43 Van Herck, S., L. Van Hoecke, B. Louage, L. Lybaert, R. De Coen, S. Kasmi, A.P. Esser-Kahn, S.A. David, L. Nuhn, and B. Schepens, *Bioconjugate Chem.* **2017**, 29, 748-760.

44 Huppertsberg, A., L. Kaps, Z. Zhong, S. Schmitt, J. Stickdorn, K. Deswarte, F. Combes, C. Czysch, J. De Vrieze, and S. Kasmi, *J. Am. Chem. Soc.* **2021**, 143, 9872-9883.

45 Yi, C., J. Zhao, Z. Zhang, and J. Zhang, *Ind. Eng. Chem. Res.* **2017**, 56, 13743-13750.

Part of the work of this chapter was done under the supervision of prof. Filip Du Prez at Ghent University.

Chapter 6

Epoxy adhesive with β-Amino Amide reversible crosslinking

6.1. Introduction

Currently, the adhesive market is constantly growing due to the widespread applications of such materials. In 2021, 1.2 million tons of adhesive were produced in Europe.[1] The versatility of adhesives is testified by the many different application fields: electronics, aerospace, construction, dentistry, etc.[2] They contribute to the utilization of advanced materials improving the structural integrity in the component. The term adhesive is used for non-metallic materials that have the ability to weld substrates.[3,4] The substrates involved can be either similar or entirely dissimilar, including materials such as glass, ceramics etc.

Three important zones can be identified in an adhesive joint[5] (**Figure 6.1**) that determine how strongly different materials can be bonded. The first is the adhesion zone at the interface of the two materials. The strength of the adhesion at this level is determined by the compatibility and type of interaction involved between the materials, typically covalent or non-covalent interaction.[6] A transition zone exists between the bulk of the adhesive and the adhesion zone where the composition, structure and properties of the adhesive continuously change. Moving away from the surface, the bulk of the adhesive is called cohesive zone. In this case, cohesion strength is given by covalent bonds but also intramolecular interactions within polymer chains.

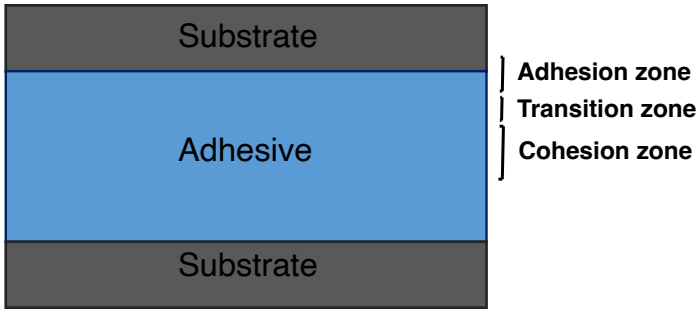

Figure 6.1. *Schematization of adhesive areas.*

The strength of adhesion is determined by how the adhesive interacts with the substrate. Generally, non-covalent or reversible interactions, such as hydrogen bonds, exhibit lesser strength when compared to covalent bonds.[7] Nonetheless, increasing the number of interactions can result in strong adhesion. Other parameters influencing the interaction are pH, concentration, solvent.[8,9] For demanding applications, it is preferred to use adhesives with improved bond strength and solvent resistance. As a result, adhesives have been developed to create covalent or irreversible bonds with substrates.[10]

It is important to note that not all interfaces between adhesives and adherents have complementary functional groups for covalent bond formation. To achieve the desired functionality, adhesion promoters or primers are used to pre-treat the substrate surface.[11] Silanes are commonly used promoters to enhance the interaction between a metal and an adhesive.[12]

Adhesive display a variety of adhesion mechanisms depending on the application. The main distinction is between structural and non-structural adhesive. Pressure-sensitive, hot-melt and contact adhesive belong to the latter category.

Pressure-sensitive adhesives (PSAs) are generally acrylic-based,[13] that adhere to surfaces when slight pressure is applied. These adhesives remain tacky and adhere to substrates without the need for heat or solvent activation.[14] PSAa are widely used in various application, due to their convenience, ease of use, and versatility in bonding different materials. Additionally, pressure-sensitive adhesives (PSAs) are prone to

creep due to their non-solid nature, resulting in a decrease in strength as temperatures increase. This can cause the adhesive joint to undergo gradual flow and permanent deformation over time.[3] The best known example is the "glue" of Post-It™ notes.[15]

Hot melt adhesives (HMAs) are thermoplastic materials that are solid at room temperature but, when heated, undergo a phase transition to a molten state, allowing for application as an adhesive.[14] These adhesives are available in various forms, such as blocks, pellets, or irregular shapes. Subsequently, they are applied in the preferred configuration onto the substrate, establishing adhesion through a process involving wetting and permeation. Applications of hot melt adhesives are widespread and include packaging, woodworking, product assembly, bookbinding, and hygiene product manufacturing, among others.

Differently from hot-melt category, contact adhesives are normally in liquid form, with the adhesive component (polychloroprene or polyurethane) dissolved in a volatile solvent that readily evaporates.[16] A thin film is then form on the substrate capable to bind other different support by only applying a small pressure. A commercial example daily used is Pattex™ glue.[17]

Non-structural adhesives are not applicable to high load material, the realm of structural adhesives. They are extremely important to build lightweight structure for automotive and aviation industry.[18] Unlike general-purpose adhesives, structural adhesives are formulated to provide high strength and long-term performance, making them suitable for application where the structural integrity of the bonded material is critical. A structural adhesive is identified as a material with a lap shear strength greater than 7 MPa.[7] Epoxy thermosets are one of the most known classes, as well as polyacrylate or polyurethane.[3] These adhesives are engineered to withstand various environmental factors, including temperature fluctuations, moisture, and exposure to chemicals, ensuring the longevity of the bonded joint.

Most recently, a highly supramolecular crosslinked epoxy hot melt adhesive, has been reported and can reused multiple times reaching an adhesion strength of 10 MPa.[19] Although early investigations in this field focused on supramolecular adhesives,

dynamic systems offer a compelling alternative when stronger connections are required. Several examples, including disulfide exchange,[20,21] Diels-Alder chemistry,[22,23] boronic ester transesterification,[24] and transesterification[25] have been reported in the literature.

In 2023, Van Lijsebetten *et al.* reported an example of epoxy adhesive using amide-imide exchange chemistry.[26] Polyamides and amidoamines are well-known curing agents used in a variety of markets, including adhesives, such as Ancamide™, produced by Evonik. These adhesives are often used in epoxy formulations as curing agents to create a crosslinked network, which enhances the strength and durability of the adhesive. Considering the use of polyamides in adhesive formulations, they prepared a prepolymer as dynamic curing agent for epoxy materials by simply mixing commercially available monomers. The adhesive properties of such network are greater compared to an epoxy reference material, providing new insights for the development of debondable structural adhesives.

To enlarge the library of dynamic chemistry employed in this field, β-aminoamide exchange chemistry, presented in Chapter 5, is used for the development of structural adhesive.

6.2. *Results and discussion*

Conventional epoxy thermoset resins are prepared from step-growth polymerization employing small molecule monomers resulting in high conversion. Dynamic covalent bonds can be introduced to the network *via* in situ crosslinking reaction, such as carboxylic anhydride, resulting in dynamic transesterification.[27] In this approach, all the crosslinking sites are dynamic, which give rise to limited mechanical performances, such as poor creep resistance, because of possible exchange reaction al low temperatures. To address this issue, several researchers have introduced permanent crosslinking to examine its effect on the material properties. One approach to creating a network is to use curing agents that contain dynamic bonds. Networks prepared using this method have both dynamic and permanent bonds, resulting in improved mechanical performance.[28–30] This method can also be used to turn conventional thermoplastics

into vitrimers without altering the reaction conditions. For example, the use of curing agents with dynamic covalent bonds in epoxy curing systems provides a convenient and effective way for producing epoxy-based vitrimers using conventional reaction routes and conditions for crosslinked epoxy resins.[31,32]

This approach was adopted in this chapter to prepare debondable adhesives, which involves the use of a commercial phenoxy-like resin Epikote™ 828LV from Westlake Epoxy. Such liquid epoxy component was selected for its wide use in adhesion formulation for the high performances (up to 41 MPa).[33] One factor which contributes to this property is the low shrinkage shown during cure as well as the presence of pendant hydroxyl group capable to interact with different substrates. In this work, an amine-terminated linear pre-polymer, containing dynamic β-aminoamide moieties, is then used as curing agents for the commercial epoxy component.

The dynamic pre-polymer was synthesized using the two-step approach described in Chapter 5. In the initial step, methyl acrylate was reacted with 1,3-di(piperidin-4-yl)propane in methanol to yield β -amino ester **1** with a quantitative yield (**Scheme 6.1**).

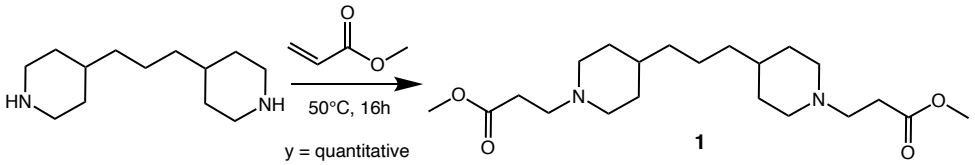

Scheme 6.1. *Synthesis of compound **1** via Michael addition reaction.*

The choice of the secondary amine was made to avoid a second Michael addition, which would have resulted in a branched crosslinker instead of in a linear one. The formation of the Michael adduct was confirmed by ^{1}H NMR (see experimental section).

Polycondensation reaction of compound **1** (0.8 eq) with 2,2,4-trimethyl-1,6-hexanediamine (1 eq) at 120 °C for 24 hours results in the viscous pre-polymer BAA-A.

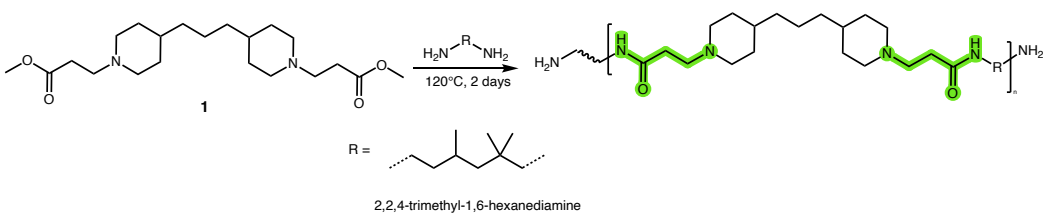

Scheme 6.2. *Scheme of the polycondensation reaction for the preparation of the reversible hardener using compound* ***1*** *and 2,2,4-trimethyl-1,6-hexanediamine.*

The crosslinker was characterized using IR and ^{1}H NMR, as shown in **Figure 6.2**. From IR spectra it is visible the disappearance of the C=O stretching band of compound **1** and the appearance of N-H and C=O amide stretching.

Furthermore, upon examination of the ^{1}H NMR spectra, it was confirmed that all ester moieties have reacted as the characteristic singlet of the methyl ester at 3.61 ppm is not present in BAA-A spectrum. Instead, a broad signal (indicated by the green dotted circle) is observed at 2 ppm, which is associated to the signal of the terminal amine group.

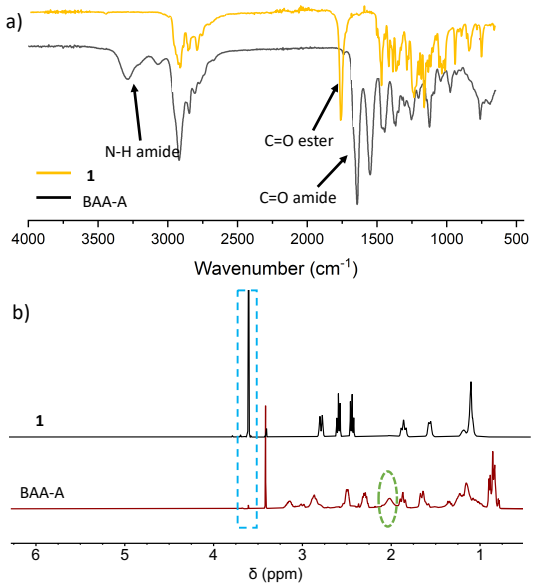

Figure 6.2. *a) IR spectra and b) ^{1}H-NMR ($CDCl_3$, 300 MHz, 25°C) spectra comparison of compound 1 and BAA-A.*

The obtained pre-polymer BAA-A was then used as curing agent in the polymerization reaction with Epikote 828LV, conducted at 80°C for 16 h (**Scheme 6.3)**.

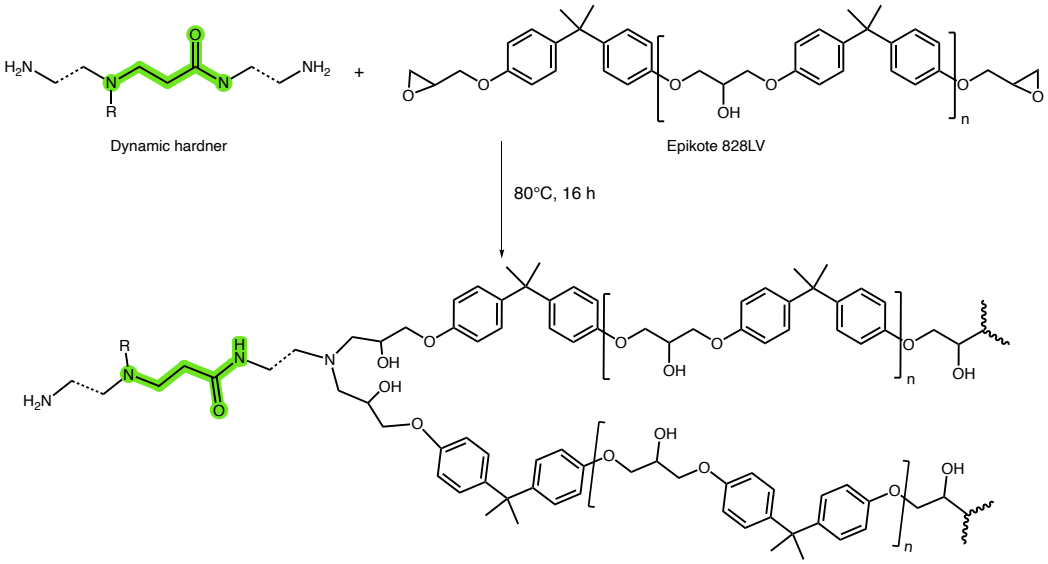

Scheme 6.3. *Schematic representation of epoxy network preparation. In green is highlighted the dynamic β-aminoamide moieties presented in the hardener.*

However, due to the high viscosity of BAA-A, the use of solvent (chloroform) was necessary to achieve a homogenous mixture. Therefore, to avoid the use of a solvent and synthesize the network in bulk, taking advantage of the liquid epoxy component, the attention was shifted to a different dynamic crosslinker, prepared by varying amines to tailor the viscosity. More specifically, aromatic XYDIA and aliphatic BAC and priamine were selected (**Scheme 6.4**). The corresponding pre-polymers were synthesized using the same conditions as for BAA-A, through a polycondensation reaction of compound **1** and the selected amines.

The results showed that BAC and XYDIA produced a solid hardener, while the presence of long aliphatic chains of priamine resulted in a low viscosity β-aminoamide polymer, therefore, the focus was on the latter.

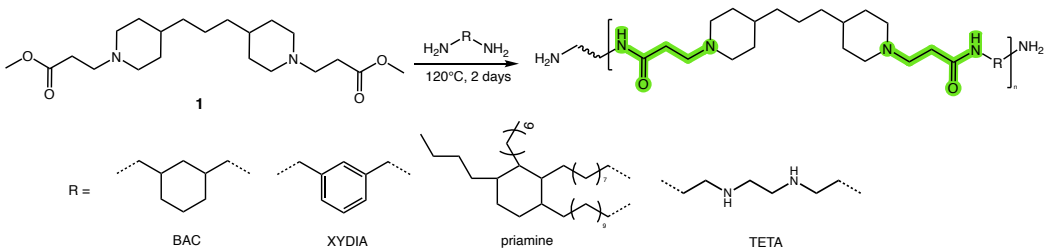

Scheme 6.4. *Preparation of the reversible hardener using compound **1** and different amines.*

A formulation of compound **1**, priamine and TETA (**Scheme 6.3**) were then used to prepare the dynamic crosslinker. More specifically, TETA was selected for its secondary amine in the structure, which reacts with the epoxy moiety, introducing permanent crosslinking. This allows for a wider range of T_g values for the materials.

To produce a poly-aminoamides with two amine end groups, a stoichiometric excess of 0.2 equivalents of amine groups was used. This excess ensures that no additional chain growth occurs once all the ester moieties of compound **1** are consumed.

Taking into account the residual -NH functionalities of the prepolymer, the hardeners obtained, where then directly used in the polymerization reaction, mixing them with epoxy (1:1 epoxy/amine ratio, **Table 6.1**, experimental section) at 80°C for 16 h to obtain BAA-T0, BAA-T10, BAA-T20 respectively for the materials without TETA, with 0% mol, 10% mol and 20% mol of TETA.

FT-IR (**Figure 6.3**) and gel fraction (**Table 6.1**) evaluation were used to verify the formation of the network.

Table 6.1. *Overall properties of the synthesized* networks *with a range of amines.*

	Swelling degree (%)	**Soluble fraction (%)**	**T_g (°C)**	**$T_{d5\%}$ (°C)**	**$m_{iso\ 200°C,\ 1h}$ (%)**
BAA-T0	102 ± 5	5,1 ± 0,2	10	341	<1
BAA-T10	104 ± 11	2,6 ± 0,3	18	345	<1
BAA-T20	85 ± 11	1,4 ± 0,3	25	315	<2

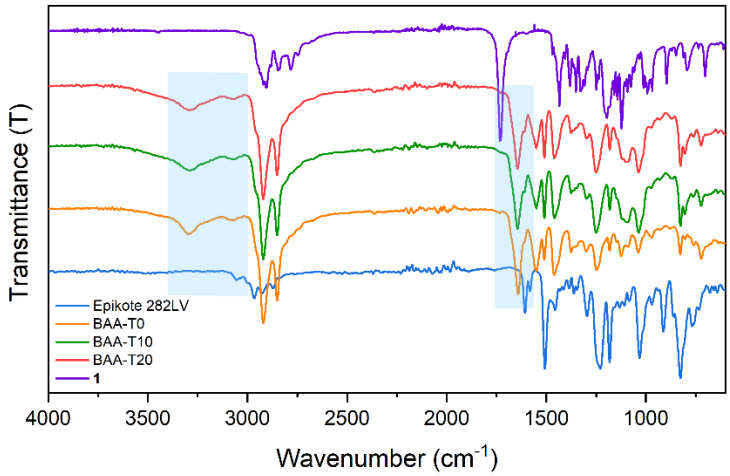

Figure 6.3. *IR spectra stacking of the network BAA-T0, BAA-T10, BAA-T20 in comparison to compound 1 and Epikote 828LV.*

To ensure that the dynamic crosslinker does not have negative impact on thermal stability, DSC (**Figure 6.4c**) and TGA (**Figure 6.4a**) analyses were performed. Although T_g values vary from 10 to 30°C, thermal stability gives promising results showing a $T_{d5\%}$ in the range of 310-340°C (**Table 6.1**). Isothermal TGA experiments (**Figure 6.4b**), performed at 200°C for 1h revealed only 2-1% of weight loss (**Table 6.1**), resulting in negligible oxidation or degradation of the materials at high temperatures.

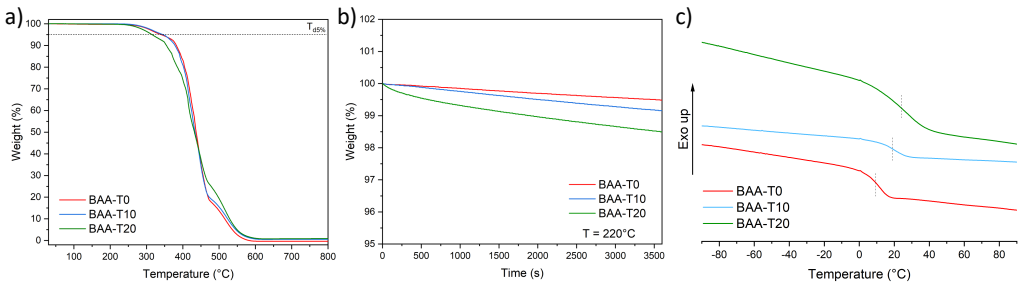

Figure 6.4. *a) TGA thermogram, b) isothermal TGA thermogram, c) DSC curves of BAA-T0 (red line), BAA-T10 (blue line) and BAA-T20 (green line).*

To demonstrate the reprocessability of the networks, they were grinded into powder and pressed at least twice at 200°C for 30 min under 3 tons (**Figure 6.5a**). FT-IR samples showed no significant changes after the second reprocessing cycle. (**Figure 6.5b**)

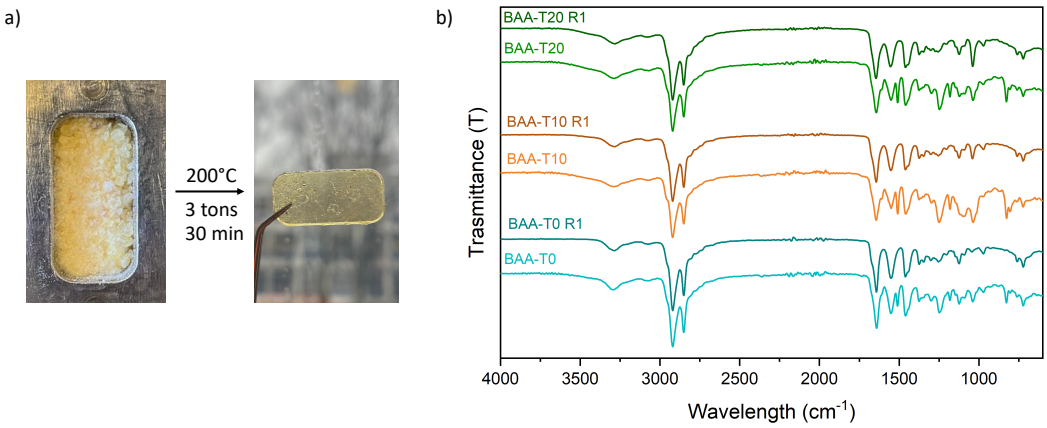

Figure 6.5. *Reprocessing demonstration of BAA-T0, b) IR spectra comparison of the initial BAA-T0, BAA-T10, BAA-T20 (lightest color line) and after one cycle of (re)compression molding (darkest color lines).*

The dynamic behavior of BAA-T0, BAAT10 and BAA-T20 was then examined by rheology performing stress relaxation experiment in a temperature range from 200°C to 220°C. As results, all materials dissipate the stress via network rearrangements. Results are reported in **Figure 6.6**.

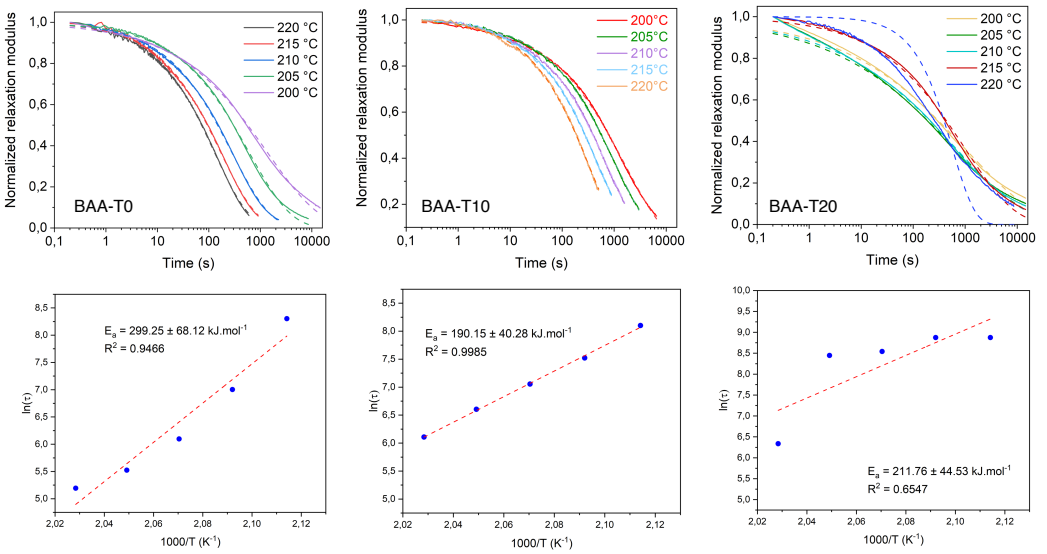

Figure 6.6. *Normalized stress relaxation curves with fitting in the dotted lines and derived Arrhenius plots of BAA-T0 (left), BAA-T10 (middle) and BAA-T20 (right).*

A high-temperature dependence of the dynamic behaviour is observed in which the applied stress could be relaxed completely at elevated temperatures, favouring the (re)processability. However, fitting stress relaxation curves (**Figure 6.6** dotted line) with the single Maxwell model did not provide good match, therefore Kohlrausch–Williams–Watts (KWW) stretched exponential decay function (**Eq 6.1**) was used to calculate the relaxation time since it takes into account differences in relaxation of the composing network segments.[34]

$$G\,(t) = G_0 e^{(\frac{-t}{\tau})^{\beta}} \qquad (6.1)$$

Comparing BAA-T0 and BAA-T10 a large variation in activation energy, respectively 299 kJ·mol^{-1} and 190 kJ·mol^{-1} is observed. This aspect emphasizes that chain diffusion significantly affects the rate of network rearrangement. When diffusion is impeded, stress relaxation may occur more slowly than in a free system. The presence of permanent crosslinking may contribute to this effect. Interestingly, BAA-T10, containing more permanent bonds compared to BAA-T0, has the lowest activation energy value. The bond dissociation, followed by an association with another dissociated group, is the rate-determining step for dynamic behaviour. Therefore, it can be assumed that a proximity-like effect exists in the BAA-T10 network due to the short structure of TETA being positioned close enough to the dissociated group, thus resulting in a decreasing of activation energy.

The adhesion properties of the network were then determined using lap shear experiments. Bond failure can occur in either the cohesion or adhesion zone. The tensile force applied to the sample results in a shear stress across the entire adhesive area (**Figure 6.7a**). The nature of the fracture is crucial to provide insights into adhesives performances. The fracture can typically be classified into three types: cohesive failure, where the break occurs within the adhesive itself, adhesive failure, in which the break is between the substrate and the adhesive and combination failure, where the failure occurs within both adhesive and adhesive-substrate bonds. Schematization of modes of failures is reported in **Figure 6.7b**.

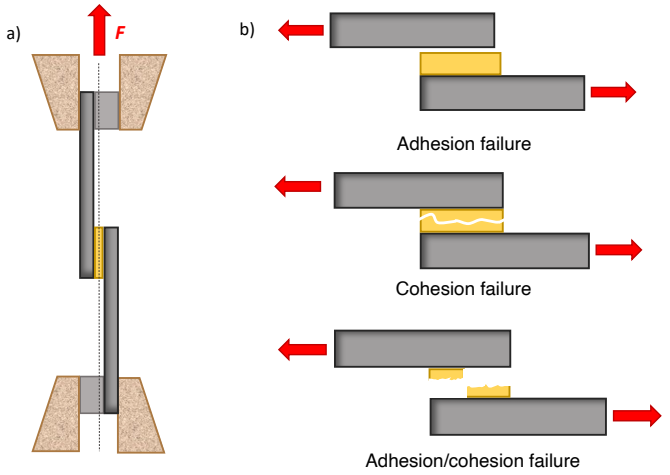

Figure 6.7. *a) Representation of lap shear experiment; b) Modes of failure of a generic adhesive.*

Experimentally, the formulations were coated using 0,1 g of the previously mixed formulation on the surface of two aluminium plates, that were overlapped in an area of 400 mm^2 (16 mm x 24.8 mm) with a thickness of 0,2 mm according to ASTM D1002 procedure.[35] The samples were then subsequently cured at 80°C for 16 h (**Figure 6.8**).

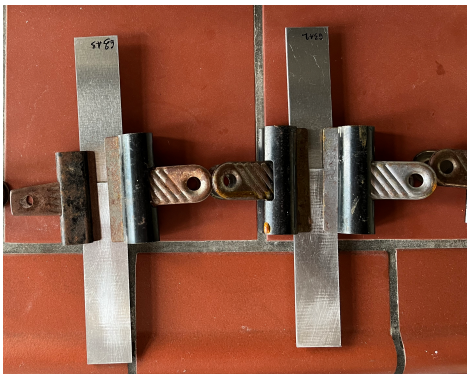

Figure 6.8. *Picture of specimens under preparation for lap shear test.*

The lap shear test results (**Figure 6.9a**) resulted in an increasing trend of lap shear strength values moving from BAA-T0 to BAA-T20, respectively 8.1 MPa, 10.1 MPa, and 12.8 MPa. The presence of dynamic β-aminoamide bonds forms strong hydrogen bonding within the bulk and the substrate. Moreover, increasing the number of

permanent bonds in the network resulted in an enhancement of the lap shear strength as the material resembles more closely a conventional epoxy resin.

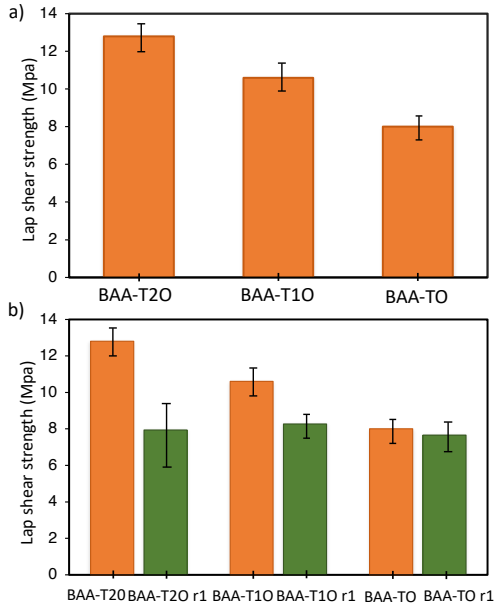

Figure 6.9. *Lap shear strength of BAA-T0, BAA-T10 and BAA-T20 before (a) and after (b) the recycling.*

Furthermore, the majority of the specimens reported a combined failure, indicating relatively strong adhesion and cohesion of the formulation. (**Figure 6.10**)

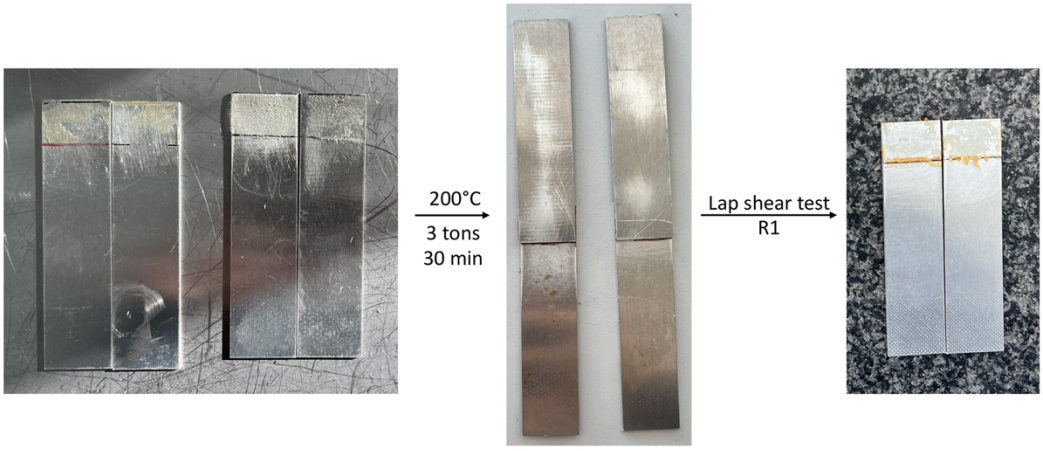

Figure 6.10. *Pictures of broken specimens after lap shear test (left), recycled specimens (middle) and broken specimens after lap shear test of the first recycle (right).*

The broken specimens were subsequently bonded together by pressing the aluminium joints at 200°C for 30 minutes under 3 tons (**Figure 6.10**). Lap shear experiment where then repeated on the regenerated specimens. Results are reported in **Figure 6.9b** and **Table 6.2**. BAA-T20 and BAA-T10 reported a partial recovery of the adhesive properties, respectively ≈ 64% and ≈ 75% while BAA-T0 allowed to be recovered up to 95% of the initial lap shear strength.

Table 6.2. *Overview of lap shear strength value of the networks synthetized before and after the first recycle.*

	Lap shear strength (MPa)	Lap shear strength r1 (MPa)
BAA-T0	8.1 ± 0.8	7.7 ± 1.1
BAA-T10	10.5 ± 0.8	7.9 ± 1.5
BAA-T20	12.8 ± 1.6	8.3 ± 3.5

Lap shear experiment were also performed at 180°C (**Figure 6.11**), showing in some cases completely detaching of the specimens before the measurement run or sliding of the aluminum joint with forces close to 0 N necessary to detach them.

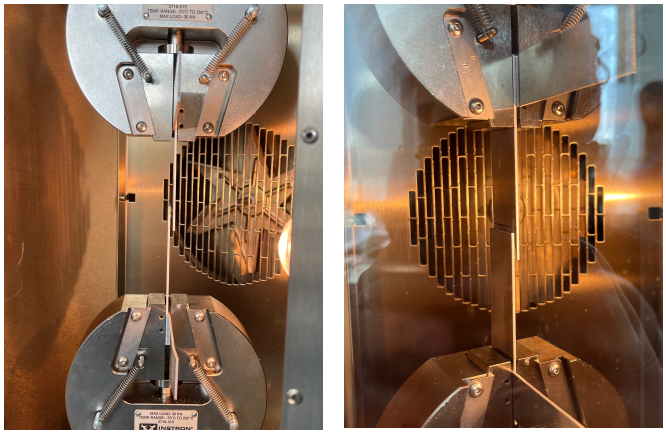

Figure 6.11. *Pictures of lap shear test performed at 180°C. In the left picture is visible the two aluminum joints already detached before the measurements, on the right the sliding of the specimen.*

The specimens were then re-bonded by pressing them at 200°C for 30 min under 3 tons of pressure and lap shear experiments were repeated at 180°C giving the same initial results.

6.3. *Conclusions*

Reversible adhesives were successfully prepared by curing a liquid phenoxy-like component (Epikote 828LV) with a dynamic β-aminoamide hardener through a conventional epoxy-amine curing process. Rheological measurements revealed a temperature-dependent stress relaxation with activation energy in the range of 299-190 $kJ \cdot mol^{-1}$, as well as the ability of the networks to be (re)processed at least once without altering the material properties. Lap shear test of the materials performed by coating and curing the network on an aluminum surface, reveal excellent results even after the first recycling. Further characterization and optimization of the networks will be necessary to improve the promising performances of such formulations.

Acknowledgements

Thanks to prof. Filip Du Prez, Loc Tan Nguyen and Bernhard De Meyer from University of Ghent. Thanks to Dr. Federico Bertani and Giulia Mannoni from Elantas Europe, Collecchio, Parma for the lap shear test at elevated temperatures.

6.4. *Experimental section*

Materials and methods

All materials were used without further purification unless stated otherwise.

Nuclear magnetic resonance (NMR) spectra were recorded on a Bruker Advance Ultrashield 300 MHz spectrometer. Deuterated chloroform ($CDCl_3$) or deuterated DMSO-d6 was used as solvent. Chemical shifts are given in parts per million (ppm).

Attenuated total reflection Fourier transform infrared spectroscopy (ATR-FTIR) spectra were measured using a Perkin-Elmer Spectrum1000 FTIR infrared spectrometer with a diamond ATR probe.

Thermogravimetric analyses (TGA) were performed with a Mettler Toledo TGA/SDTA851e instrument under air atmosphere at a heating rate of 10 K·min−1 from 25 to 800 °C for the dynamic mode or at 200 °C for 2 h for the isothermal measurement.

Differential scanning calorimetry (DSC) analyses were performed with a Mettler Toledo instrument 1/700 under air atmosphere at a heating rate of 10 K·min−1 from −100 to 100 °C.

Rheology experiments were performed on an Anton Paar MCR 302. The experiments were performed in parallel plate geometry using 8 mm sample disks. Amplitude sweep experiments were performed using a frequency of 1 Hz, a constant force of 1 N, and a variable shear strain that was ramped up logarithmically from 0.01% to 10% to observe the linear viscoelastic region. Stress-relaxation experiments were performed at different temperatures (200 - 170 °C, with intervals of 10 °C) using a constant shear strain within the linear viscoelastic region of the samples, and a constant force of 1 N. The obtained characteristic relaxation time (τ^*) was used to calculate the activation energy.

(Re)processability was investigated by cutting the crosslinked material into pieces of about 1 cm, which were then placed into a rectangular mold for compression molding. This assembly was placed in a preheated compression press (200 °C) for 1 min under 0.5 metric tons of pressure. Then the pressure was increased to 3 tons and kept constant for an additional 60 min. After 60 min of pressing, the sample was carefully removed from the mold.

Solubility tests were carried out in vials with samples of 2 mm in diameter, 2 mm in thickness, and a weight of around 15-20 mg, to which 40 mL of THF was added. Those tests were performed for 24 h at 25 °C in THF. The solvent was then removed, and the samples were dried under vacuum overnight at 60 °C. The soluble fraction and swelling ratio were calculated using equation 1 and equation 2, respectively.

$$\text{soluble fraction (\%)} = \frac{m_i - m_d}{m_i} \quad \text{(eq. } 1\text{)}$$

$$\text{swelling ratio (\%)} = \frac{m_s - m_i}{m_i} \quad \text{(eq. 2)}$$

with m_i, m_s, and m_d representing the mass of initial, swollen, and dry samples, respectively.

Lap shear tests: Instron mod 5982 was used with a load cell of 10000 N at a speed of 1.3 mm/min using ASTM standard type lap-shear joints (ASTM 1002D). Specimens were prepared by adding the adhesive formulation to a surface of overlap length of 16 mm and width of 25 mm, using aluminum samples with a thickness of 2 mm. The joints were prepared by scraping the surface and washing with methyl ethyl ketone and ethyl acetate, curing of the epoxy resin with a wet thickness of 200 μm at 80 °C for 16 h, using metal clamps to apply mild pressure. Additionally, an INSTRON alignment kit was used to align the grips.

Dimethyl 3,3'-(propane-1,3-diylbis(piperidine-4,1-diyl))dipropionate

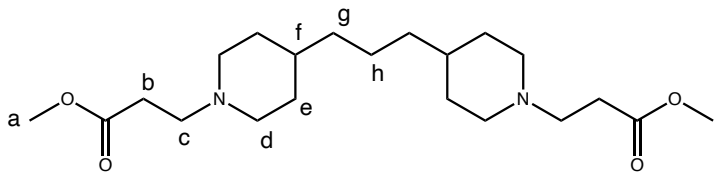

1

In a round bottom flask, 10 g of 1,3-di(piperidin-4-yl)propane (1 eq) was dissolved in 10 mL of methanol, then 14 mL of methyl acrylate (3 eq) was added using a dripping funnel to the reaction mixture. The reaction was conducted at 50°C for 24 h. Afterwards, methanol and the excess of methyl acrylate was removed under vacuum distillation and compound **1** was obtained as a transparent liquid in quantitative yield.

^{1}H-NMR (300 MHz, $CDCl_3$) δ ppm: 3.61 (s, 6H), 2.79 (d, 4H), 2.60 (t, 4H), 2.45 (t, 4H), 1.87 (t, 4H), 1.59-1.57 (m, 4H), 1.21-1.09 (m, 12 H).

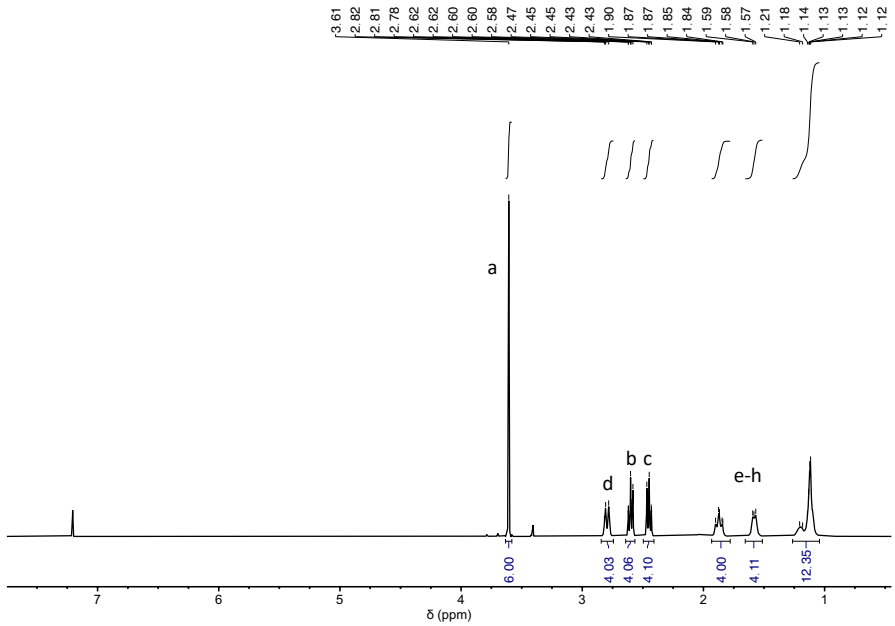

General procedure for curing agent

In a 20 mL propylene cup, compound **1** (0.8 eq) was mixed with the selected amines (1 eq) using a DAC 150.1 FVZ speed mixer (conditions of mixing: 2 min with a speed of 2500 rpm). The reaction was conducted at 120°C for 24 h then other in vacuum oven for other 24 h to completely remove the released methanol.

Epoxy adhesives synthesis (BAA-T0, BAA-T10, BAA-T20, BAA-T30)

The dynamic crosslinkers were directly reacted with Epikote 828LV (epoxy to amine ratio = 1) in the same propylene cup using a DAC 150.1 FVZ speed mixer (conditions of mixing: 2 min with a speed of 2500 rpm). The curing of the network was performed in an oven at 80°C for 16 h.

***Table 6.3**. equivalent and grams used for each component for the preparation of the adhesive.*

	Compound 1 (eq, g)	**Priamine (eq, g)**	**TETA (eq, g)**	**Epikote (eq, g)**
BAA-T0	0.8, 2	1, 3.57	-	0.8, 0.96
BAA-T10	0.8, 2	0.9, 3.22	0.1, 0.095	1, 1.2
BAA-T20	0.8, 2	0.8, 2,86	0.2, 0.19	1.2, 1,45
BAA-T30	0.8, 2	0.7, 2,5	0.3, 0.29	1.4, 1.69

References

[1] Adhesives Market 2021 Demand Analysis, Industry Size-Share Estimation, Top Leading Companies, Future Strategies, Growth Statistics, Revenue and Forecast to 2030. February 22, 2022.

[2] A. Marques, A. Mocanu, N. Tomić, S. Balos, E. Stammen, A. Lundevall, S. Abrahami, R. Günther, J. De Kok, S. Teixeira De Freitas, *Materials* **2020**, *13*, 5590.

[3] S. Ebnesajjad, in *Handbook of Adhesives and Surface Preparation*, Elsevier, **2011**, pp. 3–13.

[4] P. Zuo, A. P. Vassilopoulos, *Int. Mater. Rev.* **2021**, *66*, 313.

[5] J. A. Von Fraunhofer, *Int. J. Dent.* **2012**, *2012*, 1.

[6] S. Ebnesajjad, in *Surface Treatment of Materials for Adhesive Bonding*, Elsevier, **2014**, pp. 77–91.

[7] S. Ebnesajjad, in *Adhesives Technology Handbook*, Elsevier, **2009**, pp. 63–135.

[8] Q. Zhang, T. Li, A. Duan, S. Dong, W. Zhao, P. J. Stang, *J. Am. Chem. Soc.* **2019**, *141*, 8058.

[9] M. Liu, P. Liu, G. Lu, Z. Xu, X. Yao, *Angew. Chem. Int. Ed.* **2018**, *57*, 11242.

[10] J. Brandt, K. K. Oehlenschlaeger, F. G. Schmidt, C. Barner-Kowollik, A. Lederer, *Adv. Mater.* **2014**, *26*, 5758.

[11] M. D. Bukhari, G. A. Gohar, A. Akhtar, S. Ullah, M. Akram, J. Abid, H. Raza, *VW. Appl. Sci* **2019**, *2*, 74.

[12] L. Kersey, V. Ebacher, V. Bazargan, R. Wang, B. Stoeber, *Lab Chip* **2009**, *9*, 1002.

[13] S. Mapari, S. Mestry, S. T. Mhaske, *Polym. Bull.* **2021**, *78*, 4075.

[14] A. V. Pocius, in *Polymer Science: A Comprehensive Reference*, Elsevier, **2012**, pp. 305–324.

[15] C. Plummer, *ChemMatters* **1993**, 13.

[16] K. Zhang, H. Shen, X. Zhang, R. Lan, H. Chen, *J. Adhes. Sci. Tech.* **2009**, *23*, 163.

[17] Pattex contact adhesive, Technical Data Sheet.

[18] D. A. Dillard, *Advances in Structural Adhesive Bonding*, Elsevier, **2010**.

[19] P. Sun, Y. Li, B. Qin, J.-F. Xu, X. Zhang, *ACS Materials Lett.* **2021**, *3*, 1003.

[20] H.-Y. Tsai, Y. Nakamura, T. Fujita, M. Naito, *Mater. Adv.* **2020**, *1*, 3182.

[21] L. Li, X. Chen, J. M. Torkelson, *ACS Appl. Polym. Mater.* **2020**, *2*, 4658.

[22] W. Xiangjun, X. Li, Q. Lin, J. Xia, H. Xue, *RSC Adv.* **2021**, *11*, 32565.

[23] L. M. Sridhar, M. O. Oster, D. E. Herr, J. B. D. Gregg, J. A. Wilson, A. T. Slark, *Green Chem.* **2020**, *22*, 8669.

[24] Z. Zhao, P. Zhao, Y. Zhao, J. Zuo, C. Li, *Adv. Funct. Mater.* **2022**, *32*, 2201959.

[25] S. Zhang, T. Liu, C. Hao, L. Wang, J. Han, H. Liu, J. Zhang, *Green Chem.* **2018**, *20*, 2995.

[26] F. Van Lijsebetten, T. Maiheu, J. M. Winne, F. E. Du Prez, *Adv. Mater.* **2023**, *35*, 2300802.

[27] L. Yue, M. Amirkhosravi, X. Gong, T. G. Gray, I. Manas-Zloczower, *ACS Sust. Chem. Eng.* **2020**, *8*, 12706.

[28] A. Breuillac, A. Kassalias, R. Nicolaÿ, *Macromolecules* **2019**, *52*, 7102.

[29] J. J. Cash, T. Kubo, D. J. Dobbins, B. S. Sumerlin, *Polym. Chem.* **2018**, *9*, 2011.
[30] L. Li, X. Chen, K. Jin, J. M. Torkelson, *Macromolecules* **2018**, *51*, 5537.
[31] Y. Spiesschaert, M. Guerre, I. De Baere, W. Van Paepegem, J. M. Winne, F. E. Du Prez, *Macromolecules* **2020**, *53*, 2485.
[32] X.-L. Zhao, Y.-Y. Liu, Y. Weng, Y.-D. Li, J.-B. Zeng, *ACS Sustainable Chem. Eng.* **2020**, *8*, 15020.
[33] EPIKOTE Resin 828, Westlake, Technical Data Sheet.
[34] J. C. Hooker, J. M. Torkelson, *Macromolecules* **1995**, *28*, 7683.
[35] D14 Committee, *Test Method for Apparent Shear Strength of Single-Lap-Joint Adhesively Bonded Metal Specimens by Tension Loading (Metal-to-Metal)*, ASTM International, **n.d.**

Abbreviations

ACN	Acetonitrile
ADMET	Acyclic diene methatesis polymerization
DBTL	Dibutyltin dilaurate
DCE	Dichloroethane
DCM	Dichloromethane
DIC	Digital Imaging Correlation
DMF	Dimethylformamide
DMSO	Dimethylsufoxide
DSC	Differential Scanning Calorimetry
EtOAc	Ethyl acetate
ESI-MS	Electrospray Ionization Mass Spectrometry
FT-IR	Fourier transform-infrared spectroscopy
o-DCB	orto-dichlorobenzene
MALDI-TOF	Matrix-assisted laser desorption/ionization – time of flight
MW	Microwave
MeOH	Methanol
NMR	Nuclear magnetic resonance spectroscopy
pTsOH	para-Toluenesulfonic acid
QxCav	Quinoxaline cavitand
rT	room temperature
TBD	Triazabicyclodecene
TEA	Triethylamine
TETA	Triethylenetetramine
T_g	Glass transition temperature
UV-Vis	Ultraviolet-visible
XPS	X-ray photoelectron spectroscopy
XRD	X-ray diffraction